Numerical simulations of seismic wave propagation in anisotropic and heterogeneous Earth models—the Japan subduction zone

Thesis by

Min Chen

In Partial Fulfillment of the Requirements

for the Degree of

Doctor of Philosophy

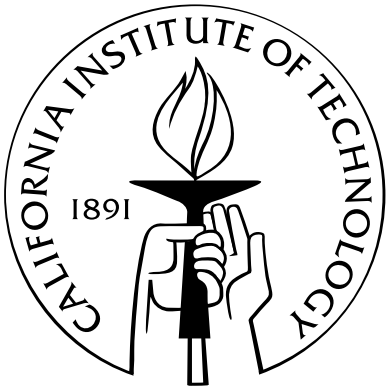

California Institute of Technology

Pasadena, California

2008

(Defended April 28, 2008)

To My Family and All My Friends

Acknowledgements

I want to thank my dad for the letter he wrote me about half a year ago. In the letter, he was very worried about my health during this marathon type Ph.D. study. He wrote it doesn't matter if I don't get a Ph.D. in the end. In order to convince me that getting a Ph.D. is really not so important, my dad even mentioned the stories of some MIT dropouts who did great later in their career. Caltech is not as famous as MIT in China, otherwise, my dad would also know similar stories at Caltech. I am very sure these MIT dropouts must be very brilliant, otherwise, everyone else would flunk Ph.D. study and become rich and famous. However, I am not so sure about myself being that brilliant, so I decided not to take the risk, and my dad's letter turned out certainly to be a big drive for me to write this thesis.

I want to think my advisor Jeroen Tromp, for his tremendous patience and guidance throughout my Ph.D. study. I learned a lot from Jeroen, his attitude of treating research, passion, and precision. Whenever I was in his office, listening to his exciting ideas about how a big project can be done, I always got convinced. Although sometimes after stepping out of his office, I started to realize how challenging it would be to make everything work. But whenever I faced research challenges, it was Jeroen's patience and optimism that always kept me from giving up. It's also pleasant to listen to him explaining and answering questions, as he can really convey it in a simple but precise way, which really saved me lots of brain cells. I also want to thank Jeroen's generosity of letting us having the opportunity of going on the European trips. Although these trips were for academic meetings, they were indeed an eye-opening experience to me.

I want to thank Don Helmberger for teaching me how to look at the seismograms, which makes me feel like a real seismologist sometimes. It was a very nice experience working with Don on the Japan waveform modeling project. He always came up with all kinds of

ideas, most of which I didn't try because of my laziness. Otherwise, I could have graduated sooner and become rich and famous. Like all the other Chinese students, I fully appreciate all of Don's shockingly funny jokes. Academic life in Seismo Lab could have been very boring without all the laughter floating around.

I want to thank Hiroo Kanamori for his patience and knowledge in answering all my questions, and thanks for all the efforts he made to get all the data needed for the Japan tomography project. This project wouldn't be possible without his help. I really appreciate his strict way of dealing with every scientific detail, and his constructive discussion in Seismo Lab social hour.

Thanks to my academic advisor, Mike Gurnis for all the signatures he made on all of my important academic paperwork and his enlightening conversations.

Thanks to Joann Stock, Rob Clayton, and Jean-Philippe Avouac for leading all those wonderful field trips, which I really enjoyed lot.

Thanks to my oral committee chair, Tom Heaton for all the helpful advices he gave before and after my oral exams.

I would like to take this paragraph to thank people in my research group, my lab-mates, office-mates, and Seismo Lab staff. Thanks to Qinya and Vala for all the wonderful scripts they coded, for all the discussions they contributed to enlighten me. Thanks to Carl for his active organization of all the group meetings and tons of research or soccer related emails he sent, which were very helpful. Thanks to Alessia, Ying, Anne, Yonghee, Laura, Givanni, and Christina for all the constructive group discussions. Thanks to Ozgun for all the Turkish snacks, food, and coffee. Thanks to Xiangyan for being considerately quiet and watering my orchid when I was away. Thanks to Francisco for his excellent flyer design skill for the Caltech Salsa Club, which saved me lots of time when I was the club president. Thanks to Dan Bower to agree on being the Salsa Club president after me, so that I know it is in good hands and I can concentrate on writing my thesis. Thanks to Kristin for her support to the Salsa Club in every aspect. Thanks to Ravi, Ensueo, Lijun, Chris, Nathan, and Yossi for all their constant effort to maintain the friendly environment of Seismo Lab. Thanks to all the staff in Seismo Lab that make everything so convenient in the lab. Especially, I want to thank Viola, Ellisa, Everlyna, and Sue for all the help they provided. Thanks to Mike and

Ken for all the IT support.

Maybe it's kind of strange, but I want to thank Mr. Walt Disney for all the wonderful cartoon characters and the Disneyland he created for kids and people who still have the heart to enjoy the ideals of creation, imagination, optimism, and happiness. Thanks to all my Disneyland buddies for sharing all the fun and joys with me in Disneyland.

I want to thank all my friends at Caltech, mainly my friends I have known in Caltech Salsa Club for years. Thanks to Stephane, Daven, Theo, Elena, Corrine, Saina, Ros, Nikoo, Dan, Kristin, Tom, Steffen ... Thanks to those who introduced me to salsa dancing and all these people who danced with me. It was great fun to be able enjoy something like salsa outside my research life.

I also want to thank all my soccer pals at Caltech, Glendale and Duarte. It's great that women's soccer is so popular here in California. The soccer games really bring lots of joys to me, plus the good health. I am very glad to be able to know so many wonderful ladies on the soccer field. Thanks to my teammates Sher, Evie, Penny, Meridith and Stephanie for their constant support on the soccer field. Thanks to all my teammates from team Elephant and Castle, Storm, Sublime, and Red Vine. Also thanks to my coed soccer teammates here at Caltech, soccer team of Chinese Students, and GPS division.

Thanks to professor Aden Albee for the wonderful field trip he led in Death Valley many years ago. Thanks to all the people who were on that trip. Especially, Arnaud Saintraine, Vishal Shah, and Stephane Lintner, who turned out to be very good friends of mine.

Thanks to all the friends I made during the last year of my Ph.D. study, Riccardo, Luca, Luigi, Jestus, Diego, Sarah, Guido, Noel, Magali, Anthony, and Mathieu for their friendship.

Thanks to Ying Tan, Zhimei Yan, Huiyu Li, and Xiangyan Tian for sharing their thoughts and care during my Ph.D. study.

Thanks to my dearest friend Jiaying Lou and her husband Min Mao for the great friendship in the past many years.

At last, thanks to all my family members: Daoyuan Sun for all his care, constant support and love in the past nine years; my dad Xingchang Chen, my mom Jiacui Jiang, my sister Beilei Chen, and my niece Lele Chen for their love and support through all my life.

Abstract

This thesis involved studies of the seismic wave propagation in fully anisotropic and heterogeneous Earth models, and the seismic velocity structures in the Japan subduction zone derived from the observations, using both forward modeling and tomographic methods. All the simulations of seismic wave propagation in this thesis have been carried out using both 2-D finite-difference method (FDM) and 3-D spectral-element method (SEM).

we extend the SEM code to incorporate three-dimensionally, fully anisotropic earth models. For weakly anisotropic media, we benchmark the numerical simulations against asymptotic, ray theoretical predictions for both surface waves and body waves. The numerical simulations and asymptotic predictions are in good agreement for anisotropy at the 5% level. Weakly anisotropic body-wave propagation involves all 21 independent elastic parameters. The code is capable of simulating the shear-wave splitting in terms of waveforms. Strong waveform distortions are observed when the seismic waves propagate through a simple and weakly anisotropic Earth model. Our results also further prove the anisotropic effects on body-wave traveltime are completely directional dependent.

From the high-density waveform data provided by Japanese data center (NIED), we observed a strong secondary SH arrival recorded in NE Japan. In order to explain this secondary arrival, a thin but strong low velocity layer (LVL) on top of the slab has to be introduced. Our 2-D model suggests the LVL extends down to a depth of 300 km with an S-wave velocity reduction of 14% if a thickness of 20 km is assumed. Further 3-D SEM simulations confirm that this model explains the strong secondary arrival. We interpret this deeply extended LVL as a zone composed of hydrated mafic and/or ultramafic rocks, and more likely ultramafic rocks (serpentinized peridotite) at depths greater than 150 km. The water released from the dehydration reactions in this hydrous zone could cause the abundant arc volcanism, the intermediate-depth intra-slab seismicity (70–30 km),

and possible silent slip events.

In order to obtain better 3-D seismic velocity models of the Japan subduction zone and the neighboring region beneath Eastern China, we use adjoint tomography to iteratively minimize the misfit between the synthetics and data from Hi-net, F-net, and Global Seismographic Network (GSN) stations. In this study, we are able to maximize the information obtained from three-component seismic records for tomographic inversion by using an automated windowing code. It selects not only the body-wave but also the surface-wave windows. With a dataset of 206 events in the Japan subduction zone, the frequency-dependent traveltime measurements are made in 44,709 windows for the period range of 24–120 s and 119,376 windows for the period range of 6–30 s. The combined adjoint sources are thus constructed based on these traveltime misfit measurements for all the receivers. Given the adjoint sources, we use the adjoint spectral-element method to calculate banana-doughnut kernels for the selected records. The weighted sums of the banana-doughnut kernels for all event-station pairs, with weights determined by the traveltime measurements, can be used to construct misfit kernels, which are the gradients required in a non-linear conjugate gradient algorithm to further refine the existing 3-D model.

Contents

List of Figures

List of Tables

Chapter 1

Introduction

It is challenging to find an universal 3-D seismic velocity model to fully describe the Earth, given the complexity of the Earth itself, the challenges posed by the biased data coverages, and all the assumptions lying behind the forward and inversion techniques . But on the other hand, the non-uniqueness of Earth models also provides us a wide space to explore the different flavors of the Earth. And the studies of two classes of the Earth models, the anisotropic and the heterogeneous, are presented in this thesis.

To find out how intrinsic seismic anisotropy of the Earth media affects seismic wave propagation, we extend the spectral-element method code to incorporate three-dimensionally, fully anisotropic earth models (Chapter 2, published by *Chen and Tromp* [2007]). For weakly anisotropic media, we benchmark the numerical simulations against asymptotic, ray theoretical predictions for both surface waves and body waves.

The originality of our research on anisotropy is that we can calculate the 3-D synthetic waveforms using SEM code with high accuracy. With this advantage, we observed strong waveform distortions when the seismic waves propagate through a simple and weakly anisotropic Earth model, which alternatively must require a complex and severely heterogeneous isotropic Earth model to explain. Our results further prove the anisotropic effects on body-wave traveltime are completely directional dependent, which again brings out the big challenge in seismic anisotropy imaging, the non-uniqueness given the actual limited azimuthal and incidence-angle data coverage. But at the same time, we also observed the same intrinsic anisotropy affect the multiple seismic phases very differently in terms of both traveltime and amplitude. Therefore, maximizing the imaging of intrinsic anisotropy

requires the unconventional parts or observables of the seismograms to be taken into account, e.g., the multiple observations, which may help constrain intrinsic anisotropy.

The theoretical and numerical results we've presented for this study provide new insight into connection between seismic waveforms and anisotropy, which should guide future tomographic inversion for anisotropic heterogeneity. The forward modeling tool, which calculates seismograms in fully 3D anisotropic media, can certainly be used for both testing the existing anisotropic models and waveform model anisotropic regions inside the Earth.

With the high-density waveform data provided by Japanese data center (NIED), I study the detailed velocity structure of the slab beneath Japan (in Chapter 3, Section 3.1–3.8 are published by *Chen et al.* [2007]).

In this study, 2-D FDM and 3-D SEM synthetic seismograms were calculated for an existing tomographic model of the Japan subduction zone developed by *Zhao et al.* [1994]. Within a one-chunk SEM mesh domain with lateral dimensions of $30^\circ \times 30^\circ$, we simulate the wave propagation accurate at periods of 3 seconds or longer on 100 processors. The synthetics were compared with the observed waveforms from the Hi-net array. The comparison shows that *Zhao et al.* [1994]'s regional P-wave model reduces the data-synthetics traveltime residuals relative to the 1-D model by $\sim 50\%$, but the observed waveforms are not well matched by the synthetics, especially not the observed strong secondary SH arrivals in NE Japan. By a combination of forward modeling and a grid search, we obtained a 2-D model with a thin but strong low velocity layer (LVL) on top of the slab extending to a depth of 300 km, which cannot be easily imaged with traveltime tomographic techniques.

Although there are former observations of LVL in Japan and other subduction zones, the LVL we observed is deeper and has even stronger velocity reduction, and can not be explained by an oceanic crust alone. We interpret this deeply extended LVL as a zone composed of hydrated mafic and/or ultramafic rocks, and more likely ultramafic rocks (serpentinized peridotite) at depths greater than 150 km. The water released from the dehydration reactions in this hydrous zone could cause the abundant arc volcanism, the intermediate-depth intra-slab seismicity (70–30 km), and possible silent slip events. By incorporating this low velocity layer as a low viscosity layer in the 2-D dynamic models, the low viscosity layer can create the slabs with more realistic shallow and deep dips [*Manea and Gurnis*,

2007].

With the goal of obtaining more detailed images of the Japan subduction zone, I am currently working on applying an adjoint spectral-element method [*Tromp et al.*, 2005] on the Japan regional tomography (Chapter 4, part of this chapter is in the paper by *Maggi et al.* [2008], *in preparation*).

We use *Zhao et al.* [1994]'s 3-D model embedded in *Lebedev and Nolet* [2003]'s model as the initial model in the tomographic inversion. The method proceeds in using adjoint tomography to iteratively minimize the misfit between the 3-D SEM synthetics and data from Hi-net, F-net, and Global Seismographic Network (GSN) stations (total 845). In collaboration with Japanese data center (NIED), we prepared a dataset of 269 total events ($4.5< M_w <8$) to obtain maximum coverage of this region while avoiding redundancy.

We construct the adjoint sources using the frequency-dependent traveltime misfits between synthetics and data for P, S, and surface waves. For each event, we back-propagate the adjoint sources at all receivers into the model to create the adjoint wave field, which interacts with the regular wave field to produce the event kernel. The sum of all event kernels gives the sensitivity region in the current model and the gradients for a non-linear conjugate gradient algorithm to further refine the existing 3-D models.

Chapter 2

Theoretical and Numerical Investigations of Global and Regional Seismic Wave Propagation in Weakly Anisotropic Earth Models

2.1 Abstract

Smith and Dahlen [1973] demonstrated that in a weakly anisotropic Earth model the relative surface-wave phase speed perturbation $\delta c/c$ may be written in the form $\delta c/c = \sum_{n=0,2,4}(A_n \cos n\zeta + B_n \sin n\zeta)$, where A_n and B_n are frequency-dependent depth integrals and ζ denotes the ray azimuth. In this approximation, surface-wave anisotropy is governed by 13 elastic parameters and the azimuthal dependence of the phase speed is represented by an even Fourier series in ζ involving degrees zero (5 elastic parameters), two (6 elastic parameters), and four (2 elastic parameters). *Jech and Pšenčík* [1989] demonstrated that in such a weakly anisotropic Earth model the relative compressional-wave phase-speed perturbation may be expressed as $\delta c/c = (2c^2)^{-1}B_{33}$, whereas the relative shear-wave phase-speed perturbations are given by $\delta c/c = (4c^2)^{-1}\{B_{11} + B_{22} \pm [(B_{11} - B_{22})^2 + 4B_{12}^2]^{1/2}\}$. We demonstrate that the coefficients B_{33}, B_{11}, B_{22}, and B_{12} may be written in the generic form $B_{lm} = \sum_{n=0}^{4}\left[a_n(i)\cos n\zeta + b_n(i)\sin n\zeta\right]$ where ζ denotes the local azimuth and i the local angle of incidence. For B_{11}, B_{22}, and B_{33} the coefficients $a_n(i)$ and $b_n(i)$ are an even Fourier series of degrees zero, two, and four in i, but for B_{12} they are an odd Fourier series of degrees one and three. Like surface waves, the azimuthal (ζ)

dependence of body waves involves even degrees zero (5 elastic parameters), two (6 elastic parameters), and four (2 elastic parameters), but, unlike surface waves, it also involves the odd degrees one (6 elastic parameters) and three (2 elastic parameters). Thus, weakly anisotropic body-wave propagation involves all 21 independent elastic parameters. We use spectral-element simulations of global and regional seismic wave propagation to assess the validity of these asymptotic body- and surface-wave results. The numerical simulations and asymptotic predictions are in good agreement for anisotropy at the 5% level.

2.2 Introduction

The theory of surface-wave propagation in weakly anisotropic Earth models was developed by *Smith and Dahlen* [1973]. Their analysis predicts degree two and four azimuthal variations of surface-wave phase speeds, which were first observed by *Forsyth* [1975] and have been widely used to constrain maps of anisotropic phase-speed variations [e.g., *Montagner and Nataf*, 1986; *Nishimura and Forsyth*, 1989; *Montagner and Tanimoto*, 1990, 1991; *Montagner*, 2002; *Trampert and van Heijst*, 2002; *Trampert and Woodhouse*, 2003].

The asymptotic theory of body-wave propagation in anisotropic media is also well developed [e.g., *Crampin*, 1984; *Thomsen*, 1986; *Tsvankin*, 1997; *Červený*, 2001; *Chapman*, 2004]. In this paper we derive approximate expressions for body-wave phase speeds in weakly anisotropic media that complement the surface-wave theory derived by *Smith and Dahlen* [1973], and extend the body-wave results obtained by *Backus* [1965], *Červený* [1982], *Hanyga* [1982], *Jech and Pšenčík* [1989], and *Mensch and Rasolofosaon* [1997] to spherical coordinates. The shear-wave traveltime predictions are based upon the degenerate perturbation theory developed by *Jech and Pšenčík* [1989] and summarized by *Červený* [2001] and *Chapman* [2004]. Recently, first-order ray tracing equations for quasi-shear waves in weakly anisotropic Earth models were determined by *Farra* [2005].

We use our asymptotic results to predict surface-wave phase and body-wave traveltime anomalies in weakly anisotropic models, and compare these predictions to phase and traveltime anomalies determined from numerical simulations. A first attempt at combining observations of surface- and body-wave anisotropy was made by *Montagner and Griot-*

Pimmera [2000]; the results derived in this paper further facilitate such combined inversions.

The spectral-element method (SEM) has enabled accurate three-dimensional (3D) simulations of global [*Komatitsch and Tromp*, 2002a,b; *Chaljub et al.*, 2003; *Capdeville et al.*, 2003] and regional [*Komatitsch and Vilotte*, 1998; *Komatitsch and Tromp*, 1999; *Komatitsch et al.*, 2004] seismic wave propagation in laterally heterogeneous Earth models. Spectral-element simulations for spherically symmetric reference Earth model PREM [*Dziewonski and Anderson*, 1981] were carefully benchmarked against semi-analytical normal-mode calculations by *Komatitsch and Tromp* [2002a]. General two-dimensional (2D) and 3D anisotropy was considered by *Komatitsch et al.* [2000]. In this paper we extend spectral-element simulations of seismic wave propagation to incorporate fully 3D anisotropic Earth models. For weakly anisotropic media, we compare the numerical simulations against theoretical predictions and systematically assess how the elastic parameters affect surface- and body-wave propagation.

2.3 Theory

In the following two sections we discuss the directional dependence of surface- and body-wave propagation in weakly anisotropic media. The assumption will be that we have a laterally homogeneous background model superimposed on which we introduce weak anisotropic perturbations. In the context of global surface-wave propagation we will use a transversely isotropic reference model characterized by the five elastic parameters A, C, L, N, and F [*Love*, 1911; *Dziewonski and Anderson*, 1981]. For global and regional body-wave propagation we will use an isotropic reference model characterized by two elastic parameters: the bulk modulus κ and the shear modulus μ; in such an isotropic model we have $A = C = \kappa + \frac{4}{3}\mu$, $L = N = \mu$, and $F = \kappa - \frac{2}{3}\mu$. We include a brief synopsis of the well-known directional dependence of surface-wave phase speed [e.g., *Smith and Dahlen*, 1973; *Montagner and Nataf*, 1986; *Larson et al.*, 1998], and, following *Jech and Pšenčík* [1989], present a complementary result for the directional dependence of body-wave phase speeds. These asymptotic results will be tested against global and regional spectral-element

simulations in subsequent sections.

2.3.1 Surface Waves

Smith and Dahlen [1973] demonstrated that in a flat, weakly anisotropic Earth model the directionally dependent relative surface-wave phase speed perturbation $\delta c/c$ may be written in the form

$$\delta c/c = \sum_{n=0,2,4} (A_n \cos n\zeta + B_n \sin n\zeta), \tag{2.1}$$

where A_n and B_n are depth integrals involving the radial eigenfunctions of the laterally homogeneous reference model, and ζ denotes the azimuth. The underlying assumption is that the anisotropy is sufficiently weak such that quasi-Love and quasi-Rayleigh waves can be defined, and that no folding of the wavefront occurs [*Crampin*, 1977]. Note the even nature of the Fourier series (2.1), which implies that waves traveling in the direction ζ move at the same speed as those traveling in the opposite direction $\zeta + \pi$:

$$(\delta c/c)(\zeta) = (\delta c/c)(\zeta + \pi). \tag{2.2}$$

Larson et al. [1998] demonstrated that an expression similar to (2.1) holds on a spherical Earth model, in which case ζ denotes the local azimuth. Based upon the results derived by *Larson et al.* [1998], measuring the local azimuth ζ counter-clockwise from due south, for quasi-Love waves the coefficients A_n and B_n, $n = 0, 2, 4$, may be expressed as

$$A_0 = (2cGI_1)^{-1} \int_b^a \left[\delta N k^2 r^{-2} W^2 + \delta L(\partial_r W - r^{-1}W)^2\right] r^2 dr, \tag{2.3}$$

$$B_0 = 0, \tag{2.4}$$

$$A_2 = -(2cGI_1)^{-1} \int_b^a G_c(\partial_r W - r^{-1}W)^2 \, r^2 dr, \tag{2.5}$$

$$B_2 = (2cGI_1)^{-1} \int_b^a G_s(\partial_r W - r^{-1}W)^2 \, r^2 dr, \tag{2.6}$$

$$A_4 = -(2cGI_1)^{-1} \int_b^a E_c k^2 W^2 \, dr, \tag{2.7}$$

$$B_4 = (2cGI_1)^{-1} \int_b^a E_s k^2 W^2 \, dr, \tag{2.8}$$

where G denotes the group speed in the isotropic reference model and

$$I_1 = k^2 \int_b^a \rho \, W^2 \, r^2 dr. \tag{2.9}$$

The unperturbed Love-wave radial eigenfunction is denoted by W, the associated wavenumber is k, r denotes the radius, ρ the density, and a and b denote the radii of the free surface and the core-mantle boundary, respectively. Love-wave anisotropy is governed by 6 out of a possible 21 elastic parameters: the two 0ζ transversely isotropic perturbations δL and δN, the two 2ζ parameters G_c and G_s, and the two 4ζ parameters E_c and E_s. The relationship between these elastic parameters and the elements of the elastic tensor in spherical coordinates is given in Appendix A.1.

For quasi-Rayleigh waves we have

$$\begin{aligned} A_0 = (2cGI_1)^{-1} \int_0^a & [k^{-2}\delta C(\partial_r U)^2 + \delta L(\partial_r V - r^{-1}V + r^{-1}U)^2 \\ & + 2\delta F k^{-2} r^{-1} \partial_r U (2U - k^2 V) + (\delta A - \delta N) k^{-2} r^{-2} (2U - k^2 V)^2 \\ & + \delta N r^{-2} k^2 V^2] \, r^2 dr, \end{aligned} \tag{2.10}$$

$$B_0 = 0, \tag{2.11}$$

$$A_2 = (2cGI_1)^{-1} \int_0^a \left[G_c(\partial_r V - r^{-1}V + r^{-1}U)^2 - B_c r^{-2} V (2U - k^2 V) - 2H_c r^{-1} V \partial_r U \right] r^2 dr, \tag{2.12}$$

$$B_2 = -(2cGI_1)^{-1} \int_0^a \left[G_s(\partial_r V - r^{-1}V + r^{-1}U)^2 - B_s r^{-2} V (2U - k^2 V) - 2H_s r^{-1} V \partial_r U \right] r^2 dr, \tag{2.13}$$

$$A_4 = (2cGI_1)^{-1} \int_0^a E_c k^2 V^2 \, dr, \tag{2.14}$$

$$B_4 = -(2cGI_1)^{-1} \int_0^a E_s k^2 V^2 \, dr. \tag{2.15}$$

In this case

$$I_1 = \int_0^a \rho (U^2 + k^2 V^2) \, r^2 dr, \tag{2.16}$$

and the unperturbed Rayleigh-wave radial eigenfunctions are U and V.

Rayleigh-wave anisotropy is governed by 13 out of a possible 21 elastic parameters: the five 0ζ transversely isotropic perturbations δA, δC, δL, δN, and δF, the six 2ζ parameters G_c, G_s, B_c, B_s, H_c, and H_s, and the two 4ζ parameters E_c and E_s (see also Appendix A.1). Table 2.1 summarizes the azimuthal effects of the 13 independent elastic parameters on Rayleigh and Love surface waves as well as body waves.

Based upon Fermat's principle, the relative phase anomaly $\delta\psi/\psi$ is given by

$$\delta\psi/\psi = -\frac{1}{\Delta}\int_0^\Delta \delta c/c \, d\,\mathrm{ray} = -\delta\bar{c}/c, \tag{2.17}$$

where the integration is along the unperturbed surface-wave ray, i.e., a great circle, over the epicentral distance Δ, and $\delta\bar{c}/c$ denotes the path-averaged relative phase-speed anomaly. In Section 2.4 we will use equation (2.17) in conjunction with (2.1) to predict path-averaged relative phase-speed anomalies for idealized weakly anisotropic models.

2.3.2 Body Waves

In this section we present asymptotic expressions for directionally dependent body-wave phase speeds in weakly anisotropic media that complement the surface-wave result (2.1). We will consider an isotropic background model upon which we superimpose weakly anisotropic perturbations [for a summary see *Červený*, 2001, Section 3.9.4]. We begin by considering wave propagation in the isotropic reference model, which is controlled by the Christoffel equation

$$(\mathbf{\Gamma} - c_m^2\mathbf{I}) \cdot \hat{\mathbf{g}}_m = \mathbf{0}, \tag{2.18}$$

where $\mathbf{I}$ denotes the identity tensor. The eigenvalues of (2.18) determine the three body-wave phase speeds c_m, $m = 1, 2, 3$, and the associated orthonormal eigenvectors $\hat{\mathbf{g}}_m$, $m = 1, 2, 3$, determine the polarization directions. The symmetric matrix $\mathbf{\Gamma}$ is given by

$$\mathbf{\Gamma} = [(\kappa + \tfrac{1}{3}\mu)\hat{\mathbf{p}}\hat{\mathbf{p}} + \mu\mathbf{I}]/\rho, \tag{2.19}$$

	B_{33}	B_{11}	B_{22}	B_{12}	c_R	c_L
$0\,\zeta$						
δA	$\frac{3}{8} - \frac{1}{2}\cos 2i + \frac{1}{8}\cos 4i$	$\frac{1}{8}(1 - \cos 4i)$	0	0	1	0
δC	$\frac{3}{8} + \frac{1}{2}\cos 2i + \frac{1}{8}\cos 4i$	$\frac{1}{8}(1 - \cos 4i)$	0	0	1	0
δL	$\frac{1}{2}(1 - \cos 4i)$	$\frac{1}{2}(1 + \cos 4i)$	$\frac{1}{2}(1 + \cos 2i)$	0	1	1
δN	0	0	$\frac{1}{2}(1 - \cos 2i)$	0	1	1
δF	$\frac{1}{4}(1 - \cos 4i)$	$-\frac{1}{4}(1 - \cos 4i)$	0	0	1	0
$1\,\zeta$						
J_c	$4 \sin 2i \cos\zeta$	0	0	0	0	0
J_s	$4 \sin 2i \sin\zeta$	0	0	0	0	0
K_c	$-(2 \sin 2i + \sin 4i)\cos\zeta$	$\sin 4i \cos\zeta$	0	$\frac{1}{2}(\sin i + \sin 3i)\sin\zeta$	0	0
K_s	$-(2 \sin 2i + \sin 4i)\sin\zeta$	$\sin 4i \sin\zeta$	0	$-\frac{1}{2}(\sin i + \sin 3i)\cos\zeta$	0	0
M_c	0	0	$\sin 2i \cos\zeta$	$-\sin i \sin\zeta$	0	0
M_s	0	0	$\sin 2i \sin\zeta$	$-\sin i \cos\zeta$	0	0
$2\,\zeta$						
G_c	$\frac{1}{2}(1 - \cos 4i)\cos 2\zeta$	$\frac{1}{2}(1 + \cos 4i)\cos 2\zeta$	$-\frac{1}{2}(1 + \cos 2i)\cos 2\zeta$	$\frac{1}{2}(\cos i + \cos 3i)\sin 2\zeta$	$\cos 2\zeta$	$\cos 2\zeta$
G_s	$-\frac{1}{2}(1 - \cos 4i)\sin 2\zeta$	$-\frac{1}{2}(1 + \cos 4i)\sin 2\zeta$	$\frac{1}{2}(1 + \cos 2i)\sin 2\zeta$	$\frac{1}{2}(\cos i + \cos 3i)\cos 2\zeta$	$\sin 2\zeta$	$\sin 2\zeta$
B_c	$(\frac{3}{8} - \frac{1}{2}\cos 2i + \frac{1}{8}\cos 4i)\cos 2\zeta$	$\frac{1}{8}(1 - \cos 4i)\cos 2\zeta$	0	$\frac{1}{8}(\cos i - \cos 3i)\sin 2\zeta$	$\cos 2\zeta$	0
B_s	$-(\frac{3}{8} - \frac{1}{2}\cos 2i + \frac{1}{8}\cos 4i)\sin 2\zeta$	$-\frac{1}{8}(1 - \cos 4i)\sin 2\zeta$	0	$\frac{1}{8}(\cos i - \cos 3i)\cos 2\zeta$	$\sin 2\zeta$	0
H_c	$\frac{1}{4}(1 - \cos 4i)\cos 2\zeta$	$-\frac{1}{4}(1 - \cos 4i)\cos 2\zeta$	0	$-\frac{1}{4}(\cos i - \cos 3i)\sin 2\zeta$	$\cos 2\zeta$	0
H_s	$-\frac{1}{4}(1 - \cos 4i)\sin 2\zeta$	$\frac{1}{4}(1 - \cos 4i)\sin 2\zeta$	0	$-\frac{1}{4}(\cos i - \cos 3i)\cos 2\zeta$	$\sin 2\zeta$	0
$3\,\zeta$						
D_c	$(\sin 2i - \frac{1}{2}\sin 4i)\cos 3\zeta$	$\frac{1}{2}\sin 4i \cos 3\zeta$	$-\sin 2i \cos 3\zeta$	$-\frac{1}{4}(\sin i - 3\sin 3i)\sin 3\zeta$	0	0
D_s	$(\sin 2i - \frac{1}{2}\sin 4i)\sin 3\zeta$	$\frac{1}{2}\sin 4i \sin 3\zeta$	$\sin 2i \sin 3\zeta$	$\frac{1}{4}(\sin i - 3\sin 3i)\cos 3\zeta$	0	0
$4\,\zeta$						
E_c	$(\frac{3}{8} - \frac{1}{2}\cos 2i + \frac{1}{8}\cos 4i)\cos 4\zeta$	$\frac{1}{8}(1 - \cos 4i)\cos 4\zeta$	$-\frac{1}{2}(1 - \cos 2i)\cos 4\zeta$	$\frac{1}{4}(\cos i - \cos 3i)\sin 4\zeta$	$\cos 4\zeta$	$\cos 4\zeta$
E_s	$-(\frac{3}{8} - \frac{1}{2}\cos 2i + \frac{1}{8}\cos 4i)\sin 4\zeta$	$-\frac{1}{8}(1 - \cos 4i)\sin 4\zeta$	$\frac{1}{2}(1 - \cos 2i)\sin 4\zeta$	$\frac{1}{4}(\cos i - \cos 3i)\cos 4\zeta$	$\sin 4\zeta$	$\sin 4\zeta$

Table 2.1: Comparison of the directional effects of all 21 independent elastic coefficients on body- and surface-wave phase speeds. The compressional-wave phase speed is given in terms of B_{33} by (2.27), and the shear-wave phase speeds are determined in terms of the coefficients B_{11}, B_{22}, and B_{12} by (2.33). The Rayleigh- and Love-wave phase speeds (c_R & c_L) are determined by (2.1). See Figure 2.1 for the definition of the angle of incidence i and the azimuth ζ. The relationship between these 21 independent elastic parameters and other representations of the elastic tensor may be found in Appendix A.1.

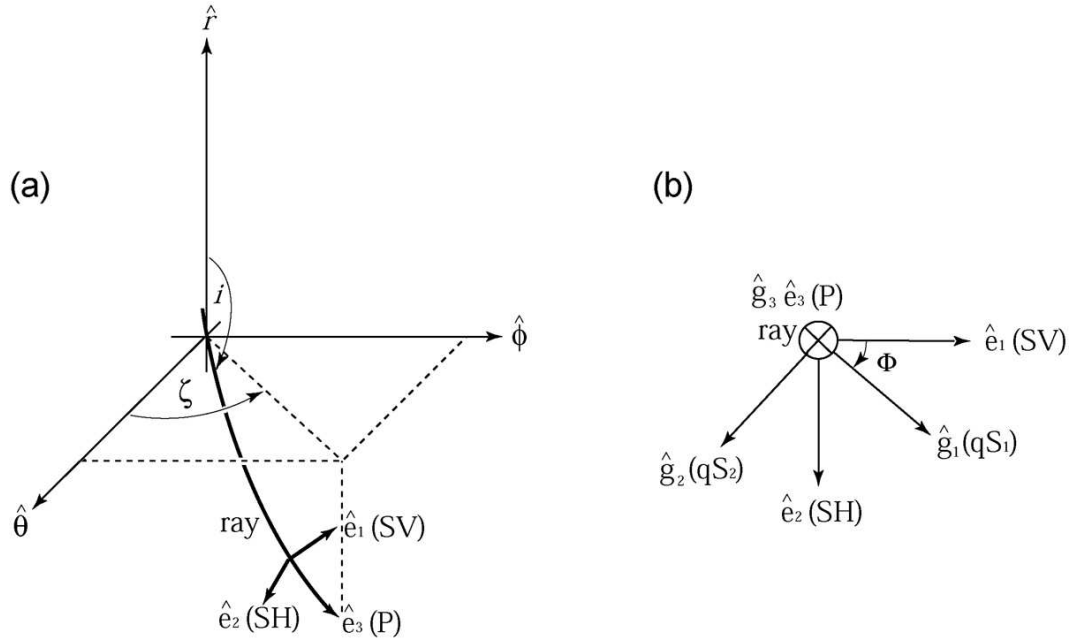

Figure 2.1: Schematic illustration of (a) the local radial, colatitudinal, and longitudinal directions r, θ, ϕ at an arbitrary point along a ray in the isotropic reference model; and (b) the polarization directions of unperturbed P, SV, and SH waves (given by equations 2.20, 2.21, and 2.22, respectively) and perturbed fast (qS_1) and slow (qS_2) shear waves (given by 2.23). Note the angle of incidence $0 \leq i \leq \pi$ is measured downward from vertical, whereas the azimuth $0 \leq \zeta \leq 2\pi$ is measured counterclockwise from due south; the polarization angle Φ is measured counterclockwise from the SV polarization direction ($\hat{\mathbf{e}}_1$) in a right-handed coordinate system. Note that the SH polarization vector ($\hat{\mathbf{e}}_2$) is a tangent vector.

where ρ denotes the density, κ and μ the bulk and shear moduli, respectively, and the slowness vector is given by $\mathbf{p} = p\hat{\mathbf{p}} = \boldsymbol{\nabla} T$, where $p = |\mathbf{p}|$, T denotes the traveltime, and $\hat{\mathbf{p}}$ the slowness direction. Note that in an isotropic medium the slowness vector is normal to the wavefront.

Following the convention of *Dahlen and Tromp* [1998], let us introduce the local angle of incidence i and the local azimuth ζ of the unperturbed ray, as illustrated in Figure 2.1a. The unperturbed slowness direction $\hat{\mathbf{p}}$ along this ray may be expressed in terms of these angles as

$$\hat{\mathbf{p}} = \cos i\, \hat{\mathbf{r}} + \sin i \cos \zeta\, \hat{\boldsymbol{\theta}} + \sin i \sin \zeta\, \hat{\boldsymbol{\phi}}, \tag{2.20}$$

where $\hat{\mathbf{r}}$, $\hat{\boldsymbol{\theta}}$, and $\hat{\boldsymbol{\phi}}$ denote unit vectors in the directions of increasing radius r, colatitude θ, and longitude ϕ, respectively.

The unperturbed isotropic reference model supports P, SV, and SH waves. We label the eigenvalues c_m, $m = 1, 2, 3$, and the associated eigenvectors $\hat{\mathbf{g}}_m$, $m = 1, 2, 3$, such that $c_1 = c_2 = (\mu/\rho)^{1/2}$ denote the degenerate SH- and SV-wave phase speeds and $c_3 = [(\kappa + \frac{4}{3}\mu)/\rho]^{1/2}$ the P-wave phase speed.

As a consequence of the shear-wave degeneracy, the eigenvectors associated with the two shear waves are non-unique: any polarization vector perpendicular to the ray is acceptable. Two such vectors are

$$\hat{\mathbf{e}}_1 = -\sin i\,\hat{\mathbf{r}} + \cos i \cos\zeta\,\hat{\boldsymbol{\theta}} + \cos i \sin\zeta\,\hat{\boldsymbol{\phi}}, \tag{2.21}$$

$$\hat{\mathbf{e}}_2 = -\sin\zeta\,\hat{\boldsymbol{\theta}} + \cos\zeta\,\hat{\boldsymbol{\phi}}. \tag{2.22}$$

Note that the vector (2.22) is a tangent vector, i.e., it has no vertical component, which is why we refer to this direction as the SH polarization, whereas (2.21) is referred to as the SV polarization. In a spherically symmetric Earth model with first- and second-order radial discontinuities (e.g., PREM), the SH wave with a polarization defined by (2.22) is completely decoupled from the P-SV motion involving the SV polarization (2.21).

More generally, the eigenvectors may be written as a linear combination of the particular vectors (2.21) and (2.22):

$$\hat{\mathbf{g}}_1 = \cos\Phi\,\hat{\mathbf{e}}_1 + \sin\Phi\,\hat{\mathbf{e}}_2, \qquad \hat{\mathbf{g}}_2 = -\sin\Phi\,\hat{\mathbf{e}}_1 + \cos\Phi\,\hat{\mathbf{e}}_2, \tag{2.23}$$

where Φ denotes an arbitrary rotation angle in the plane orthogonal to the ray. The unique eigenvector associated with the P wave is the same as the slowness (ray) direction $\hat{\mathbf{p}}$:

$$\hat{\mathbf{g}}_3 = \hat{\mathbf{e}}_3 = \hat{\mathbf{p}} = \cos i\,\hat{\mathbf{r}} + \sin i \cos\zeta\,\hat{\boldsymbol{\theta}} + \sin i \sin\zeta\,\hat{\boldsymbol{\phi}}. \tag{2.24}$$

Next, we superimpose a weak anisotropic perturbation on the isotropic reference model to obtain a weakly anisotropic model. Wave propagation in such a model is controlled by the perturbed Christoffel equation [e.g., *Jech and Pšenčík*, 1989; *Červený*, 2001; *Chapman*,

2004]

$$[\mathbf{\Gamma} + \delta\mathbf{\Gamma} - (c_m^2 + 2c_m\delta c_m)\mathbf{I}] \cdot (\hat{\mathbf{g}}_m + \delta\hat{\mathbf{g}}_m) = \mathbf{0}. \tag{2.25}$$

The symmetric matrix $\delta\mathbf{\Gamma}$ is given by

$$\delta\mathbf{\Gamma} = \hat{\mathbf{p}} \cdot \delta\mathbf{a} \cdot \hat{\mathbf{p}} + (\kappa + \tfrac{1}{3}\mu)[(\delta\hat{\mathbf{p}})\hat{\mathbf{p}} + \hat{\mathbf{p}}(\delta\hat{\mathbf{p}})]/\rho, \tag{2.26}$$

where $\delta\mathbf{a}$ is defined in terms of the perturbed fourth-order elastic tensor $\delta\mathbf{c}$ and the perturbed density $\delta\rho$ by $\delta\mathbf{a} = \delta(\mathbf{c}/\rho)$.

The compressional wave is non-degenerate, and thus we can obtain its perturbed relative phase speed $\delta c_3/c_3$ directly by taking the dot product of (2.25) for $m = 3$ with $\hat{\mathbf{g}}_3$, invoking the transpose of the unperturbed Christoffel equation (2.18) for $m = 3$ [*Jech and Pšenčík*, 1989]:

$$(\delta c_3/c_3) = (2c_3^2)^{-1} B_{33}, \tag{2.27}$$

where

$$B_{33} = \hat{\mathbf{g}}_3\hat{\mathbf{p}} \colon \delta\mathbf{a} \colon \hat{\mathbf{p}}\hat{\mathbf{g}}_3. \tag{2.28}$$

In obtaining (2.27), we have used the fact $\hat{\mathbf{g}}_3 \cdot \mathbf{\Gamma} \cdot \hat{\mathbf{g}}_3 = c_3^2$, and that $\hat{\mathbf{g}}_3 \cdot \delta\hat{\mathbf{p}} = \hat{\mathbf{p}} \cdot \delta\hat{\mathbf{p}} = 0$ because the perturbed slowness $\hat{\mathbf{p}} + \delta\hat{\mathbf{p}}$ is a unit vector. Equation (2.27) determines the phase speed of the quasi-P wave in a weakly anisotropic Earth model. Using the explicit dependence of the polarization vector $\hat{\mathbf{g}}_3$ on the angles i and ζ given by (2.24), (2.28) may be written in the general form

$$B_{33} = \sum_{n=0}^{4} \big[a_n(i)\cos n\zeta + b_n(i)\sin n\zeta\big]. \tag{2.29}$$

The coefficients $a_n(i)$ and $b_n(i)$ may be expressed as

$$a_n(i) = \begin{cases} \sum_{l=0,2,4} \alpha_{nl} \cos li, & n = 0, 2, 4, \\ \\ \sum_{l=2,4} \alpha_{nl} \sin li, & n = 1, 3, \end{cases} \qquad b_n(i) = \begin{cases} \sum_{l=0,2,4} \beta_{nl} \cos li, & n = 2, 4, \\ \\ \sum_{l=2,4} \beta_{nl} \sin li, & n = 1, 3. \end{cases} \tag{2.30}$$

Explicit expressions for the B_{33} coefficients α_{nl} and β_{nl} are tabulated in Appendix A.1. The coefficients a_{nl} and b_{nl} given by (2.30) are an even Fourier series in the local angle of incidence i. However, unlike surface waves, the azimuthal (ζ) dependence of quasi P waves involves both even and odd Fourier terms.

For the degenerate shear waves we dot (2.25) for $m = 1, 2$ with $\hat{\mathbf{e}}_l$, $l = 1, 2$, invoking the transpose of the unperturbed Christoffel equation (2.18) for $m = 1, 2$, to obtain the two sets of equations [e.g., *Jech and Pšenčík*, 1989; *Červený*, 2001; *Chapman*, 2004]

$$\begin{pmatrix} B_{11} - 2c\delta c_1 & B_{12} \\ B_{21} & B_{22} - 2c\delta c_1 \end{pmatrix} \begin{pmatrix} \cos\Phi \\ \sin\Phi \end{pmatrix} = 0,$$
$$\begin{pmatrix} B_{11} - 2c\delta c_2 & B_{12} \\ B_{21} & B_{22} - 2c\delta c_2 \end{pmatrix} \begin{pmatrix} -\sin\Phi \\ \cos\Phi \end{pmatrix} = 0, \tag{2.31}$$

where $c = c_1 = c_2$. The symmetric 2×2 matrix elements B_{lm} are given by

$$B_{lm} = \hat{\mathbf{e}}_l \hat{\mathbf{p}} : \delta\mathbf{a} : \hat{\mathbf{p}} \hat{\mathbf{e}}_m, \tag{2.32}$$

where we have used the fact that $\hat{\mathbf{p}} \cdot \hat{\mathbf{e}}_m = 0$, $m = 1, 2$. The solubility condition for the problem (2.31) implies that the perturbed shear-wave phase speeds are [*Jech and Pšenčík*, 1989]

$$\delta c_{1,2}/c = (4c^2)^{-1}(B_{11} + B_{22} \pm B), \tag{2.33}$$

where B is given by

$$B = [(B_{11} - B_{22})^2 + 4B_{12}^2]^{1/2}. \tag{2.34}$$

Labeling the shear waves in terms of decreasing speed, the plus sign in (2.33) goes with δc_1 and the minus sign with δc_2. The orthonormal eigenvectors of the 2×2 problems (2.31) associated with the eigenvalues (2.33) are determined by

$$\tan 2\Phi = \frac{2B_{12}}{B_{11} - B_{22}}. \tag{2.35}$$

We conclude that the weak anisotropy removes the degeneracy, and, given the polarization

angle Φ determined by (2.35), the unique anisotropic shear-wave polarization directions $\hat{\mathbf{g}}_1$ and $\hat{\mathbf{g}}_2$ are determined by (2.23) (Figure 2.1b). As noted by *Chapman* [2004], the isotropic polarizations depend on the ray history, whereas, the weakly anisotropic polarizations are determined solely based upon the local weak anisotropy, i.e., there is no dependence on the history of the ray. Of course this is an asymptotic, high-frequency result, and in finite-frequency simulations, e.g., the numerical experiments presented in later sections of the paper, the polarization will have some memory. We will refer to the shear wave polarized in the $\hat{\mathbf{g}}_1$ direction as the qS_1 wave (the fast shear wave) and to the shear wave polarized in the $\hat{\mathbf{g}}_2$ direction as the qS_2 wave (the slow shear wave). We restrict the value of Φ to the domain $(-90^\circ, 90^\circ]$, since the principal value of 2Φ is obtained by taking the arc tangent of (2.35). Note that when $B_{12} = 0$ the polarization angle Φ equals 0° or 90°. When $\Phi = 0^\circ$ we have $\hat{\mathbf{g}}_1 = \hat{\mathbf{e}}_1$ (the SV polarization), $B_{11} > B_{22}$, and $\delta c_1/c = (2c^2)^{-1}B_{11}$, whereas $\hat{\mathbf{g}}_2 = \hat{\mathbf{e}}_2$ (the SH polarization) and $\delta c_2/c = (2c^2)^{-1}B_{22}$. Alternatively, when $\Phi = 90^\circ$ we have $\hat{\mathbf{g}}_1 = \hat{\mathbf{e}}_2$ (the SH polarization), $B_{11} < B_{22}$, and $\delta c_1/c = (2c^2)^{-1}B_{22}$, whereas $\hat{\mathbf{g}}_2 = -\hat{\mathbf{e}}_1$ (the negative SV polarization) and $\delta c_2/c = (2c^2)^{-1}B_{11}$.

Like B_{33} in (2.29), the shear-wave elements B_{lm}, $l, m = 1, 2$, may be written in the general form

$$B_{lm} = \sum_{n=0}^{4} \big[a_n(i) \cos n\zeta + b_n(i) \sin n\zeta\big]. \tag{2.36}$$

For the two parameters B_{11} and B_{22} the coefficients $a_n(i)$ and $b_n(i)$ may be expressed in the form (2.30):

$$a_n(i) = \begin{cases} \sum_{l=0,2,4} \alpha_{nl} \cos li, & n = 0, 2, 4, \\ \\ \sum_{l=2,4} \alpha_{nl} \sin li, & n = 1, 3, \end{cases} \qquad b_n(i) = \begin{cases} \sum_{l=0,2,4} \beta_{nl} \cos li, & n = 2, 4, \\ \\ \sum_{l=2,4} \beta_{nl} \sin li, & n = 1, 3, \end{cases} \tag{2.37}$$

i.e., they are an even Fourier series in the local angle of incidence i. However, for the

parameter B_{12} we have

$$a_n(i) = \begin{cases} \sum_{l=1,3} \alpha_{nl} \cos li, & n = 2, 4, \\ \\ \sum_{l=1,3} \alpha_{nl} \sin li, & n = 1, 3, \end{cases} \qquad b_n(i) = \begin{cases} \sum_{l=1,3} \beta_{nl} \cos li, & n = 2, 4, \\ \\ \sum_{l=1,3} \beta_{nl} \sin li, & n = 1, 3, \end{cases} \tag{2.38}$$

i.e., they are an odd Fourier series in the local angle of incidence i. The shear-wave coefficients α_{nl} and β_{nl} associated with B_{11}, B_{22}, and B_{12} are tabulated in Appendix A.1.

Note that although the coefficients B_{lm} given by (2.36) are simple Fourier series, the dependence of the shear-wave phase-speed perturbations (2.33) on B induces a more complicated directional dependence. In contrast, the surface-wave phase speeds (2.1) and the compressional-wave phase speed (2.27) do have a directional dependence that is characterized by a simple Fourier series.

The elements B_{mm}, $m = 1, 2, 3$, exhibit the symmetry $B_{mm}(i, \zeta) = B_{mm}(\pi - i, \zeta + \pi)$, whereas the element B_{12} exhibits the anti-symmetry $B_{12}(i, \zeta) = -B_{12}(\pi - i, \zeta + \pi)$. But because the perturbed shear-wave phase speed (2.33) depends on B_{12}^2, the body-wave phase speeds (2.27) and (2.33) exhibit the local symmetry

$$(\delta c/c)(i, \zeta) = (\delta c/c)(\pi - i, \zeta + \pi), \tag{2.39}$$

which implies that body waves travel with the same phase speed in opposite directions along the same ray.

Table 2.1 categorizes the effects of the 21 elastic parameters that affect body-wave propagation in terms of the five (transversely isotropic) 0ζ perturbations δA, δC, δL, δN, and δF, the six 1ζ parameters J_c, J_s, K_c, K_s, M_c, and M_s, the six 2ζ parameters G_c, G_s, B_c, B_s, H_c, and H_s, the two 3ζ parameters D_c and D_s, and the two 4ζ parameters E_c and E_s (see Appendix A.1 for expressions in terms of the elements of the elastic tensor c_{ijkl}).

Given the perturbed body-wave phase speeds (2.27) and (2.33) and the perturbed Christoffel equation (2.25), *Jech and Pšenčík* [1989] demonstrate how one may obtain the perturbed polarization directions $\delta\hat{\mathbf{g}}_m$. We shall not need these perturbations in this study, which is why they are omitted.

The perturbed traveltime may be obtained based upon an integration along the unperturbed, isotropic ray [*Červený*, 2001; *Chapman*, 2004]:

$$\delta T = \int \delta\mathbf{p}\cdot d\mathbf{r} = \int \delta(\hat{\mathbf{p}}/c)\cdot d\mathbf{r} = -\int (\delta c/c^2)\hat{\mathbf{p}}\cdot d\mathbf{r} + \int (1/c)\delta\hat{\mathbf{p}}\cdot d\mathbf{r} = -\int (\delta c/c^2)\, d\,\mathrm{ray}, \tag{2.40}$$

where we have used the fact that along the isotropic reference ray $\delta\hat{\mathbf{p}}\cdot d\mathbf{r} = 0$, i.e., the perturbed slowness is perpendicular to the unperturbed isotropic reference ray, and the unperturbed slowness $\hat{\mathbf{p}}$ is parallel to the reference ray. As shown by *Backus* [1965], in a weakly anisotropic medium the directional dependence of the group speed is the same as the directional dependence of the phase speed. For this reason it is the relative perturbation in phase speed that occurs in (2.40). For quasi-P (qP) waves one uses (2.27) in (2.40), whereas for fast (qS_1) and slow (qS_2) shear waves one uses (2.33). It is interesting, and perhaps surprising, that, for an isotropic reference model, (2.40) implies that one can compute traveltime perturbations in weakly anisotropic media without accounting for group speed or polarization perturbations.

The differential traveltime between the two shear waves, i.e., the amount of shear-wave splitting, may be expressed as [e.g., *Červený*, 2001, 3.9.24]

$$\Delta T = |\delta T_2 - \delta T_1| = \int B/(2c^3)\, d\,\mathrm{ray}. \tag{2.41}$$

In the context of near-vertically traveling SKS waves, we show in Appendix A.1 that the split time ΔT and the polarization direction Φ constrain the degree-two G_c and G_s parameters.

2.4 Numerical Simulations

In this section we compare spectral-element simulations of global and regional seismic wave propagation in idealized, weakly anisotropic media against our theoretical predictions. The global spectral-element method (SEM) developed and implemented by *Komatitsch and Tromp* [2002a] incorporates spherically symmetric transversely isotropic PREM

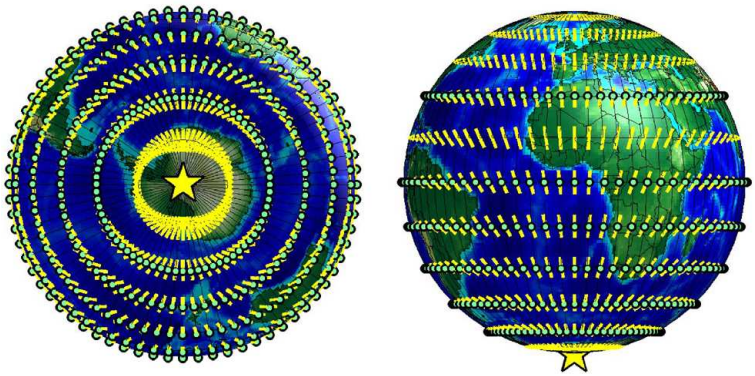

Figure 2.2: Global experimental setup. For surface-wave simulations, the source is a pure strike-slip event located at the South Pole at a depth of 15 km (yellow star), and surface waves are recorded by a ring of equidistant stations (green circles) with an epicentral distance of 120°. For body-wave simulations, the source (yellow star) is replaced by a vertical point force located at a depth of 600 km, and body waves are recorded by five rings of equidistant stations (green circles) with epicentral distances of 30°, 45°, 60°, 75° and 90°, respectively, with a longitudinal inter-station spacing of 5°. In our experiments, the theoretically predicted fast axis of the anisotropy projected onto the unit sphere, indicated by the yellow dashes, makes a constant angle with a given meridian/raypath. Thus, for a given source-receiver combination the direction of the projected fast axis makes a constant angle with the projection of the raypath onto the unit sphere, and the ray azimuth ζ has a constant value of π (see Figure 2.1a). In this figure the longitudinal variation of the direction of the projected fast axis is given by a degree two Fourier series; we will also consider degree one, three, and four variations (see equations 2.42–2.49 for the prescribed longitudinal variation associated with a particular elastic parameter pair). The background model is transversely isotropic PREM for surface-wave simulations and isotropic PREM for body-wave simulations, upon which we superimpose constant anisotropy at the 5% level throughout the upper mantle. Left: map view. Right: side view.

[*Dziewonski and Anderson*, 1981], and because the SEM is based upon Cartesian coordinates the corresponding simulations involve a full Cartesian elastic tensor. The incorporation of completely general anisotropy in the global and regional SEM mesh generators and solvers is therefore relatively straightforward. From a numerical perspective, the main issue is that the memory requirements increase ten-fold relative to an isotropic simulation, and five-fold relative to a transversely isotropic simulation.

2.4.1 Global Simulations

The global experimental setup is depicted in Figure 2.2. The reference model is transversely isotropic PREM [*Dziewonski and Anderson*, 1981] for surface-wave simulations and isotropic PREM for body-wave simulations. The epicenter is located at the South Pole, and thus the source azimuth Ψ is the initial take-off azimuth, measured clock-wise from the prime meridian (i.e., 0° longitude). Concentric rings of equidistant receivers are located at epicentral distances of 30°, 45°, 60°, 75°, 90°, and 120°, with a longitudinal inter-station spacing of 5°. Because the unperturbed surface- and body-wave raypaths lie along a meridian/in the meridional plane, the ray azimuth ζ has a constant value of π (see Figure 2.1a). In each numerical experiment only one particular cosine-sine pair (e.g., G_c and G_s) listed in Table 2.1 is non-zero. This approach enables us to determine whether or not this particular parameter pair has the theoretically expected effect on surface-wave phase and body-wave traveltime. In our experiments, the theoretically predicted fast axis of the anisotropy projected onto the unit sphere makes a constant angle with each great circle, i.e., with each meridian. At a given latitude, the longitudinal variation of the direction of the fast axis is given by a degree two or four Fourier series, depending on the theoretically expected directional dependence tabulated in Table 2.1. So along any given meridian, the pairs J_c & J_s, K_c & K_s, M_c & M_s, G_c & G_s, B_c & B_s, H_c & H_s, D_c & D_s, or E_c & E_s are combined to produce the desired fast direction, with source azimuthal variations of degree one, two, three, or four, i.e,

$$J_c = J\cos(\Psi), \qquad J_s = J\sin(\Psi), \tag{2.42}$$

$$K_c = K\cos(\Psi), \qquad K_s = K\sin(\Psi), \tag{2.43}$$

$$M_c = M\cos(\Psi), \qquad M_s = M\sin(\Psi), \tag{2.44}$$

$$G_c = G\cos(2\Psi), \qquad G_s = G\sin(2\Psi), \tag{2.45}$$

$$B_c = B\cos(2\Psi), \qquad B_s = B\sin(2\Psi), \tag{2.46}$$

$$H_c = H\cos(2\Psi), \qquad H_s = H\sin(2\Psi), \tag{2.47}$$

$$D_c = D\cos(3\Psi), \qquad D_s = D\sin(3\Psi), \tag{2.48}$$

$$E_c = E\cos(4\Psi), \qquad E_s = E\sin(4\Psi). \tag{2.49}$$

For a particular elastic parameter pair in Table 2.1, constant anisotropy defined as J/A, K/A, M/N, G/L, B/A, H/F, D/L, or E/N at a level of 5% is superimposed on PREM throughout the entire upper mantle, i.e., between the Moho (24.4 km) and the 670 km discontinuity. In the context of body waves, note that in isotropic PREM $A = C = \kappa + \frac{4}{3}\mu$, $L = N = \mu$ and $F = \kappa - \frac{2}{3}\mu$, where κ and μ denote the reference bulk and shear moduli, respectively.

2.4.1.1 Surface Waves

For the surface-wave simulations a vertical strike-slip source is located at the South Pole at a depth of 15 km and waves are recorded at an epicentral distance of 120° by an equidistant ring of stations with a longitudinal inter-station spacing of 5°, as illustrated in Figure 2.2. Along the ring of stations we expect, based upon the theory discussed in Section 2.3 and the direction of the fast axis determined by (2.45)–(2.47) and (2.49), that the surface-wave phase speed exhibits anomalies varying as a degree two ($G_{c,s}$, $B_{c,s}$ and $H_{c,s}$) or four ($E_{c,s}$) Fourier series with source azimuth, i.e., with longitude. We calculated spectral-element synthetics for transversely isotropic PREM as well as for the anisotropic models. These SEM synthetics are accurate at periods of 36 s and longer. These parallel calculations take approximately 12 hours on 150 processors of a PC cluster for 4500 s long synthetic seismograms.

Equation (2.1) describes the directional dependence of surface-wave phase speed for a particular mode branch at a particular frequency. Making a surface-wave phase anomaly measurement (2.17) requires us to isolate this mode branch from other signals. We accomplish this based upon a phase-matched filtering technique described in detail by *Ekström et al.* [1997].

In Figure 2.3 we compare theoretical path-averaged phase-speed anomalies $\delta\bar{c}/c$ defined by (2.17) with SEM estimates. For the $G_{c,s}$, $B_{c,s}$ and $H_{c,s}$ anisotropic parameters we expect a 2ζ directional dependence for the Rayleigh wave (see Table 2.1 and equations 2.45, 2.46, and 2.47). The theoretical predictions indicated by the black (50 s) and red

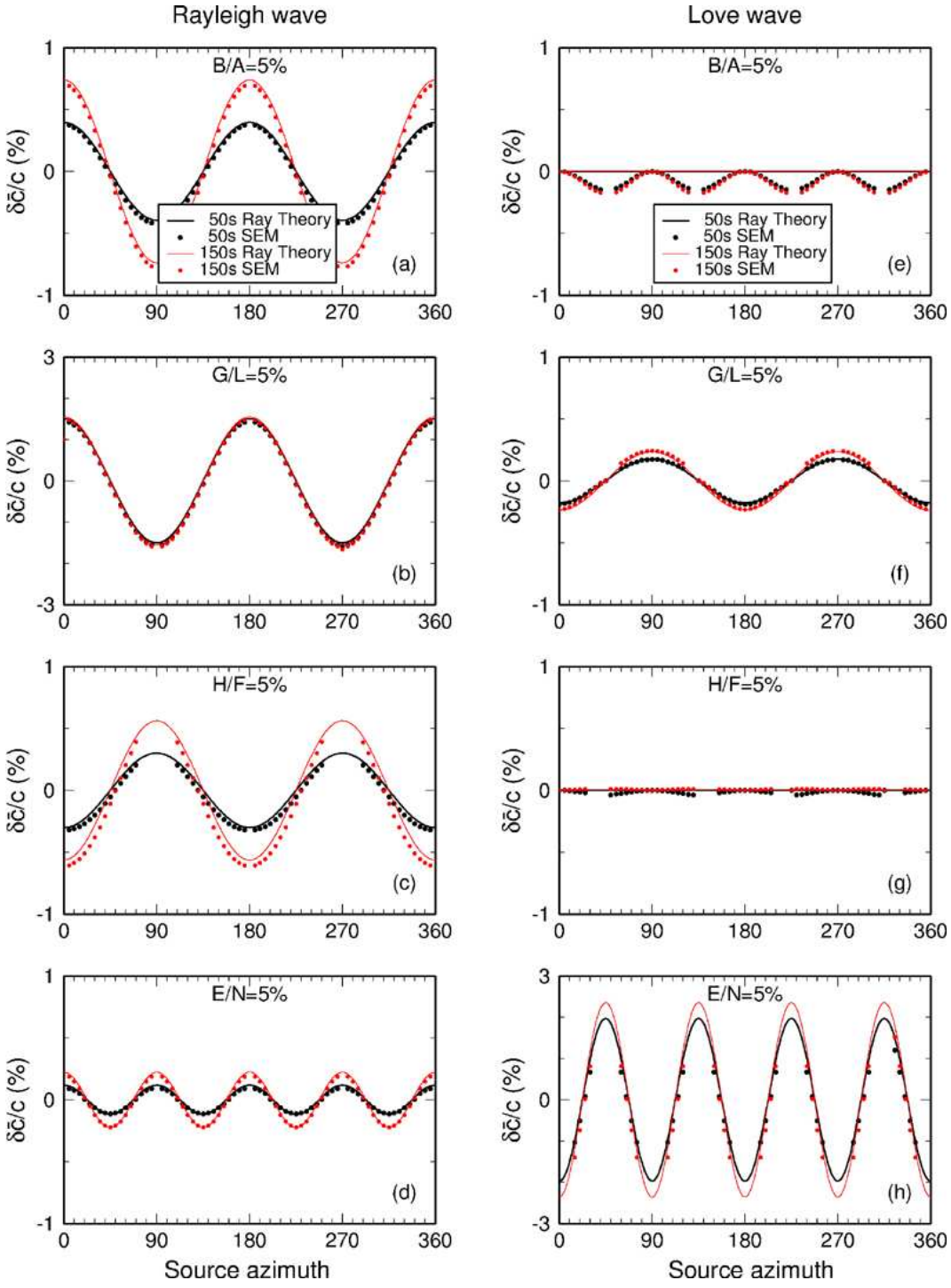

Figure 2.3: Path-averaged surface-wave phase-speed anomalies $\delta\bar{c}/c$ defined by (2.17) due to 5% perturbations of particular combinations of the anisotropic parameters $G_{c,s}$, $B_{c,s}$, $H_{c,s}$, and $E_{c,s}$ given by (2.45)–(2.47) and (2.49) are shown for fundamental 50 s (black lines and symbols) and 150 s (red lines and symbols) Love waves (left column) and Rayleigh waves (right column) at an epicentral distance of 120°. The solid black and red lines denote theoretical predictions of the path-averaged phase-speed anomaly calculated from (2.1) and (2.17). The black and red symbols denote measurements of the actual surface-wave phase anomalies determined from the spectral-element synthetics based upon a phase-matched filtering technique. See Figure 2.2 for the geometry of the experiment, Table 2.1 for the expected local azimuthal behavior, and Appendix A.1 for the relationship between these coefficients and the elements of the elastic tensor. We use the phase-matched filtering technique of *Ekström et al.* [1997] to determine the phase anomalies.

(150 s) solid lines are in excellent agreement with the SEM calculations denoted by the corresponding black and red symbols. Love waves are theoretically expected to be unaffected by the $B_{c,s}$ and $H_{c,s}$ anisotropic parameters, whereas the $G_{c,s}$ parameters introduce a 2ζ directional dependence. Indeed the SEM measurements confirm that the Love-wave phase anomalies for the parameters $B_{c,s}$ and $H_{c,s}$ are very small, and the theoretical predictions for the $G_{c,s}$ parameters are in good agreement with the SEM calculations. Notice that the amplitude of the Love-wave phase anomaly is roughly six times smaller than that of the Rayleigh wave for the $G_{c,s}$ parameters, which implies that the Love wave is basically insensitive to 2ζ variations, as noted by *Montagner and Nataf* [1986]. The $E_{c,s}$ parameters are expected to introduce 4ζ variations in both the Love- and the Rayleigh-wave phase (see Table 2.1 and equation 2.49). Again the asymptotic theory and the SEM calculations are in very good agreement. Note that the amplitude of the Rayleigh-wave phase anomaly is roughly eight times smaller than for the Love wave. Small gaps in the Rayleigh- and Love-wave phase-anomaly measurements for the spectral-element synthetics correspond to nodes in the pure strike-slip radiation pattern.

2.4.1.2 Body Waves

For the body-wave simulations a vertical point force is located at the South Pole at a depth of 600 km, and waves are recorded at five rings of equidistant stations at epicentral distances of 30°, 45°, 60°, 75°, and 90°, with a longitudinal inter-station spacing of 5°, as indicated by green circles in Figure 2.2. The vertical point force avoids waveform complexities associated with the radiation pattern. The source-time function is a Ricker wavelet with a 3 s half-duration. According to the theory discussed in Section 2.3, we expect that for a given ring the body-wave phase speed varies as a degree one, two, three, or four Fourier series with source azimuth as prescribed by (2.42)–(2.49).

We calculated SEM synthetics accurate at periods of 9 s and longer for isotropic PREM as well as for the anisotropic models. These calculations take approximately 4.5 hours on 600 processors for 1500 s long seismograms. The anisotropic models are implemented by perturbing one of the eight pairs of generic anisotropic parameters according to (2.42)–(2.49). Along each body-wave raypath the ray direction ζ equals π (see Figure 2.1a), and

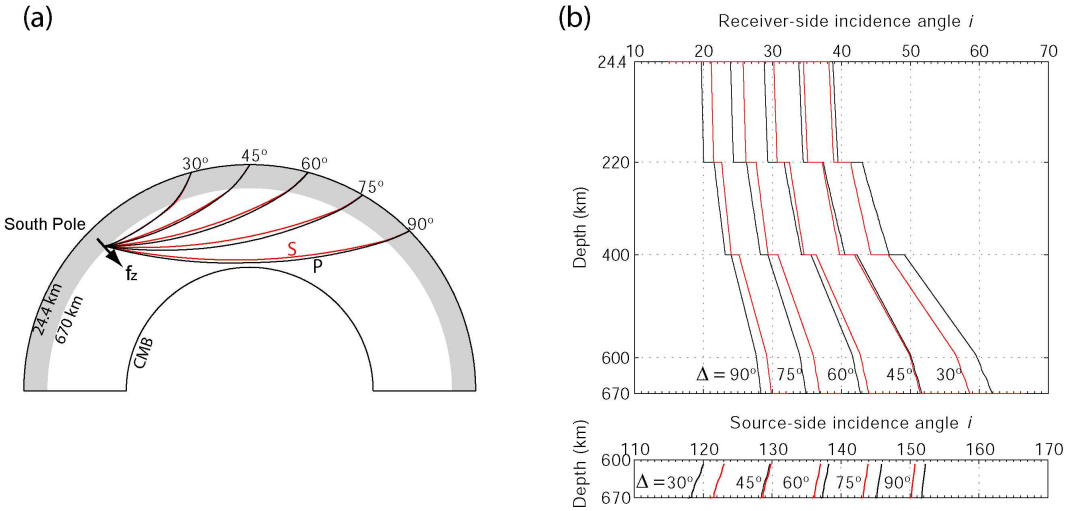

Figure 2.4: (a) Raypaths of P waves (black) and S waves (red) at epicentral distances of 30°, 45°, 60°, 75° and 90°. The vertical point force (f_z) used for the global body-wave simulations is indicated by the black arrow. The perturbed anisotropic region is in the depth range from 24.4–670 km, which is highlighted in gray. At any given depth, the longitudinal variation of the direction of the theoretically predicted fast axis projected onto the unit sphere is given by a degree one, two, three, or four Fourier series in source azimuth as defined by equations (2.42)–(2.49) and illustrated in Figure 2.2 for a degree-two variation. Thus, for any given raypath the direction of the projected fast axis makes a constant angle with the ray plane (i.e., a meridional plane). (b) The body-wave ray incidence angle i (defined in Figure 2.1a) in the anisotropic upper mantle (24.4–670 km). Top: receiver-side incidence angle; bottom: source-side incidence angle. P wave rays are shown in black and S wave rays are shown in red for various epicentral distances.

thus, according to Table 2.1, all cosine-parameters (i.e., J_c, K_c, M_c, G_c, B_c, H_c, D_c, and E_c) are solely determined by B_{11}, B_{22}, and B_{33}, and all sine-parameters (i.e., J_s, K_s, M_s, G_s, B_s, H_s, D_s, and E_s) are solely determined by B_{12}. We known from (2.35) that B_{12} controls the polarization angle, and therefore for non-zero values of B_{12} we obtain non-degenerate shear waves with polarizations that deviate from the unperturbed SV and SH polarizations defined by (2.21) and (2.22). Figure 2.4a shows the P- and S-wave ray geometry for various epicentral distances. In the anisotropic upper mantle the P- and S-wave raypaths almost overlap, and the difference in incidence angle i between the P and S waves is less than 3°, as illustrated in Figure 2.4b. The theoretical traveltime anomalies are calculated along the unperturbed P or S raypaths based upon (2.40) and (2.27) or (2.33). Figure 2.5 shows isotropic and anisotropic shear waveforms on the unperturbed SV and SH polarization directions defined by (2.21) and (2.22) as well as the perturbed polarization di-

rections $\hat{\mathbf{g}}_1$ and $\hat{\mathbf{g}}_2$ determined by (2.23) and (2.35). The vertical point source does not produce a noticeable shear wave on the SH components in the isotropic reference model, but we see a clear arrival on the SH component in the anisotropic model. Note that the anisotropic shear waveforms on the perturbed polarization directions are similar in shape to the unperturbed shear waveforms, i.e., the fast and slow waveforms are cleanly split, which facilitates cross-correlation differential traveltime measurements. Figure 2.7 shows that the traveltime anomalies, which are measured based upon cross-correlation between the anisotropic and isotropic synthetics, fit the theoretical predictions quite well for all anisotropic parameters pairs at all five epicentral distances. Fast (qS_1) and slow (qS_2) shear waves are well separated as measured by cross-correlation. The body-wave traveltime anomalies exhibit π-periodicity (J, K, M), $\pi/2$-periodicity (G, B, H), $\pi/3$-periodicity (D), and $\pi/4$-periodicity (E) for different anisotropic models, in accordance with (2.42)–(2.49). Note that the $J_{c,s}$ pair (2.42) has the biggest effect on the traveltime of the P wave, while having negligible effects on the S wave, and that the magnitude of the P-wave traveltime anomaly decreases with increasing distance. The pair $K_{c,s}$ (2.43) has a significant effect on P, qS_1, and qS_2 waves, whereas the pair $M_{c,s}$ (2.44) affects qS_1 and qS_2 waves but not P waves, and the differential traveltime between qS_1 and qS_2 decreases with increasing epicentral distance. The degree-two pairs $G_{c,s}$, $B_{c,s}$, and $H_{c,s}$ induce comparable traveltime anomalies at the ± 3 s level for the S waves and the ± 1 s level for the P wave. The degree-three pair $D_{c,s}$ (2.48) induces almost the same magnitude traveltime anomaly for the shear waves as the degree-one pair $M_{c,s}$. The pair $E_{c,s}$ (2.49) has a relatively small effect in terms of shear-wave splitting at larger epicentral distances ($\Delta > 60^\circ$), and a minimal effect on P waves.

Before making the cross-correlation traveltime measurements, the three-component isotropic and anisotropic synthetics are rotated onto to the polarization directions of the (orthogonal) P, qS_1, and qS_2 components (illustrated in Figure 2.1b). The P-wave polarization direction is determined by the incidence angle of the P-wave at the surface. The shear-wave polarization angle Φ is calculated for the last anisotropic layer traversed by the ray based upon (2.35), as illustrated in Figure 2.6. As discussed in Section 2.3.2, under the assumption of weak anisotropy the S-wave polarizations are determined solely based

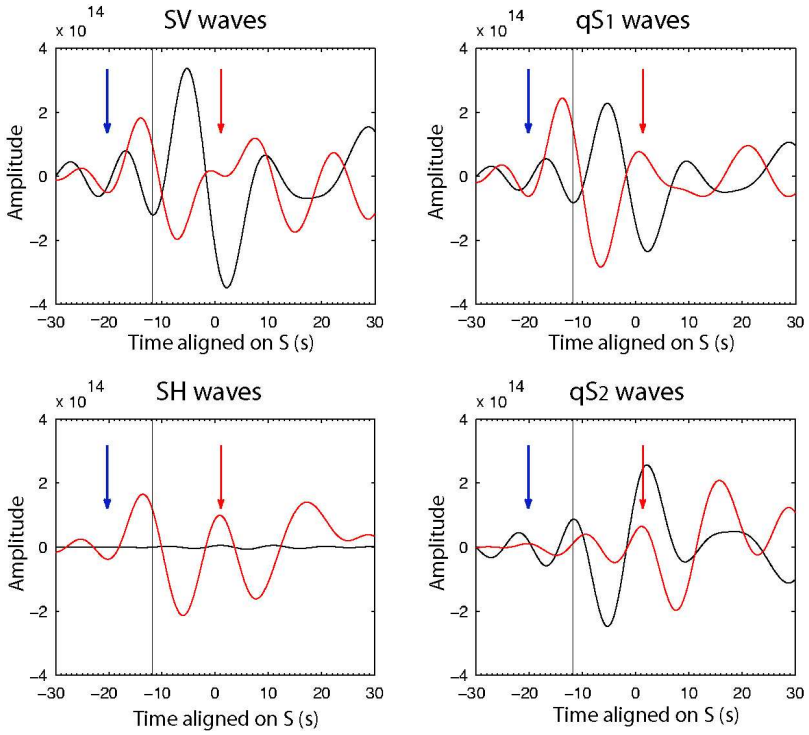

Figure 2.5: Shear waveforms for isotropic PREM (black lines) and an anisotropic model (red lines) determined by the degree-one parameter (2.43) with $K/A = 5\%$ throughout the entire upper mantle. The station is located at a source azimuth of 90° and an epicentral distance of 75°. All seismograms are aligned on the direct S arrival predicted by IASP91 [*Kennett and Engdahl*, 1991]. Vertical lines indicate the reference S arrival time in isotropic PREM. Blue arrows indicate the predicted qS_1 (fast) arrival time and red arrows indicate the predicted qS_2 (slow) arrival time, both relative to the isotropic reference arrival time. Left column: shear waveforms on the unperturbed polarization directions ($\hat{\mathbf{e}}_1$ and $\hat{\mathbf{e}}_2$ defined by 2.21 and 2.22). The vertical point source does not generate an SH wave in the isotropic reference model in the lower left panel (black line). The anisotropic S wave has non-zero double arrivals on the SV and SH components (red lines). Right column: shear waveforms on the perturbed polarization directions ($\hat{\mathbf{g}}_1$ and $\hat{\mathbf{g}}_2$ defined in 2.23). The isotropic reference shear wave is clearly visible on both the qS_1 and the qS_2 components (black lines). The anisotropic shear wave nicely separates on these components, with a fast shear-wave arrival on the qS_1 component and a slow shear-wave arrival on the qS_2 component (red lines), as predicted by (2.23) and (2.35). Note that on the qS_1 and qS_2 components the anisotropic shear waveforms are similar to the isotropic waveforms, whereas on the SV and SH components in the left column the anisotropic waveforms feature two arrivals.

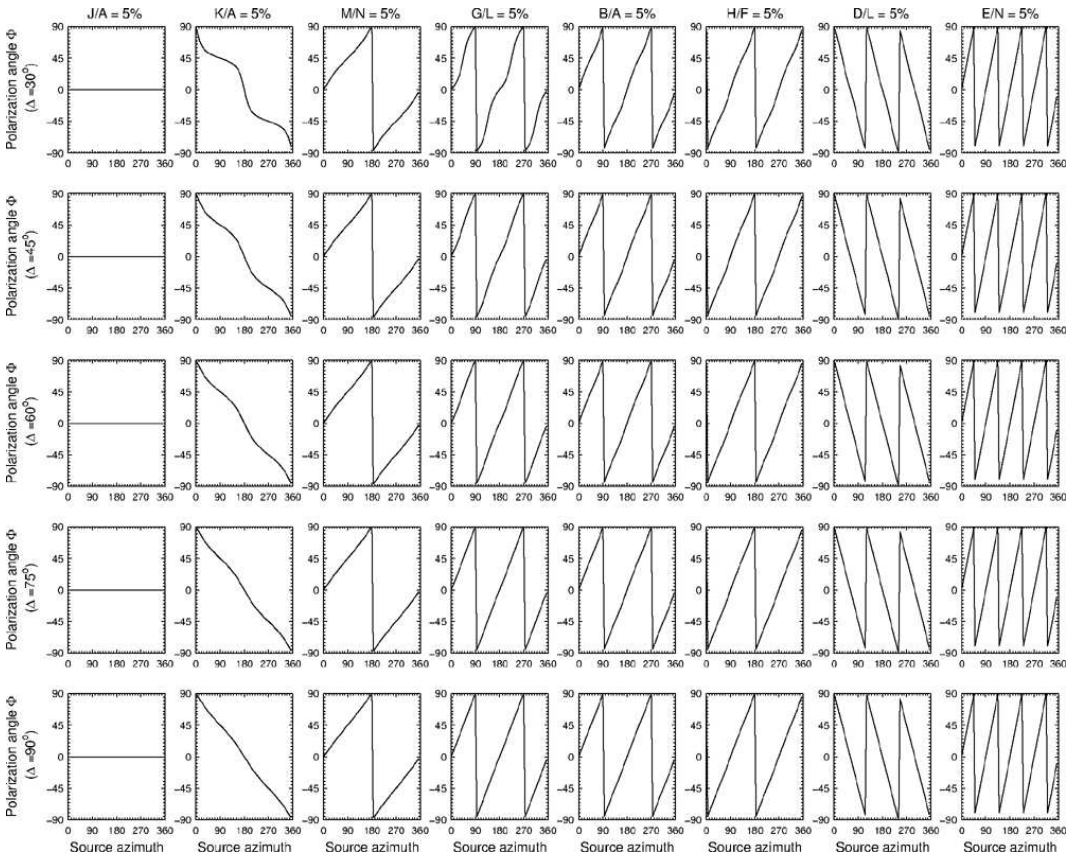

Figure 2.6: Polarization angle Φ determined by (2.35) in the top anisotropic layer as a function of source azimuth for the equidistant rings of stations at epicentral distances (represented by each row) of 30°, 45°, 60°, 75°, and 90°, respectively. Each column represents one of the eight elastic parameter pairs prescribed by (2.42)–(2.49). This polarization angle is used to define the qS_1 and qS_2 polarization directions (2.23), which are used to make the cross-correlation traveltime anomalies shown in Figure 2.7. See Figure 2.2 for the experimental set up.

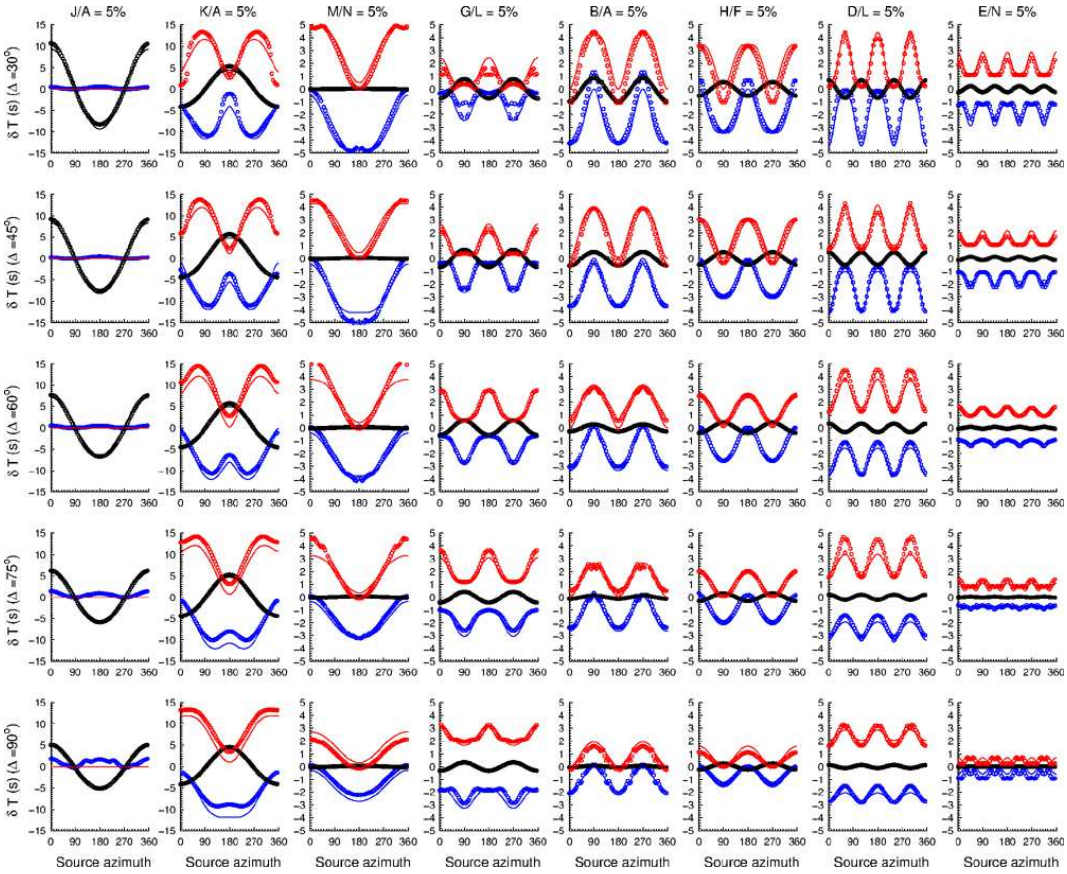

Figure 2.7: Body-wave cross-correlation traveltime anomalies (δT) as a function of source azimuth for global anisotropic models at epicentral distances (represented by each row) of $30°$, $45°$, $60°$, $75°$, and $90°$, respectively. The experimental setup is illustrated in Figure 2.2. The solid lines denote theoretical predictions of the traveltime anomalies calculated based upon (2.27), (2.33), and (2.40). The symbols denote measurements of the actual traveltime anomalies determined from the global spectral-element synthetics based upon cross-correlation. Black lines or symbols indicate P-wave theoretical predictions and SEM measurements, blue indicate qS_1 predictions and measurements, and red indicate qS_2 predictions and measurements. Note that the predictions and measurements for the eight elastic parameter pairs shown in subsequent columns ($J_{c,s}$, $K_{c,s}$, $M_{c,s}$, $B_{c,s}$, $G_{c,s}$, $H_{c,s}$, $D_{c,s}$, and $E_{c,s}$) nicely follow the expected variation with source azimuth Ψ prescribed by (2.42)–(2.49). The synthetics have been rotated onto the qS_1 and qS_2 polarization directions based upon a calculation of the polarization angle Φ defined by (2.35) for the top anisotropic layer (depth = 24.4 km), i.e., the last anisotropic region traversed by the ray (see Figure 2.6).

upon the local anisotropy, i.e., there is no memory along the ray. The variation in the shear-wave polarization angle Φ with source azimuth in Figure 2.6 reflects the degree one, two, three, or four parameterization of the elastic parameters prescribed by (2.42)–(2.49), and the associated traveltime anomalies shown in Figure 2.7 reflect this same pattern. Notice in Figure 2.7 that for the $G_{c,s}$ parameter pair at an epicentral distance of 30°, the fits between the SEM measurements and the theoretical predictions deteriorate around $\Psi = 0^\circ$, 90°, 180°, and 270°, but the fits at the same stations are good for other parameters, e.g., the $B_{c,s}$ pair. As shown in Figure 2.8, this difference can be attributed to the more dramatic along-ray variations of the shear-wave polarization angle Φ for the $G_{c,s}$ parameters than for the $B_{c,s}$ parameters. We assumed that the shear-wave polarization angle depends solely on the local anisotropy, but this assumption holds only when the local angle between the ray and the fast axis varies slowly along the raypath [e.g., ***Rümpker and Silver***, 1998]. Figure 2.8 shows that for the $B_{c,s}$ parameters the shear-wave polarization angle varies by less than 6° along the receiver-side raypath. However, for the $G_{c,s}$ parameters the shear-wave polarization angle varies by as much as 16°. This rapid variation of the shear-wave polarization angle Φ may cause a breakdown of our weakly anisotropic theory. Figure 2.9 shows an example of the predicted fast shear-wave polarization directions projected on the Earth's surface for the degree-three $D_{c,s}$ parameters defined by (2.48). For a given source azimuth, the angle between each ray plane/meridian and the fast polarization direction for the top layer is constant at all epicentral distances, but, depending on the incidence angle, the level of anisotropy may vary slowly along each raypath. The conventional definition of seismic anisotropy is a percent anisotropy which reflects the phase-speed difference between qS_1 and qS_2 waves [***Savage***, 1999]. Figure 2.10 shows the phase-speed anomaly ($\delta c/c$) in the upper mantle for P, qS_1, and qS_2 waves for a source azimuth of 0°, i.e., along the prime meridian, for equidistant rings of stations at epicentral distances of 30°, 45°, 60°, 75°, and 90°, respectively. The P-wave phase-speed anomaly is calculated based upon (2.27) and the S-wave phase-speed anomalies are calculated based upon (2.33). For P waves we see $\pm 10\%$ phase-speed anomalies associated with the $J_{c,s}$ pair and $\pm 5\%$ anomalies associated with the $K_{c,s}$ pair, but most other parameters produce phase-speed anomalies smaller than $\pm 2\%$. For S waves we see no phase-speed perturbations associated with the $J_{c,s}$ pair,

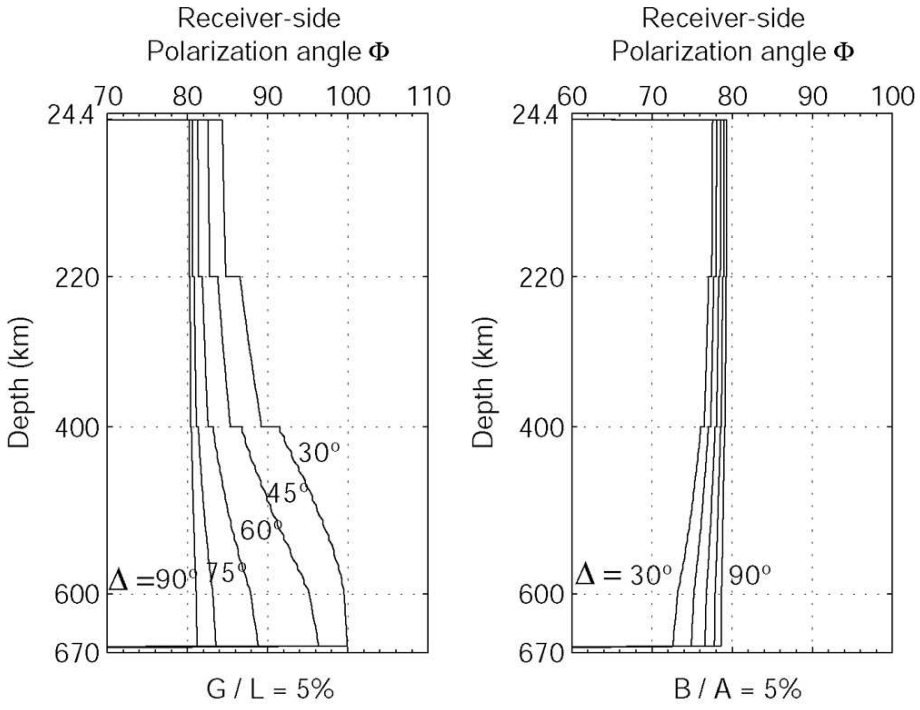

Figure 2.8: Variation of the polarization angle Φ defined by (2.35) with depth for a source azimuth Ψ of 80° for stations at epicentral distances of 30°, 45°, 60°, 75°, and 90°, respectively. Left: $G/L = 5\%$. Right: $B/A = 5\%$. As dictated by the asymptotic theory discussed in Section 2.3.2, the polarization angle at the top of the anisotropic layer (i.e., at a depth of 24.4 km as shown in Figure 2.6) is used to determine the shear-wave polarization directions (2.23) which are used to make the cross-correlation traveltime anomalies shown in Figure 2.7.

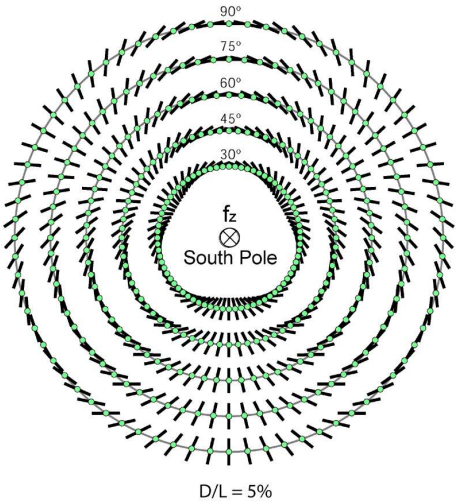

Figure 2.9: Bird's-eye view of the fast shear-wave (qS_1) polarizations in the top anisotropic layer for the $D_{c,s}$ parameter pair. The variation of the polarization angle Φ defined by (2.35) with source azimuth Ψ for the $D_{c,s}$ parameter pair is shown in the seventh column of Figure 2.6 for epicentral distances of $30°$, $45°$, $60°$, $75°$, and $90°$. The polarization directions are indicated by the black dashes, which are projected onto the unit sphere. Note that along each equidistant ring the fast axis projected onto the unit sphere exhibits the degree-three dependence with source azimuth prescribed by (2.48). The stations are marked by green dots. The source is a vertical force (f_z) located at South Pole at a depth of 600 km.

$\pm 5-8\%$ perturbations for $K_{c,s}$, $\pm 2-3\%$ perturbations for $M_{c,s}$, $G_{c,s}$, and $D_{c,s}$, and $\pm 1-2\%$ perturbations for $B_{c,s}$, $H_{c,s}$, and $E_{c,s}$.

In Figure 2.11 we show a comparison between the SV-component isotropic reference seismogram and a corresponding anisotropic seismogram for the $J_{c,s}$ perturbations given by (2.42). The $J_{c,s}$ pair has a dramatic effect on compressional waves, e.g., P, PcP, pP, and sP, but no effect on the direct S wave. This example illustrates how multiple observations may help constrain intrinsic anisotropy.

We would like to emphasize the fact the SEM implementation is based upon a Cartesian coordinate system in which the z-axis coincides with the rotation axis [*Komatitsch and Tromp*, 2002a,b]. Therefore, 'turning on' two of the parameters listed in Table 2.1 brings into play all the elements of the Cartesian representation of the elastic tensor used in the SEM software. Thus the numerical experiments presented here represent a very broad, challenging test of the SEM, and the software may thus be used with confidence to investigate general anisotropic models of the Earth's mantle.

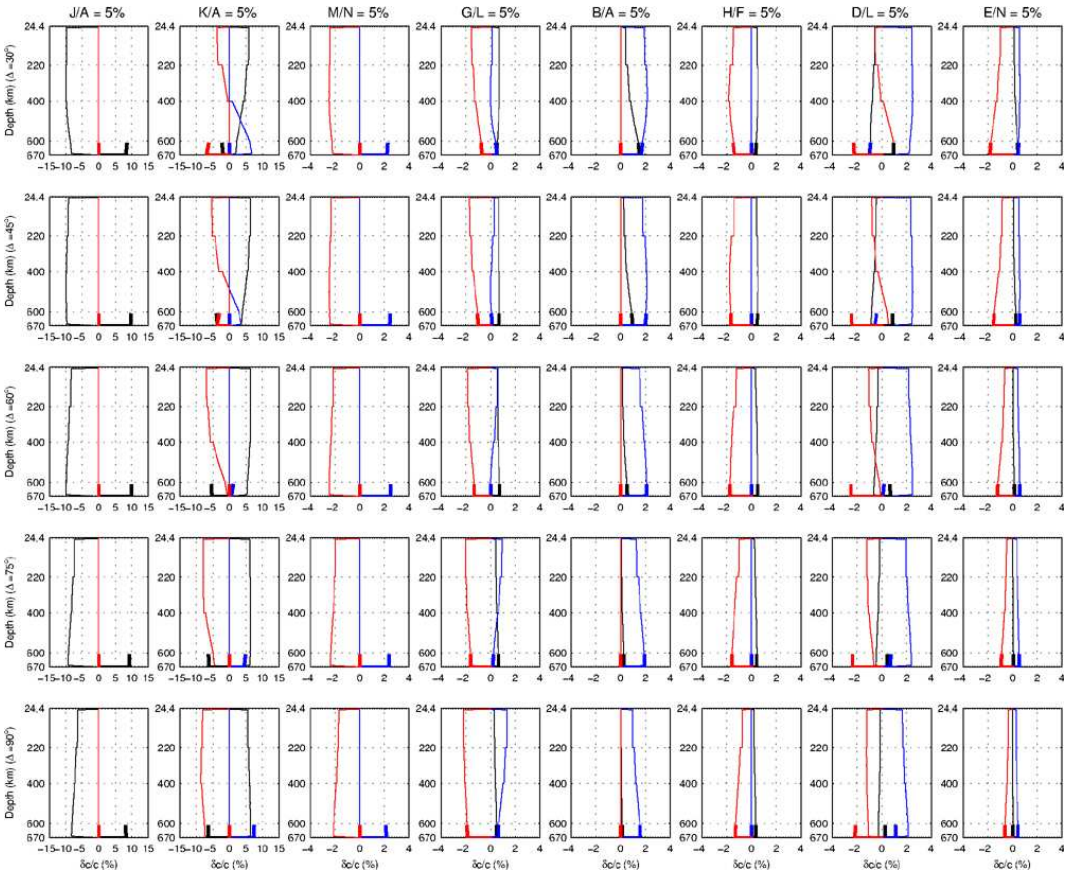

Figure 2.10: Phase-speed anomaly ($\delta c/c$) in the upper mantle for P, qS_1, and qS_2 waves for a source azimuth of 0° (i.e., along the prime meridian) for equidistant rings of stations at epicentral distances (represented by each row) of 30°, 45°, 60°, 75°, and 90°, respectively. The P-wave phase-speed anomaly is calculated based upon (2.27) and the S-wave phase-speed anomalies are calculated based upon (2.33). The P waves are represented by black lines, qS_1 waves are indicated by blue lines, and qS_2 waves are indicated by red lines. The thick lines with the same colors in the bottom represent the phase-speed anomaly $\delta c/c$ along the ray on the source side, i.e., between the hypocenter at 600 km and the bottom of the PREM upper mantle at 670 km. Each of the eight columns represents one of the eight elastic parameter pairs prescribed by (2.42)–(2.49).

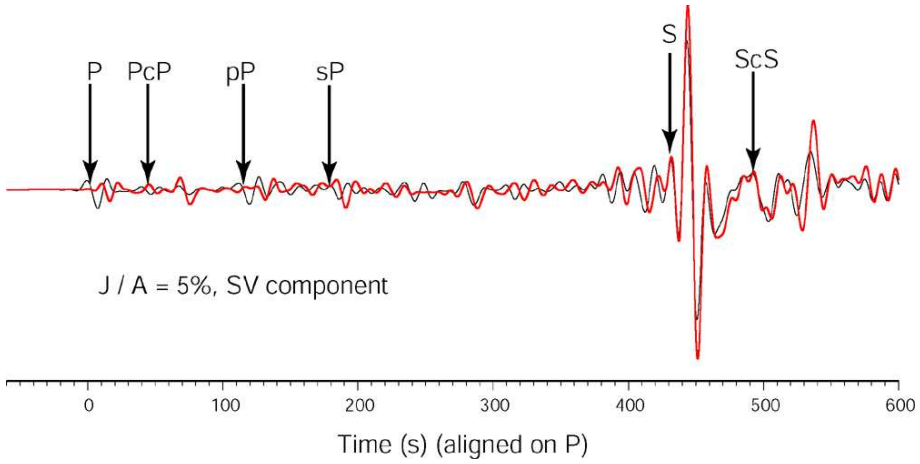

Figure 2.11: SV-component synthetic seismograms for PREM (black line) and an anisotropic model determined by (2.42) with $J/A = 5\%$ throughout the entire upper mantle (red line). The station is located at a source azimuth of 0° (i.e., along the prime meridian) at an epicentral distance of 60°. Both seismograms are aligned on the P arrival predicted by IASP91 [*Kennett and Engdahl*, 1991], and the IASP91 arrivals times of P, PcP, pP, sP, S, and ScS are indicated by the arrows. Note that the P wave is severely affected by the anisotropy but that the S wave is not, in agreement with our expectations based upon the phase-speed anomalies shown in the third row and first column of Figure 2.10 (J/A at a distance of 60°).

2.4.2 Regional Simulations

The global experiments in the previous section test the asymptotic theory for a local ray azimuth ζ equal to π and a variable incidence angle i along the unperturbed ray (Figures 2.1a and 2.2). As illustrated in Figure 2.12, in this section we will consider regional seismic wave propagation during which the incidence angle i of the unperturbed reference ray is constant but the ray azimuth ζ is variable. In order to avoid P-to-SV conversions and the generation of a Rayleigh wave at the free surface, which complicates phase identification and cross-correlation, the source is located at a depth of 40 km and the wavefield is recorded by an equidistant ring of receivers which is buried at a depth of 10 km. This source-receiver geometry results in a constant incidence angle $i = 71.6^\circ$ (the raypath in the isotropic reference model is a straight line) and a ray azimuth ζ that is equal to the source azimuth Ψ (which is measured counter-clockwise from due South).

As a reference model we use an isotropic, homogeneous half space with a density of 3 g/cm^3, a compressional-wave speed of 7.8 km/s, and a shear-wave speed of 4.5 km/s.

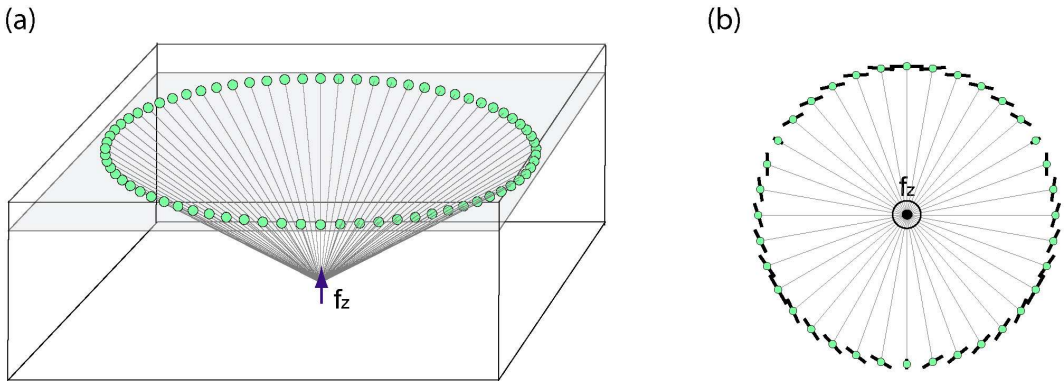

Figure 2.12: (a) Regional experimental setup. The model dimensions are 516 km (EW) $\times$ 507 km (NS) $\times$ 60 km (depth). The source is a vertical force (f_z) located at a depth of 40 km (indicated by the arrow). The green circles denote a ring of stations at an epicentral distance of 90 km and a depth of 10 km. The reference model is isotropic, with a density of 3 g/cm^3, a compressional-wave speed of 7.8 km/s, and a shear-wave speed of 4.5 km/s, upon which we superimpose constant 5% (J_c/A, K_c/A, M_c/A, D_c/L and B_c/A) or 10% (G_c/L, H_c/F, and E_c/N) anisotropy throughout the model. (b) Top view of the regional experimental setup. The black dash at each receiver indicates the horizontal projection of the fast shear-wave polarization direction (qS$_1$) for a 5% degree-three D_c/L perturbation.

The source is a vertical point force with a Ricker wavelet source-time function with a half-duration of 0.25 s. Synthetic seismograms for the isotropic reference model and the anisotropic models are calculated based upon a regional version of the SEM [*Komatitsch and Tromp*, 1999; *Komatitsch et al.*, 2004]. The regional spectral-element synthetics for this model are accurate at periods of 0.6 s and longer. These calculations take approximately 8 hours on 576 processors for 27 s long seismograms.

This experimental setup up enables us to 'turn on' one of the 1ζ, 2ζ, 3ζ, or 4ζ anisotropic perturbations listed in Table 2.1 to obtain non-degenerate shear waves with polarizations different from the reference SH and SV polarizations. We will only investigate the cosine parameters J_c, K_c, M_c, G_c, B_c, H_c, D_c, and E_c since the complementary sine parameters simply induce a $\pi/2$ phase shift. For the experimental setup shown in Figure 2.12a, the fast polarization direction of the shear wave varies predictably as a degree one, two, three, or four Fourier series with source azimuth. For example, it exhibits $2\pi/3$-periodicity if the 3ζ parameter D_c is uniformly perturbed by 5%, as illustrated in Figure 2.12b.

In Figure 2.13 we compare theoretical P, qS$_1$, and qS$_2$ body-wave traveltime anoma-

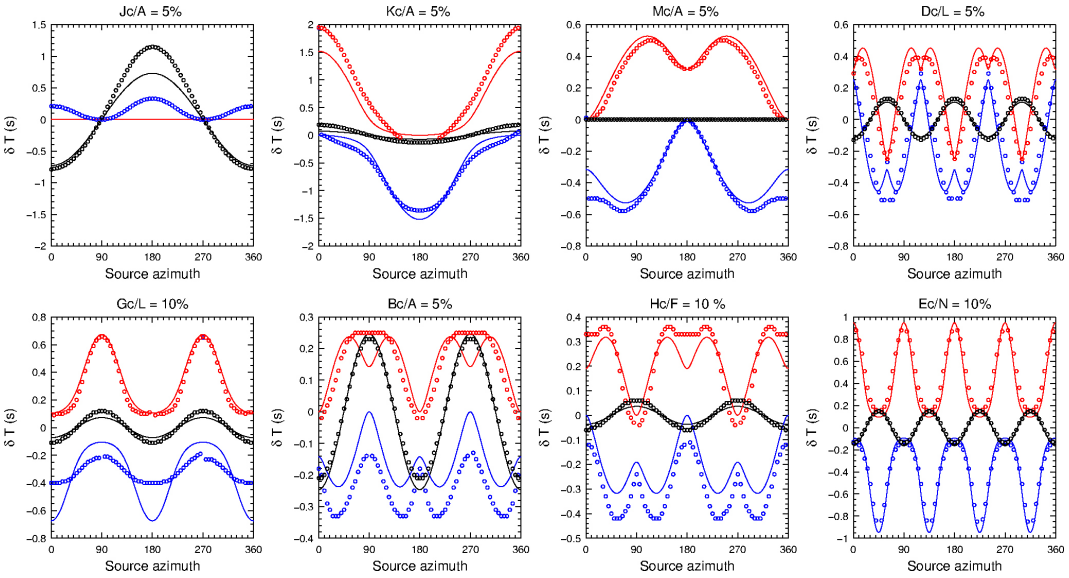

Figure 2.13: Body-wave traveltime anomalies due to uniform perturbations in the 1ζ anisotropic parameters J_c (5%), K_c (5%), and M_c (5%); the 2ζ anisotropic parameters G_c (10%), B_c (5%), and H_c (10%); the 3ζ anisotropic parameter D_c (5%); or the 4ζ anisotropic parameter E_c (10%). The solid lines (black: P; red: qS_1; blue: qS_2) denote theoretical predictions of the traveltime anomaly calculated based upon (2.27) or (2.33) and (2.40). The symbols (black: P; red: qS_1; blue: qS_2) denote measurements of the actual traveltime anomalies determined from the regional spectral-element synthetics based upon cross-correlation. See Figure 2.12 for the geometry of the experiment, Table 2.1 for the expected local azimuthal behavior, and Appendix A.1 for the relationship between these coefficients and the elements of the elastic tensor.

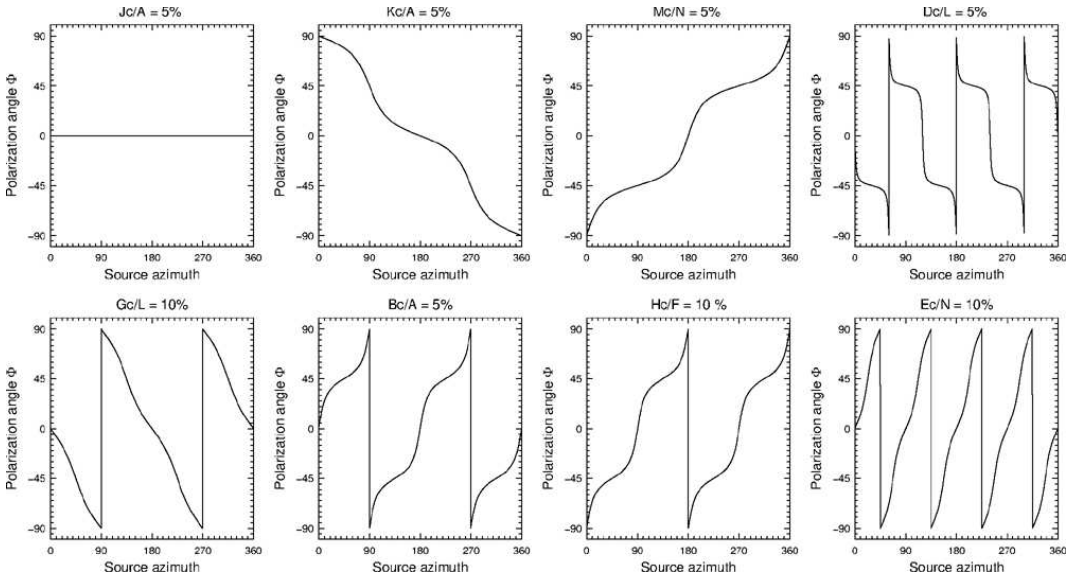

Figure 2.14: Variation of the polarization angle Φ defined in (2.35) as a function of source azimuth due to uniform perturbations in the 1ζ anisotropic parameters J_c (5%), K_c (5%), and M_c (5%); the 2ζ anisotropic parameters G_c (10%), B_c (5%), and H_c (10%); the 3ζ anisotropic parameter D_c (5%); or the 4ζ anisotropic parameter E_c (10%). Note that in the regional experiments (Figure 2.12) the source azimuth coincides with the ray azimuth (ζ) (Figure 2.1).

lies calculated based upon (2.27), (2.33), and (2.40) with SEM cross-correlation estimates. Once again, there is overall good agreement between the theoretical predictions and the SEM cross-correlation measurements, both of which show π-periodicity ($J_c/A = 5\%$, $K_c/A = 5\%$, or $M_c/A = 5\%$), $\pi/2$-periodicity ($G_c/L = 10\%$, $B_c/A = 5\%$, or $H_c/F = 10\%$), $\pi/3$-periodicity ($D_c/L = 5\%$) and $\pi/4$-periodicity ($E_c/N = 10\%$) for various anisotropic models. Prior to cross-correlation, both the isotropic and anisotropic synthetics are rotated onto the polarization directions of the P, qS_1, and qS_2 waves (see Figure 2.1). The polarization angles Φ predicted by (2.35) used for the rotations are shown in Figure 2.14 for each anisotropic model. Again these exhibit 2π-periodicity ($J_c/A = 5\%$, $K_c/A = 5\%$, or $M_c/A = 5\%$), π-periodicity ($G_c/L = 10\%$, $B_c/A = 5\%$, or $H_c/F = 10\%$), $2\pi/3$-periodicity ($D_c/L = 5\%$), and $\pi/2$-periodicity ($E_c/N = 10\%$) for different anisotropic models.

There are some notable small discrepancies between the theoretical predictions and the SEM cross-correlation measurements shown in Figure 2.13. Based upon Table 2.1, for

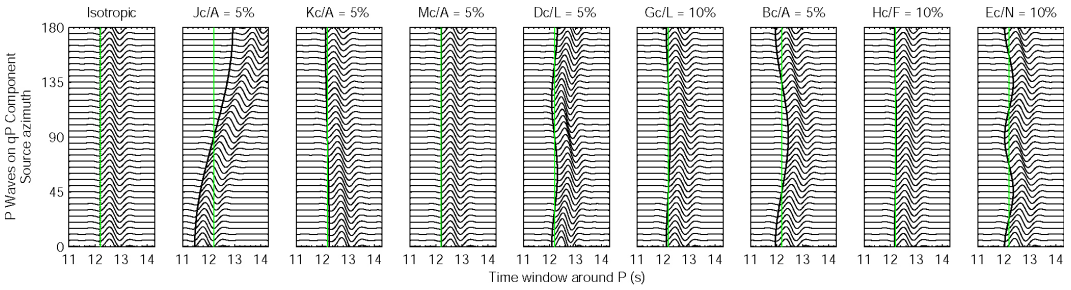

Figure 2.15: Azimuthal profiles (i.e., waveforms plotted as a function of source azimuth) for regional synthetic P waveforms for the isotropic reference model; the 1ζ anisotropic parameters J_c (5%), K_c (5%), and M_c (5%); the 2ζ anisotropic parameters G_c (10%), B_c (5%), and H_c (10%); the 3ζ anisotropic parameter D_c (5%); and the 4ζ anisotropic parameter E_c (10%). Green lines indicate the P-wave arrival time in the homogeneous isotropic reference model. Black lines indicate the theoretical prediction of the P-wave arrival time for each anisotropic model. The waveforms have been rotated onto the P-wave polarization direction $\hat{\mathbf{g}}_3$ (see Figure 2.1). The experimental setup is illustrated in Figure 2.12.

the J_c anisotropic parameter we expect a 1ζ directional dependence for P waves but not for S waves. However, the SEM cross-correlation measurements exhibit a weak directional dependence for the fast S wave, and the P-wave traveltime anomalies at a source azimuth in the vicinity of 180° are larger than predicted. There are also discrepancies for the fast shear waves (qS_1) for the G_c, B_c, and H_c parameters. Despite relatively large perturbations in the anisotropic parameters, the differential traveltime anomalies are frequently just a fraction of a second, which makes the cross-correlation measurements challenging. The theory is probably more accurate for the global simulations than for the regional simulations, because the global wavefronts have traveled long distances and are therefore more planar than the regional waves. Because of this, the distinction between group and phase speeds becomes more important at the regional scale.

The theoretical traveltime predictions for our anisotropic models are relatively simple and straightforward to implement, but the anisotropic effects on waveforms are much more difficult to account for. For P waves the waveforms in the perturbed anisotropic model are very similar to the isotropic reference waveforms (Figure 2.15). For the three-component S waves the waveforms change dramatically in the anisotropic models (Figure 2.16). The fast and slow shear waves are coupled on all three components, and when the coupling is severe

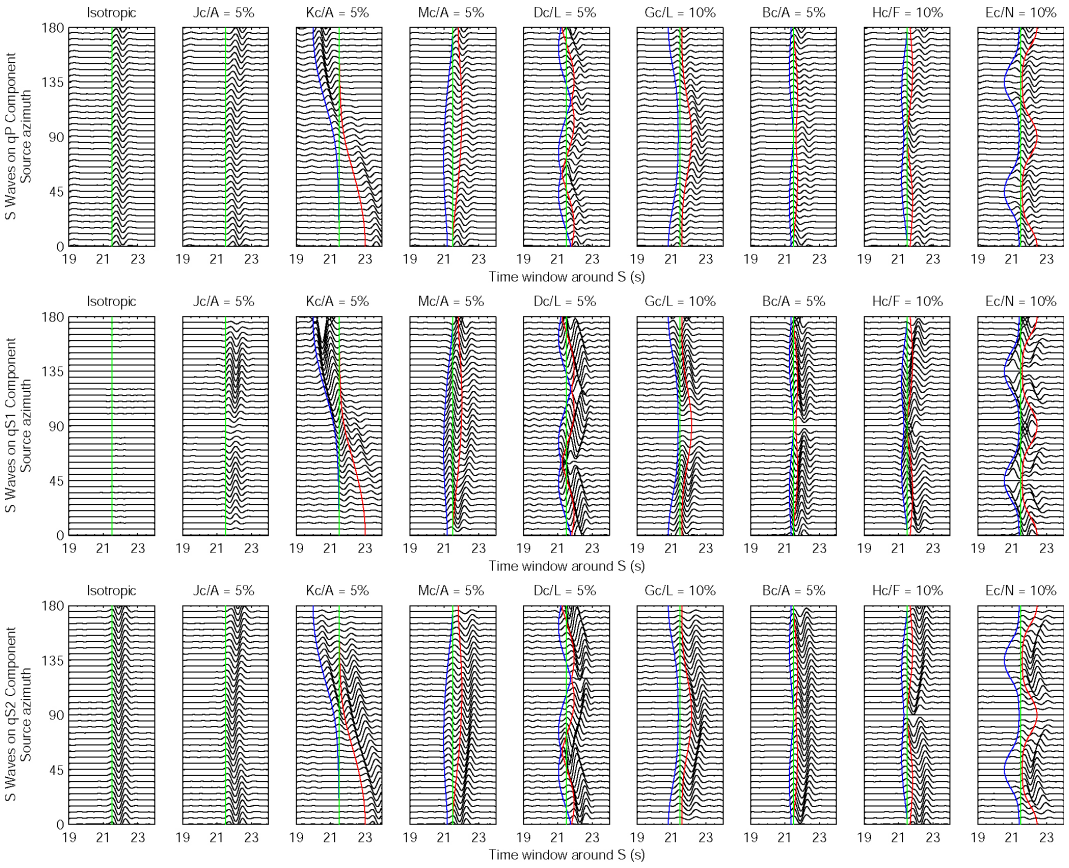

Figure 2.16: Azimuthal profiles (i.e., waveforms plotted as a function of source azimuth) for regional synthetic S waveforms for the isotropic reference model; the 1ζ anisotropic parameters J_c (5%), K_c (5%), and M_c (5%); the 2ζ anisotropic parameters G_c (10%), B_c (5%), and H_c (10%); the 3ζ anisotropic parameter D_c (5%); and the 4ζ anisotropic parameter E_c (10%). Green lines indicate the S-wave arrival time in the isotropic reference model. Blue lines (red lines) indicate the theoretical prediction of qS_1-wave (qS_2-wave) arrival times for each anisotropic model. The waveforms are rotated onto the perturbed polarization directions ($\hat{\mathbf{g}}_1$, $\hat{\mathbf{g}}_2$, and $\hat{\mathbf{g}}_3$) (Figure 2.1). The isotropic waveforms are projected to the unperturbed polarization directions ($\hat{\mathbf{e}}_1$, $\hat{\mathbf{e}}_2$, and $\hat{\mathbf{e}}_3$). Top row: qP component. Middle row: qS_1 component. Bottom row: qS_2 component. The isotropic SH wave (second row, first column) has zero amplitude because the vertical point force does not excite it. The experimental setup is illustrated in Figure 2.12.

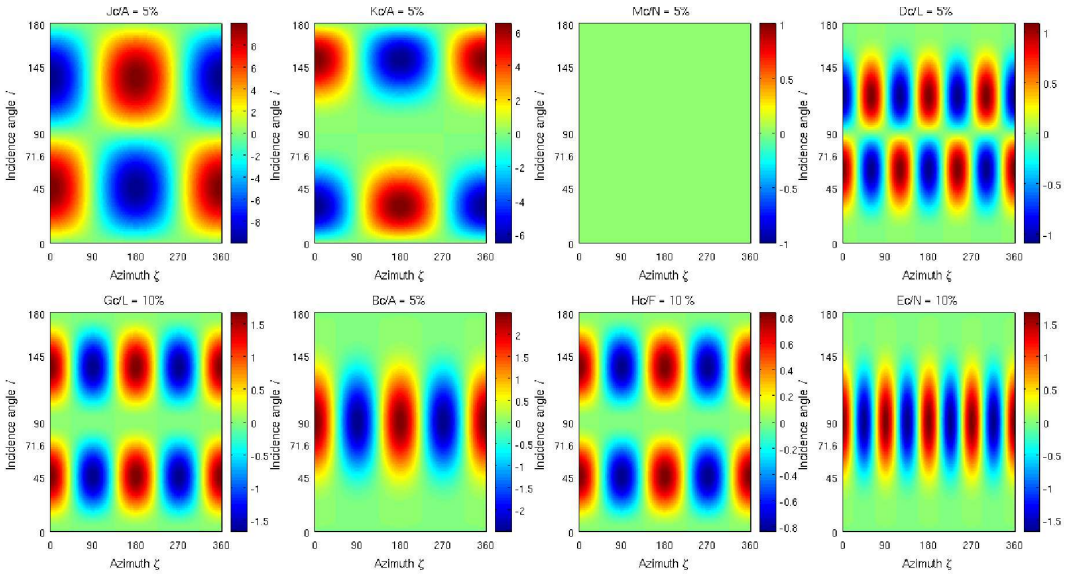

Figure 2.17: Directional dependence of the P-wave phase-speed anomaly $\delta c_3/c_3$ defined by (2.27) as a function of ray azimuth ζ and incidence angle i. Colors indicate percentage phase-speed perturbations for each anisotropic model, i.e., the 1ζ parameters J_c (5%), K_c (5%), and M_c (5%); the 2ζ parameters G_c (10%), B_c (5%), and H_c (10%); the 3ζ parameter D_c (5%); and the 4ζ parameter E_c (10%).

the waveforms exhibit obvious broadening or even double-pulse characteristics associated with wavefront folding, e.g., for the M_c parameter on all three components, and for the K_c parameter on the qS_1 and qS_2 components. The S waveform on the qS_1 component usually contains both fast and slow shear waves, with most of the energy concentrated in the first arrival, and the S waveform on the qS_2 component usually contains a clean late arrival with very small precursors. This could explain why we generally obtain slightly better agreement between the asymptotic theory and SEM cross-correlation traveltimes for the slow qS_2 waves.

The raypaths considered in the regional simulations cover only a very small subset of all possible slowness directions in the anisotropic models. Figure 2.17 illustrates the complete directional dependence of the anisotropic P-wave phase-speed anomaly (2.27) for all anisotropic cosine parameters. Note that the phase-speed is anti-symmetric with respect to $i = 90^\circ$ for parameters with an odd dependence on the ray azimuth ζ, but symmetric for parameters with an even dependence on ζ, in accordance with the symmetry (2.39). The P-wave phase-speed anomaly is as large as $\pm 10\%$ for the J_c parameter and $\pm 6\%$ for the K_c

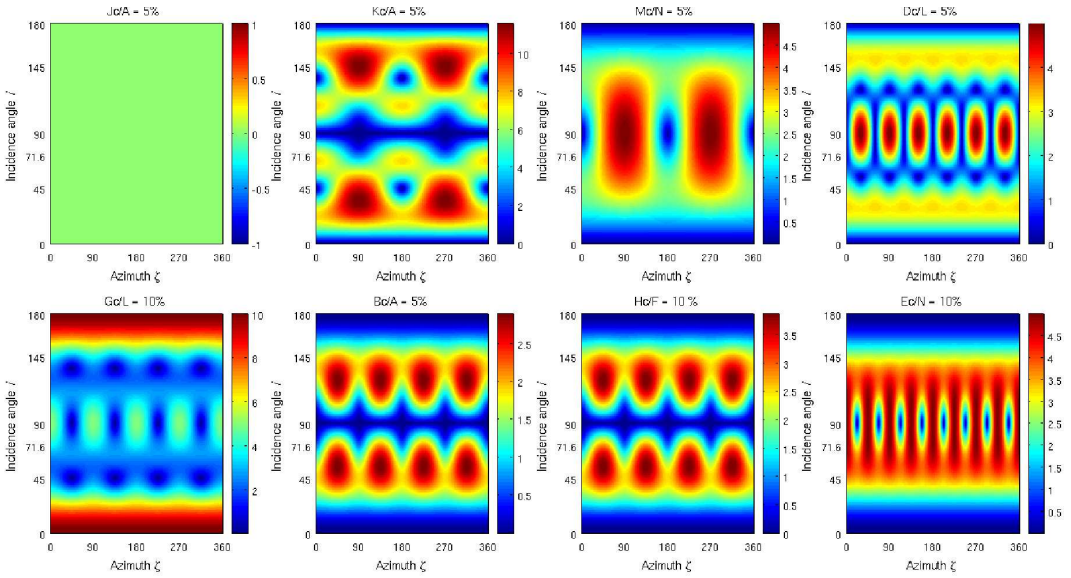

Figure 2.18: Directional dependence of the S-wave differential phase-speed anomaly $(\delta c_1 - \delta c_2)/c_1$ defined by (2.33) as a function of ray azimuth ζ and incidence angle i. Colors indicate percentage differential phase-speed perturbations for each anisotropic model, i.e., the 1ζ parameters J_c (5%), K_c (5%), and M_c (5%); the 2ζ parameters G_c (10%), B_c (5%), and H_c (10%); the 3ζ parameter D_c (5%); and the 4ζ parameter E_c (10%).

parameter, but for most other parameters the phase-speed perturbation is less than $\pm 2\%$. The P-wave is insensitive to the degree-one M_c parameter.

The directional dependence of the anisotropic S-wave differential phase-speed anomaly is illustrated in Figure 2.18 based upon (2.33) for all anisotropic cosine parameters. Note that the differential phase-speed between qS_1 and qS_2 exhibits the symmetry (2.39) for all anisotropic parameters. S waves are insensitive to the degree-one parameter J_c but exhibit 0–12% perturbations for K_c, 0–10% perturbations for G_c, 0–5% perturbations for M_c, D_c and E_c, 0–4% perturbations for H_c, and 0–3% for B_c.

2.5 Conclusions

Based upon the well-known azimuthal dependence of surface-wave phase speeds in weakly anisotropic media and a complementary result derived in this paper for the directional dependence of body-wave phase speeds, we have demonstrated that theoretical predictions of surface-wave phase and body-wave traveltime anomalies are generally in good agreement

with numerical simulations for anisotropy at the 5% level. To accommodate this comparison, we have extended global and regional spectral-element simulations to incorporate fully 3-D anisotropic media. For P, qS_1, and qS_2 body waves as well as quasi-Love and quasi-Rayleigh surface waves we have tabulated which combination of the 21 independent elastic parameters affects their respective phase speeds (Table 2.1).

A transversely isotropic medium is determined by the five elastic parameters A, C, L, N, and F [*Love*, 1911; *Dziewonski and Anderson*, 1981]. *Montagner and Nataf* [1986] demonstrated that surface-wave propagation in a general anisotropic Earth model is controlled by an additional eight elastic parameters: the six 2ζ parameters G_c, G_s, B_c, B_s, H_c, and H_s, and the two 4ζ parameters E_c and E_s, where ζ denotes the local surface-wave ray azimuth. In theory, as summarized in Table 2.1, the dispersion of Love waves involves only six anisotropic parameters (the 0ζ parameters L and N, the 2ζ parameters G_c and G_s, and the 4ζ parameters E_c and E_s), whereas Rayleigh-wave dispersion involves thirteen anisotropic parameters (the 0ζ parameters A, C, L, N, and F; the 2ζ parameters G_c, G_s, B_c, B_s, H_c, and H_s; and the 4ζ parameters E_c and E_s). In this paper we demonstrated that body-wave propagation in a weakly anisotropic Earth model involves an additional eight parameters: the six 1ζ parameters J_c, J_s, K_c, K_s, M_c, and M_s, and the two 3ζ parameters D_c and D_s, for a combined total of all 21 elastic parameters. In theory, compressional waves are sensitive to all but three of these anisotropic parameters (there is no sensitivity to the 0ζ parameter N and the 1ζ parameters M_c and M_s), and shear waves are sensitive to all but two anisotropic parameters (there is no sensitivity to the 1ζ parameters J_c and J_s). The theoretical and numerical results presented in this paper provide new insight into the connection between seismic waveforms and anisotropy, insight that should guide future tomographic inversions for anisotropic heterogeneity.

Our spectral-element packages are freely available for academic, non-commercial research from `www.geodynamics.org/cig/software/packages/seismo`.

Chapter 3

Waveform Modeling Of The Slab Beneath Japan

3.1 Abstract

The tomographic P-wave model for the Japan subduction zone derived by *Zhao et al.* [1994] has two very striking features: a slab about 90 km thick with P-wave velocities 3–6% higher than the surrounding mantle, and a mantle wedge with -6% low-velocity anomalies. We study 3-component seismograms from more than 600 Hi-net stations produced by two earthquakes which occurred in the down-going Pacific Plate at depths greater than 400 km. We simulate body-wave propagation in the 3-D P-wave model [*Zhao et al.*, 1994] using 2-D finite-difference (FDM) and 3-D spectral-element (SEM) methods. As measured by cross-correlation between synthetics and data, the P-wave model typically explains about half of the traveltime anomaly and some of the waveform complexity, but fails to predict the extended SH wavetrain. In this study we take advantage of the densely distributed Hi-net stations and use 2-D FDM modeling to simulate the P-SV and SH waveforms. Our 2-D model suggests a thin, elongated, low-velocity zone exists atop the slab, extending down to a depth of 300 km with an S-wave velocity reduction of 14% if a thickness of 20 km is assumed. Further 3-D SEM simulations confirm that this model explains a strong secondary arrival which cannot easily be imaged with standard tomographic techniques. The low-velocity layer could explain the relatively weak coupling associated with most subduction zones at shallow depths ($<$ 50 km), generally involving abundant volcanic activity and

silent earthquakes, and it may also help to further our understanding of the water-related phase transition of ultra-mafic rocks, and the nature of seismicity at intermediate depths ($\sim$ 70–300 km).

3.2 Introduction

Subduction zones represent some of the most heterogeneous regions in Earth's upper mantle in terms of seismic velocities. A great deal of tectonic activity, such as earthquakes, silent slip events, and volcanic eruptions, occurs in subduction zones due to dehydration of the slab and the associated melting inside the mantle wedge.

Detailed 3-D tomographic P-wave studies of the Japanese subduction zone have been conducted on both regional and global scales by *Zhao and Hasegawa* [1993], *Zhao et al.* [1994], and *Zhao* [2001]. The tomographic models on both scales exhibit similar gross P-wave heterogeneity. The P-wave velocity is higher inside the slab and lower in the wedge compared to the ambient mantle (Figure 3.1). The imaged anomalies are well correlated with seismic and volcanic activities. However, the regional and global models also exhibit significant differences (Figure 3.1b): the regional model has a sharp P-velocity contrast across the top of the slab, while the contrast in the global model is weaker and smoother; the regional model has no high-velocity anomaly inside the transition zone due to a lack of depth resolution below 500 km, whereas the global model has a high-velocity slab-shaped anomaly inside the transition zone (410–660 km), which was resolved by traveltime data from teleseismic events. In order to better explain body-wave traveltimes and waveforms, it is necessary to incorporate the observed global features into the regional model, and to determine the correct amplitude of the P-velocity anomalies inside the slab and in the mantle wedge. There are a few inherent drawbacks of the regional model [*Zhao et al.*, 1994] in terms of explaining the data from local deep earthquakes. The Japan University Seismic Network (216 stations) was used in the inversion, but due to a lack of local earthquakes at depths greater than 500 km, the array aperture is insufficient to resolve seismic velocity structure below depths of $\sim$ 400 km. Furthermore, the starting model for the inversion by *Zhao et al.* [1994] contains a pre-constrained slab and the traveltimes of S-to-P and P-to-S

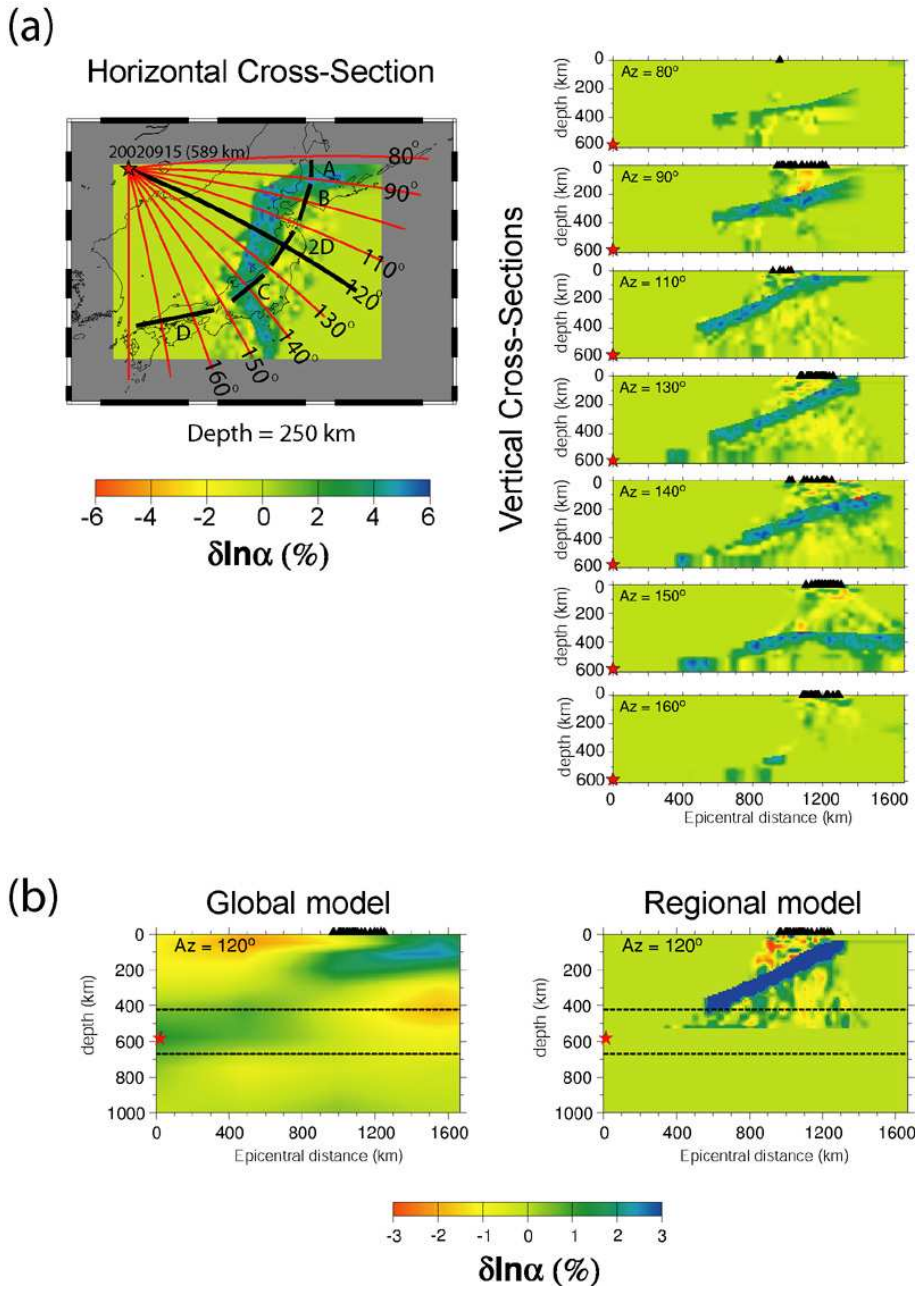

Figure 3.1: Cross-sections through the regional and global tomographic P-wave models derived by *Zhao et al.* [1994], and *Zhao* [2001]. Colors indicate P-wave velocity anomalies relative to 1-D reference Earth model IASPEI91 [*Kennett and Engdahl*, 1991]. The slab is delineated by the blue colors (positive anomalies). The red star indicates the location of event 20020915 (depth 589 km), and the stations along each profile are marked by black triangles. (a) The regional model [*Zhao et al.*, 1994]. The horizontal cross-section in the top left shows the P-wave anomalies at a depth of 250 km. The red lines roughly indicate the positions of the vertical cross-sections in the top right. A, B, 2D, C, and D label five corridors with distinct slab geometries. Corridor A (80–90°): flattened slab. Corridors B (90–110°) and C (130–150°): the bending edges of the slab. Corridor 2D (110–130°): steepened slab with almost constant slope. Corridor D ($>$ 160°): the non-slab region. (b) Comparison between the global and regional P-wave models. The two dashed lines indicate the 410 km and 670 km discontinuities, respectively. The cross-sections are both along the black line in the top left map with a source-station azimuth of 120°. Note that there is a positive (blue) anomaly inside the transition zone in the global model, but not in the regional model.

converted phases (at the upper boundary of the slab) were used to provide better constraints on the velocity contrast across the slab's upper surface. These converted phases, however, do not provide any constraint on a possible sharp negative velocity jump. Finally, waveform distortions caused by sharp structures are not included in the tomographic inversion. These waveform perturbations consist of multiple interfering arrivals, resulting in distorted and widened arrivals. These features are addressed in this article by modifying the regional model.

It has long been observed that sharp structures have profound effects on waveforms, and that such waveform complexity can be used as an independent constraint on slab structure. There have been a few attempts to use 2-D and 3-D forward modeling to investigate the effects of slab geometry and heterogeneity on waveforms [*Zhou and Chen*, 1995; *Vidale*, 1987; *Igel et al.*, 2002]. Some preliminary results based upon broadband sparse data coverage were obtained for slabs in other subduction zones, such as the slabs beneath North America [*Vidale and Garcia-Gonzalez*, 1988] and Kuril-Kamchatka [*Cormier*, 1989]. Recent works on guided waves in the subduction zone beneath Chile and Peru by *Martin et al.* [2003, 2005] include detailed investigations of a low-velocity layer on top of the slab. Furthermore, data from the Japanese K-NET and KiK-net strong-motion instruments and the FREESIA broadband station was used by *Furumura and Kennett* [2005] to investigate waveform dispersion caused by elongated scatterers in the slab beneath Japan. In general, the waveform dispersion recorded at broadband stations (0.25–18 Hz) is often explained in terms of a low velocity layer with a thickness less than 10 km and a P-wave velocity reduction of 7%, based upon Fourier spectral analysis and approximate P-wave waveform comparison between data and synthetics.

In this study, we take advantage of the dense and wide coverage of the Japanese Hi-net array, which is a high-sensitivity network consisting of 600 bore-hole 3-component, short-period (1 s) seismographs (Figure 3.2). Because the Hi-net instruments record only signals within a relatively narrow frequency band (0.1–2 Hz), waveform dispersion effects observed in this dataset are not as prominent as in previous studies [*Martin et al.*, 2003, 2005; *Furumura and Kennett*, 2005]. Our focus is on explaining strong secondary S arrivals. We use waveforms varying at the scale of tens of kilometers as additional constraints on slab

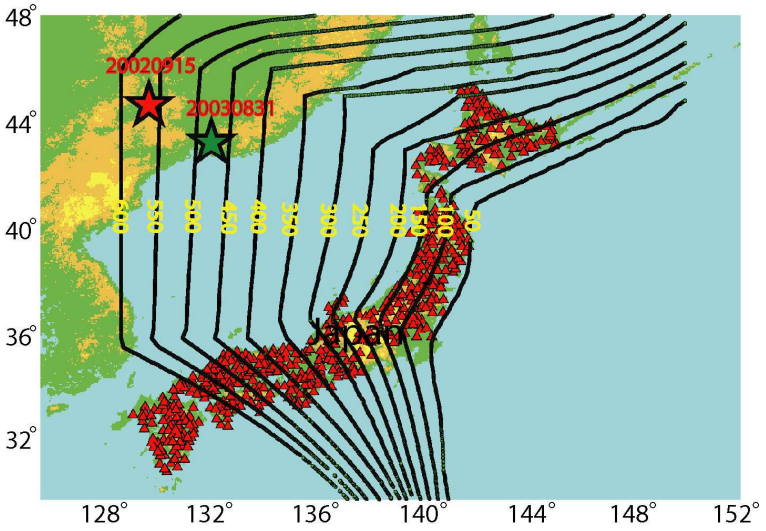

Figure 3.2: Map view of the study area: Hi-net stations are indicated by red triangles and contours of the upper boundary of the Pacific plate are indicated by black lines with a 50 km contour interval. The location of event 20020915 is marked by the red star and event 20030831 is indicated by the green star.

structure, and present waveform modeling results using the 2-D finite-difference method (FDM) by *Vidale et al.* [1985] and the 3-D spectral-element method (SEM) by *Komatitsch and Tromp* [2002a,b].

We begin with a brief review of the numerical methods and related grids used in this study. This is followed by an assessment of how well the tomographic models developed by Zhao predict the observed P and S waves both in terms of timing and waveforms for a simple deep source. The SH waveforms for one particular 2-D corridor are most suitable for further analysis of slab structure, a subject which is addressed at length in the remaining sections.

3.3 Numerical Simulations

In this section we introduce the grids used in the FDM and SEM simulations of seismic wave propagation in the regional and global P-wave models [*Zhao et al.*, 1994; *Zhao*, 2001]. The lateral domain for the regional model is 32–45°N and 130–145°E, with a depth extent from the surface to 500 km. The model properties outside this region are determined by the 1-D IASPEI91 model [*Kennett and Engdahl*, 1991]. 3-D S-wave models are obtained

from the P-velocity models using a scaling factor $f = \delta \ln \beta / \delta \ln \alpha = 1.5$–$2.5$, where β denotes the shear-wave velocity and α the compressional-wave velocity. $\delta \ln \alpha$ and $\delta \ln \beta$ refer to the fractional velocity perturbations with respect to 1-D IASPEI91 model. This range of scaling factors is representative of upper-mantle tomography. The purpose of the 2-D FDM and 3-D SEM simulations is to assess the quality of the regional and global models by comparing data and synthetics in terms of both traveltimes and waveforms.

3.3.1 FDM Simulations

The FDM simulations are carried out by simulating the P-SV and SH systems separately for each model. The 2-D models are 2-D slices which are obtained from the 3-D P model at source azimuths from 80° to 180° at 2° intervals. For each slice, the 2-D model domain is 1200 km deep and 1800 km wide. The grid size throughout the entire domain is 2 km $\times$ 2 km. To confirm that this grid has the appropriate resolution for the periods of interest, we did a few simulations at twice the resolution. For the periods of interest, this resulted in essentially the same synthetic seismograms. We placed the source 200 km from the left boundary and 600 km above the bottom boundary in order to avoid artificial reflections. The frequency contents of the FDM synthetics is 1 Hz and lower. The scheme for generating point-source seismograms for shear dislocations using 2-D numerical methods is discussed in *Helmberger and Vidale* [1988]. It is based on expanding the complete 3-D solution in asymptotic form and separating the motions into the SH and P-SV systems. This analytical Cagniard-de Hoop method is used to derive closed-form expressions appropriate for 2-D FDM source excitations. Synthetics generated by this method are benchmarked in the above mentioned study.

3.3.2 SEM Simulations

For the SEM simulations we use the implementation of *Komatitsch and Tromp* [2002a,b]. In our study we use only one of the six 'cubed-sphere' chunks that constitute the entire globe, with absorbing boundary conditions at the artificial edges of the domain. Compared to the full globe, this approach significantly reduces the memory and CPU requirements and

allows for a much denser mesh in the modeling region. On the 25 processors of a modern PC cluster (CITerra, 3.2 GHz Intel Xeon, http://aeolis.gps.caltech.edu/wiki/Public/Technology), this one chunk version SEM code can calculate synthetics accurate at periods of $\sim$ 6 s and longer in 3.5 hours for an 8.0 minutes record length. The model implementation and mesh configuration are shown in Figure 3.3; for clarity, only 2 of the 25 mesh slices are displayed. Elements in the upper mantle mesh have dimensions of 30 km $\times$ 30 km, which is twice as big as the elements in the crust. The doubling of element size with depth maintains a relatively similar number of grid points per wavelength. A polynomial degree 4 interpolation is used to capture the velocity variations within the spectral elements, and therefore the grid spacing is $\sim$ 7 km in the upper mantle and $\sim$ 3.5 km in the crust. We did a few SEM runs for a mesh with twice this resolution, i.e., a grid spacing of $\sim$ 3.5 km in the upper mantle and $\sim$ 1.75 km in the crust, and confirmed that at periods of $\sim$ 6 s and longer this mesh leads to the same synthetic seismograms as the coarser mesh, indicating that the coarser mesh accurately resolves the waves of interest.

3.4 Data Selection and Model Testing

Hi-net waveform data from two deep earthquakes with relatively simple sources were chosen for this study: event 20020915 (location: 44.77°N, 130.04°E, 589 km; fault plane 1: strike 204°, dip 85°, rake 72°; fault plane 2: strike 98°, dip 19°, rake 163°; $M_w = 6.4$) and event 20030831 (location: 43.38°N, 132.37°E, 492 km; fault plane 1: strike 77°, dip 45°, rake $-179°$; fault plane 2: strike 346°, dip 89°, rake $-45°$; $M_w = 6.1$) both are shown in Figure 3.2. The source locations and focal mechanisms are determined by the Harvard centroid-moment tensor (CMT) solutions. We use the deeper event with better coverage to develop the model, and validate this model by successfully predicting the waveforms for the other event.

We start by comparing the data with simulations based on the tomographic models developed by Zhao et al. and discussed earlier (Figure 3.1). In these initial simulations we grid the regional P-wave model [*Zhao et al.*, 1994] and experiment with 4 different S-wave models. Three S models are obtained by scaling the shear velocity β to the compressional

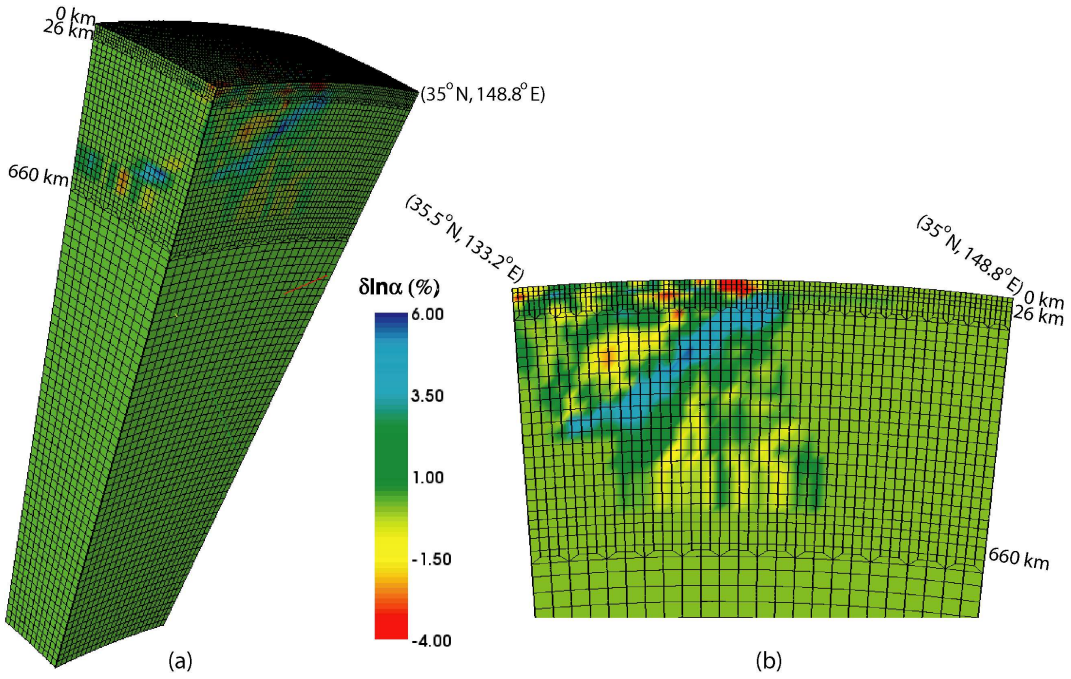

Figure 3.3: 3-D spectral-element mesh. P-wave velocity anomalies from the regional tomographic model [*Zhao et al.*, 1994] are superimposed on the mesh. For parallel computing purposes, the one-chunk SEM simulation is subdivided in terms of 25 slices. The center of the chunk is at (38.5°N, 137.5°E), and the lateral dimensions are $30^\circ \times 30^\circ$. (a) Full view of two neighboring slices. (b) Close-up view of the upper mantle mesh. Note that the element size in the crust (top layer) is 15 km $\times$ 15 km, and that the size of the spectral elements is doubled in the upper mantle. The velocity variation is captured by 5 grid points in each direction of the elements [*Komatitsch and Tromp*, 2002a,b].

velocity α based upon overall scaling factors $f = \delta \ln \beta / \delta \ln \alpha = 1.5$, 2.0, and 2.5, respectively. A fourth S model is obtained by using a scaling factor $f = 2.0$ for the slab but a scaling factor of zero for the mantle wedge (i.e., no negative β anomalies).

Data and synthetics for all available Hi-net stations are bandpass-filtered between 1 s and 29 s for the FDM simulations and between 6 s and 29 s for the SEM simulations. For each component at every station, data and synthetic seismograms are cross-correlated in time windows centered on the predicted P or S arrivals relative to the 1-D IASPEI91 model. Cross-correlations for P waves are conducted in a time window starting 10 s before and ending 20 s after the P arrival predicted by IASPEI91. For S waves, the time window is centered on the predicted IASPEI91 S arrival with a 30 s half-window width. The time windows are chosen to be just wide enough to include the direct P and S arrivals, whose peak amplitudes are essential in determining the final cross-correlation results.

3.4.1 P Waves

An example of P-wave data and 2-D FDM synthetics for the regional model is displayed in Figure 3.4. The source-time function is taken from stations at large azimuths (greater than 175°, Figure 3.1), where the slab is not sampled by the wavefield. These records are simple and similar to the observed P waves toward the bottom of the record sections shown in Figure 3.4. The more distant stations are closer to the slab (see Figure 3.1) and display complexity associated with the development of a secondary arrival. Some of this complexity is captured by the synthetics, but it is irregular due to the complicated low-velocity structure above the slab. The data and synthetics are cross-correlated and time-shifted for alignment. Over 500 pairs have been analyzed, with delays displayed in Figure 3.5a. Note that about half of the scatter for the 1-D model is reduced by the 3-D model. About 80% of the cross-correlation coefficients fall into the range of 0.6–0.9 (Figure 3.5b) and the overall waveform fits between the P-wave data and the synthetics calculated from the regional model [*Zhao et al.*, 1994] are quite good. However, there are strong azimuthal misfit variations when the data are partitioned into the corridors shown in Figure 3.1a. The synthetics in corridor D have higher waveform similarity compared to the data than those in corri-

dors A, B, 2D, and C, where the slab exists. In particular in corridors B and C, where the slab geometry changes rapidly with azimuth, the fits deteriorate. The smallest cross-correlation values reach 0.2, which includes a group of synthetic waveforms with a polarity different from the data. The synthetics with cross-correlation coefficients in the range of 0.8–0.9 have a relatively simple Gaussian pulse shape, like the data, which is the general shape of the waveforms that are not affected by the slab. Cross-correlation values in the range of 0.6–0.8 represent waveforms with widened or dispersed pulse shapes in both synthetics and data, which is the key waveform feature in this high-resolution regional model; this feature is even more obvious in SH-wave data, and will be addressed in detail in the following sections. In corridor D, the synthetics are on average 2.5 s slower than the data. Along this corridor there is no slab and the structure is almost 1-D, indicating either that the IASPEI91 model is too slow or the baseline shift is caused by uncertainty in the source location. In corridor 2D, where the updip-going wavefronts encounter the slab the most, the slab has the maximum effect on both traveltimes and waveforms. In this corridor the time shifts between data and synthetics are 1.5 s larger than those in corridor D.

3.4.2 SV Waves

Figure 3.6 shows an example of a comparison between data and synthetics for SV waves on both the radial and the vertical components. These comparisons are made at periods of 6 s and longer, so the cross-correlation coefficients remain quite high even though the fits are not particularly good. There are similar azimuthal variations in the S-wave cross-correlation results (Figure 3.7ab). The azimuthal time-shift offset is about twice as large as for P waves. This consistent azimuthal offset cannot be explained by increasing the velocities of the 1-D background model, since this will not change azimuthal differences but only cause uniform baseline shifts. There are two possible explanations for the offset: the slab in the regional model [*Zhao et al.*, 1994] (above 500 km and in the azimuthal range from 80°–150°) is not fast enough or, in the same azimuthal window, the regional model [*Zhao et al.*, 1994] does not resolve the slab inside the transition zone. Since the 3-D tomographic model has high resolution in the slab above the transition zone, a slab anomaly inside the

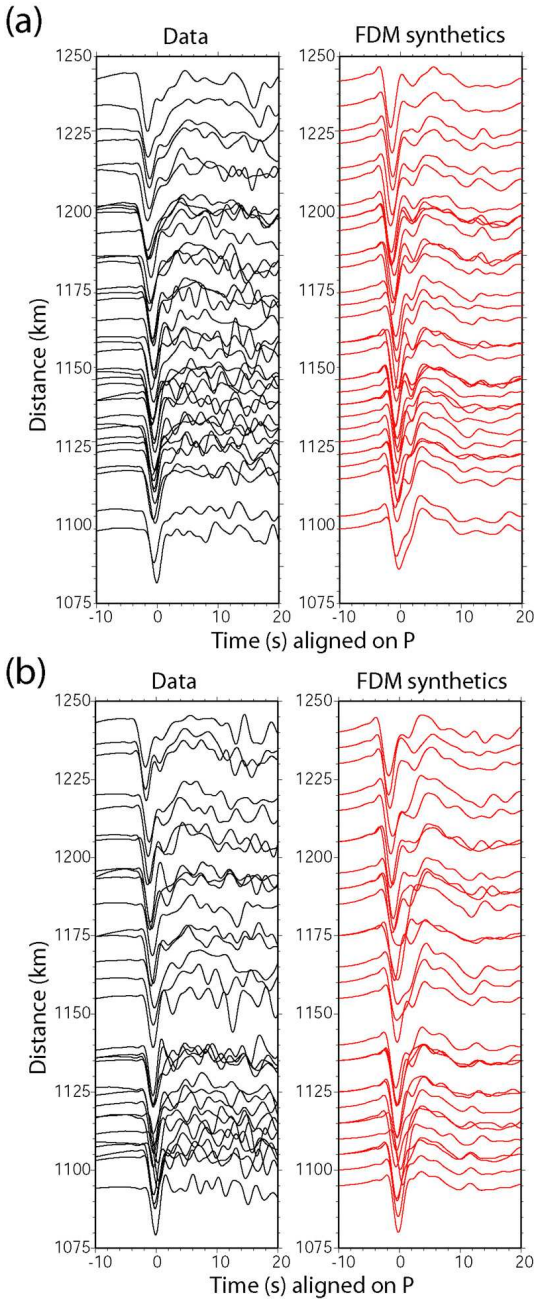

Figure 3.4: Waveform comparison between data (event 20020915) and 2-D FDM synthetics calculated for the regional model [*Zhao et al.*, 1994]. Data are aligned on the direct P wave based upon 1-D reference model IASPEI91, and synthetics are aligned with the data using the time shifts shown in Figure 3.5c. (a) Distance profile in the azimuthal range 120–130°. (b) Distance profile in the azimuthal range 130–140°.

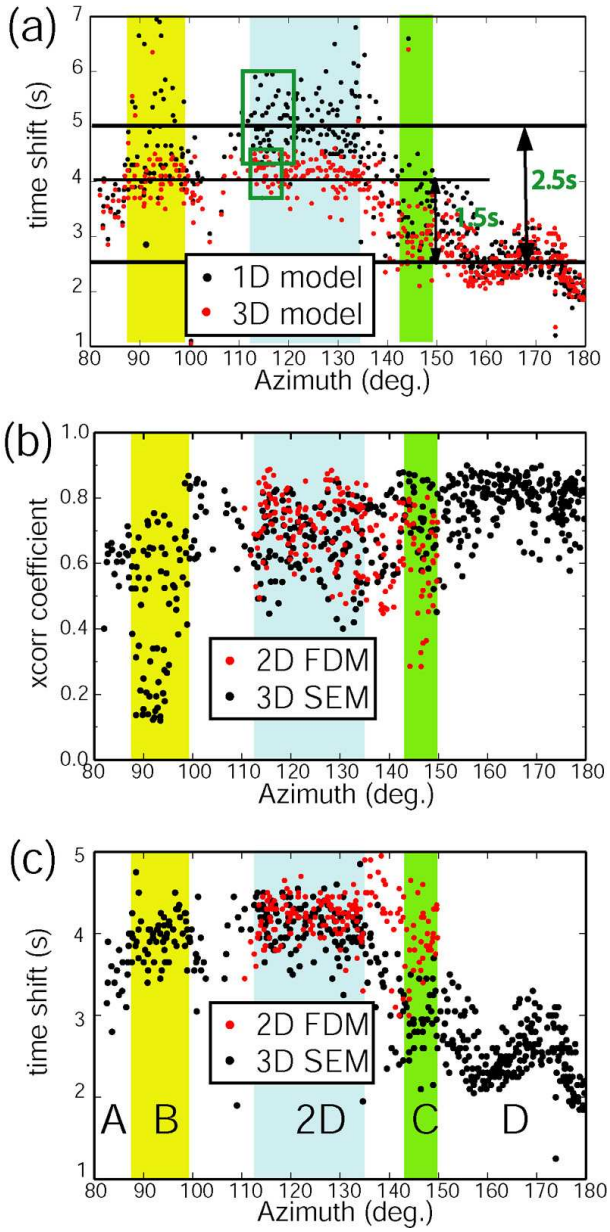

Figure 3.5: Cross-correlation traveltime anomalies between data and 3-D SEM synthetics for P waves (event 20020915). Azimuthal windows A, B (yellow), 2D (light-blue), C (green), and D labeled in the bottom panel correspond to the corridors indicated in Figure 3.1a. (a) Comparison of cross-correlation traveltime anomalies between the data and 3-D SEM synthetics for the 1-D model (IASPEI91, black dots) and Zhao et al.'s regional P-wave model (red dots). The black lines indicate average time shifts for all stations in regions with a slab (corridor 2D), or the no-slab region (corridor D), and the traveltime anomaly is indicated by this azimuthal time-shift offset. The 3-D regional tomographic model shown in Figure 3.1b (right) reduces the traveltime anomalies by almost half (from an average of 2.5 s to an average of 1.5 s) compared to the 1-D model. The model also reduces the scatter in the traveltime anomalies by half for stations in the azimuthal range 110–120°, as denoted by the green boxes. (b,c) Comparison of cross-correlation coefficients (middle panel) and traveltime anomalies (bottom panel) between data and FDM (red dots) & SEM (black dots) synthetics calculated for the regional model.

transition zone is the more reasonable explanation, and later 2-D waveform modeling will confirm this interpretation. From Figure 3.7ab we also note that radial SV waveforms are much less sensitive to the velocity structure than vertical SV waveforms. For all four S models we examined, the waveform similarity between data and synthetics is high and almost the same for all azimuths on the radial component, but the similarity decreases on the vertical component in the azimuthal windows where the slab exists. Least-squares analysis suggests a P-to-S scaling value $f = 1.5$–2.0.

3.4.3 SH waves

While the P and SV waves exhibit reasonable fits, the SH waves have low enough cross-correlations to make the traveltime delay estimates unreliable except in restricted windows. A sample of SH waveforms is presented in Figure 3.8, where the data are plotted as a function of azimuth and aligned on the IASPEI91 traveltime. The 2-D FDM synthetics were generated from 2-D cross-sections of the global and regional models (Figure 3.1b), as explained earlier. Note the change in polarity near 145°, which appears to be near a sign flip in the data, perhaps with about a 5° shift to near 150°. Such discrepancies are common, but since we will avoid modeling data near nodes in the SH radiation pattern we have not changed the source mechanism. However, the greater complexity in the full 3-D calculation near 150° relative to 175° is beginning to display waveform distortion due to 3-D multipathing near the nodes. Working with a large array of stations helps remove source complexity issues, contrary to dealing with multiple sources and a few stations. Moreover, difficulties due to uncertainties in locations and origin times are avoided, and relative timing between stations becomes more definitive. Note that the observed traveltimes at stations near 115° are nearly 10 s earlier than at 175°, and that this is largely predicted by the tomographic model ($f = 2.0$). We have modeled the SH-waves in these azimuths with an 8 s source duration and assumed the same time history for other paths. For all the records within the distance range of 1130–1150 km the SH waveforms are obviously broadened in the azimuthal range from 115–150°, where the slab should have the strongest effect based on the cross-sections displayed in Figure 3.1. The maximum broadening happens at around

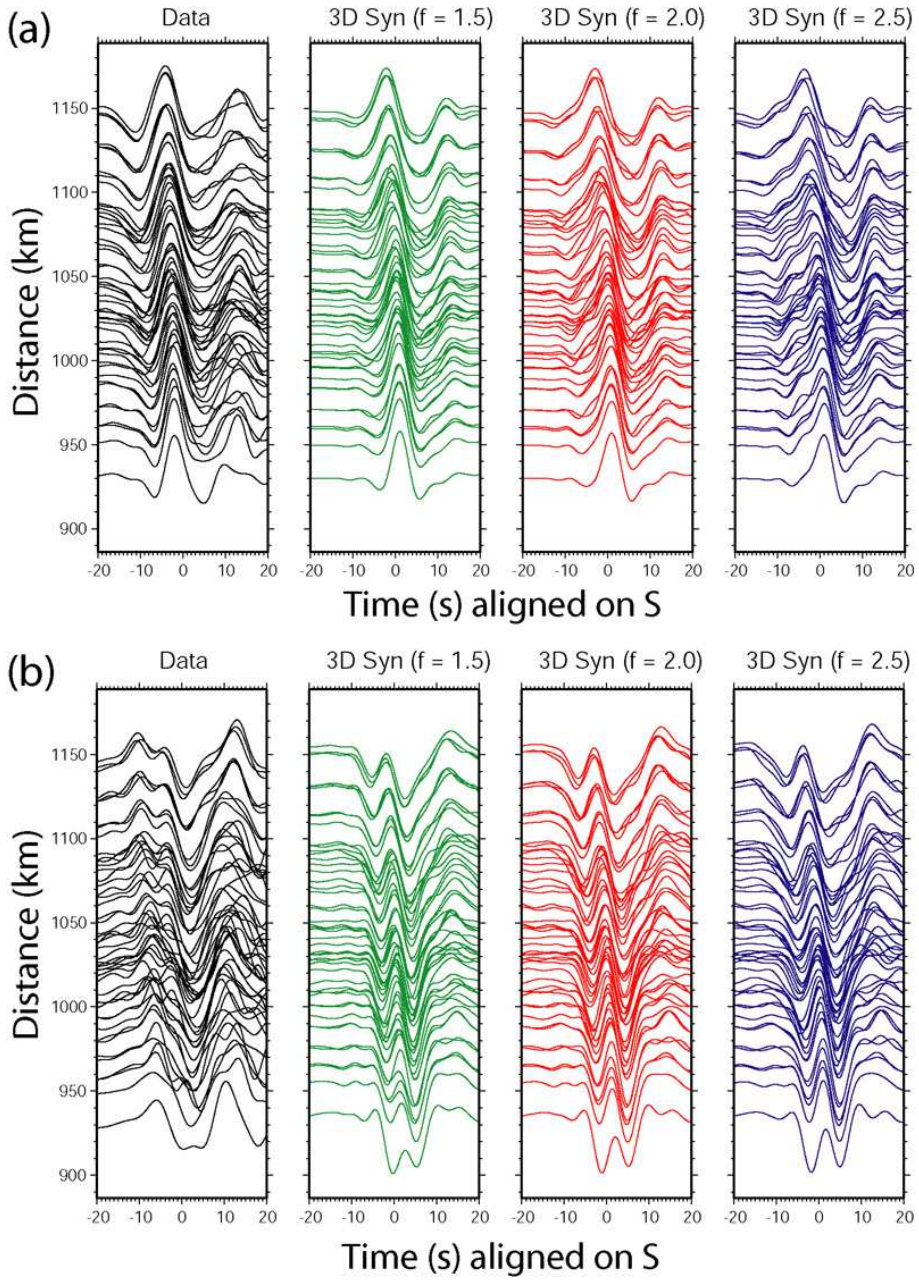

Figure 3.6: Waveform comparison between data and 3-D SEM synthetics in the azimuthal range 110–120° for event 20020915. The seismograms are plotted as function of distance and are aligned on the direct S arrivals for 1-D model IASPEI91. The SEM synthetics are calculated for three different S models with scaling factors $f = \delta \ln \beta / \delta \ln \alpha = 1.5$, 2.0, and 2.5. All seismograms are bandpass filtered between 6 s and 29 s. (a) Radial S waves. (b) Vertical S waves.

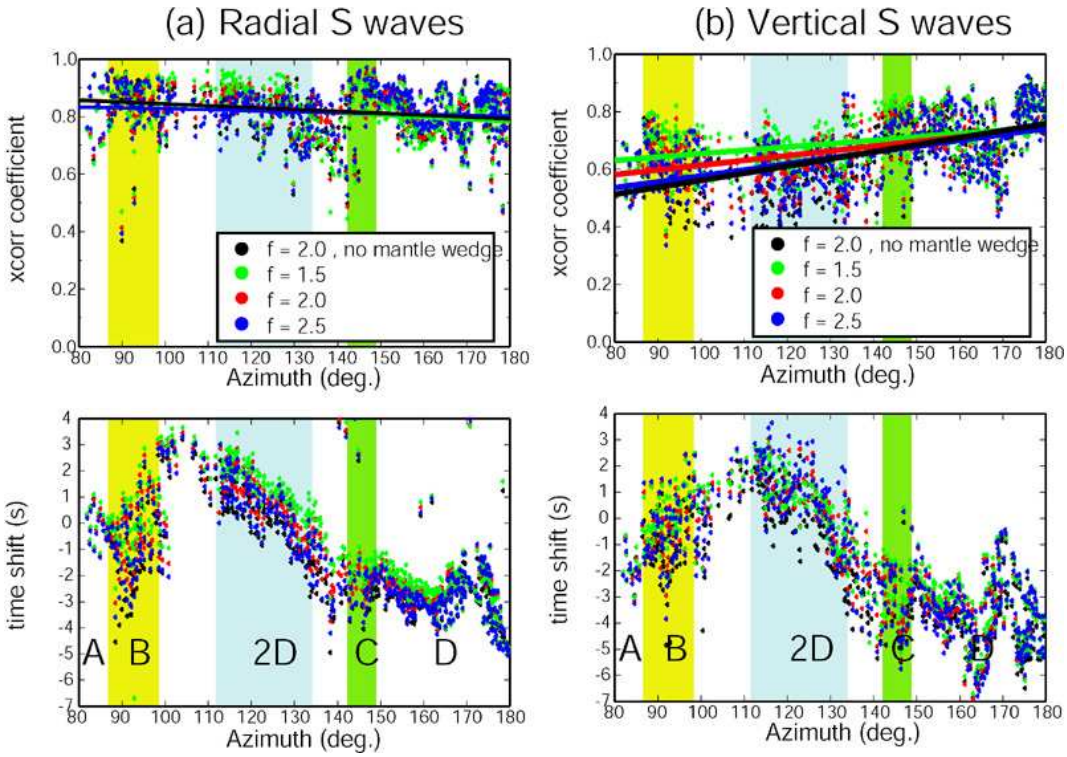

Figure 3.7: Cross-correlation between data and SEM synthetics for S waves calculated for four different S models, with different scaling factors $f = \delta \ln \beta / \delta \ln \alpha$ to the P-wave model. The cross-correlation results for the four different S models are indicated by the green dots ($f = 1.5$), red dots ($f = 2.0$), blue dots ($f = 2.5$), and black dots ($f = 2.0$ inside the slab only, no mantle wedge). (a) Radial S waves. (b) Vertical S waves. Note that models with $f = 1.5$–2.0 produce S-wave synthetic waveforms more similar to the data on the vertical component.

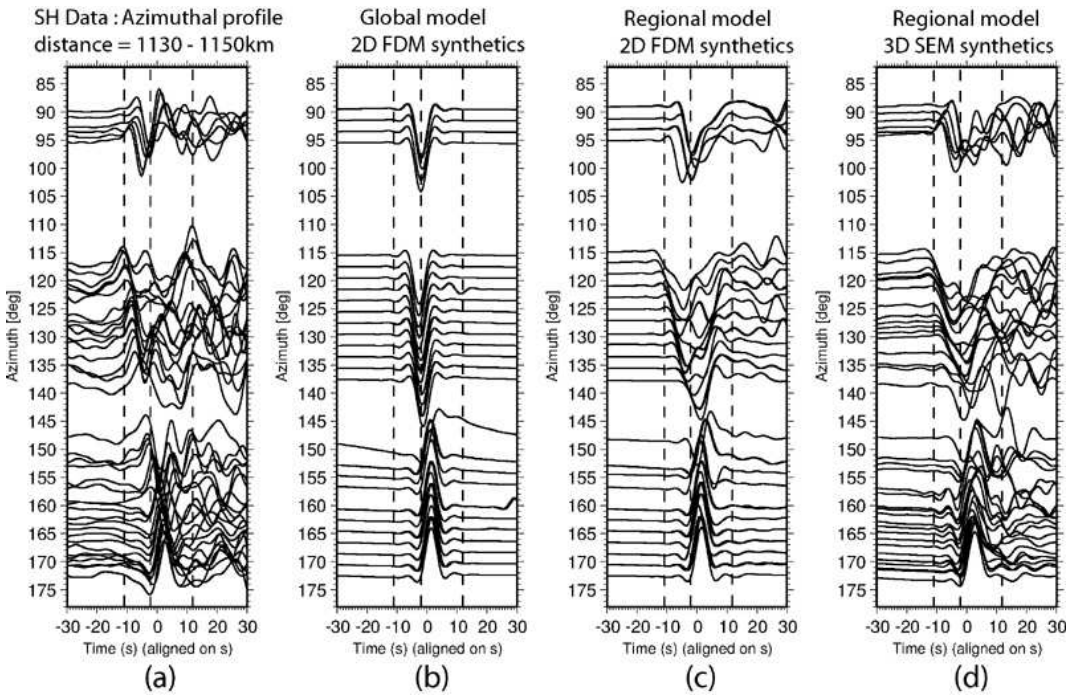

Figure 3.8: Azimuthal ('fan-shot') profiles for the SH wave (displacement) and the corresponding synthetics. All seismograms are aligned on the direct S arrivals calculated based upon 1-D model IASPEI91. The S-wave models used in the simulations are derived from the P-wave model based upon a scaling factor $f = \delta \ln \alpha / \delta \ln \beta$. The three vertical dashed lines align, respectively, with the onset of the most advanced S wave, the onset of the least advanced S wave, and the end of the most widened S wave in the data profile. (a) Azimuthal profile for SH data from event 20020915 recorded by stations at roughly the same epicentral distance (1130–1150 km), marked by the red circles in Figure 3.9. (b) 2-D FDM synthetics calculated for Zhao's global model. (c) 2-D FDM synthetics calculated for Zhao et al.'s regional model. (d) 3-D SEM synthetics calculated for Zhao et al.'s regional model.

117°, where the duration of the entire SH wavetrain is nearly 23 s. The synthetic predictions for the regional tomographic model explain some of the observed complexity, while the global model predictions are nearly 1-D-like simple waveforms. As pointed out earlier, the data for azimuths between 115° and 119° are quite well behaved, in general agreement with the 2-D geometry. Moreover, the 2-D FDM synthetics and the 3-D SEM synthetics are quite similar. Thus it appears that for this corridor we can explore 2-D models and use 3-D SEM synthetics subsequently as a check. The waveform data shown in Figure 3.8 were recorded along an arc in distance (from 1130 km to 1150 km), as displayed in Figure 3.9. A gap in coverage occurs between 115° and about 95°, where the islands have a break. A normal record section with data plotted relative to distance is useful to study multi-pathing

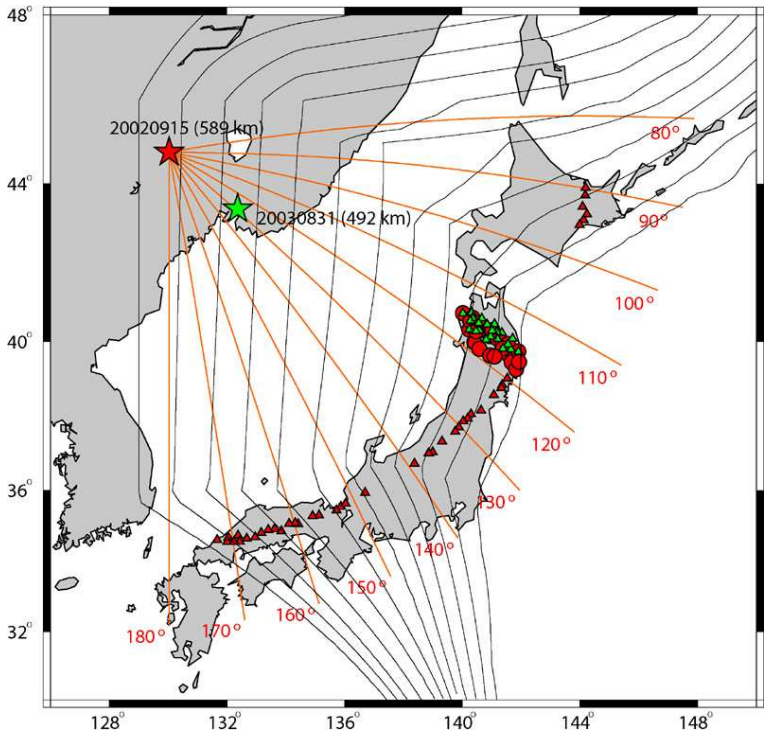

Figure 3.9: Map of the Japan subduction zone area. Black lines indicate slab contours used in the regional tomographic inversion by Zhao et al. (1994). For event 20020915 (red star) the red triangles denote Hi-net stations with almost the same epicentral distance (1130–1150 km); the red circles denote stations within the narrow azimuthal range 115–119° whose corresponding raypaths sample the slab beneath corridor 2D shown in Figure 3.1a. The green triangles indicate the selected stations for event 20030831 (green star) whose great circle paths sample the same corridor as event 20020915. Red lines indicate representative source azimuths for event 20020915.

in the plane of propagation, or for detecting internal slab structure. Stations with an azimuth of $\sim$115° are well suited for such an analysis. Based upon a comparison between stacked SH-data and FDM synthetics for an S model scaled to Zhao et al.'s P model with $f = 2$, we can see that this model explains neither the SH traveltimes nor the SH waveforms as a function of epicentral distance (Figure 3.10). The first arrivals in the data are gradually advanced relative to IASPEI91 with increasing distance. The synthetic first arrival for a station at a distance of $\sim$ 925 km is 2.5 s slower than the data, and the differences between the synthetics and the data become less with increasing distance. In terms of waveforms, the observed secondary arrivals appear only at distances greater than 1050 km, but in the synthetic profile waveform widening occurs at much closer distances ($\sim$ 960 km) and the

later arriving up-swing phases in the data are not present in the synthetics. We interpret the first arrival as the slab phase, since it is advanced by the fast slab relative to the ambient mantle. At large distances, the propagation paths tend to be closer to the slab interface and thus are even more advanced by the fast slab. The secondary up-swing phases at distances greater than 1050 km (Figure 3.10) are probably caused by slow anomalies (see Section 4.1). Our 2-D waveform modeling thus proceeds by constructing a new slab model from the regional model to minimize the traveltime misfit of the slab phases, and adding low-velocity structures to produce the later arriving up-swing phases using a combination of trial-and-error and grid search.

3.5 Construction of the 2-D Slab Model

The regional model [*Zhao et al.*, 1994] underpredicts the advancing of the slab phase for stations at small distances (Figure 3.10), and this can be explained by the lack of a slab near the earthquake source, since traveltimes at small distances are particularly sensitive to near-source velocity anomalies. In the global P model (Figure 3.1b) [*Zhao*, 2001], we see a stagnant slab pattern inside the transition zone. Thus it is necessary to add a slab anomaly in the transition zone of the regional model.

For modeling purposes, we specify several simple polygons with uniform S-wave velocity anomalies: the slab above the transition zone with a dip angle of 24° and the mantle wedge, whose shapes and anomalies are determined by capturing the major features of the regional model [*Zhao et al.*, 1994]; the slab inside the transition zone, which is flattened toward the west, with its dip angle on the eastern edge and velocity anomaly undetermined. There are two end-member models produced by the following two possible scenarios: the rigid slab subducts into the transition zone with the same dip angle as on the eastern edge, or, after the slab penetrates the 410 discontinuity, the slab sinks vertically and flattens toward the west.

In Zhao et al.'s regional model the thickness of the slab is pre-determined to be 90 km, and the pre-defined position of upper boundary is based upon previous studies of seismicity and later arrivals [*Zhao and Hasegawa*, 1993]. *Zhao et al.* [1994] included the slab in

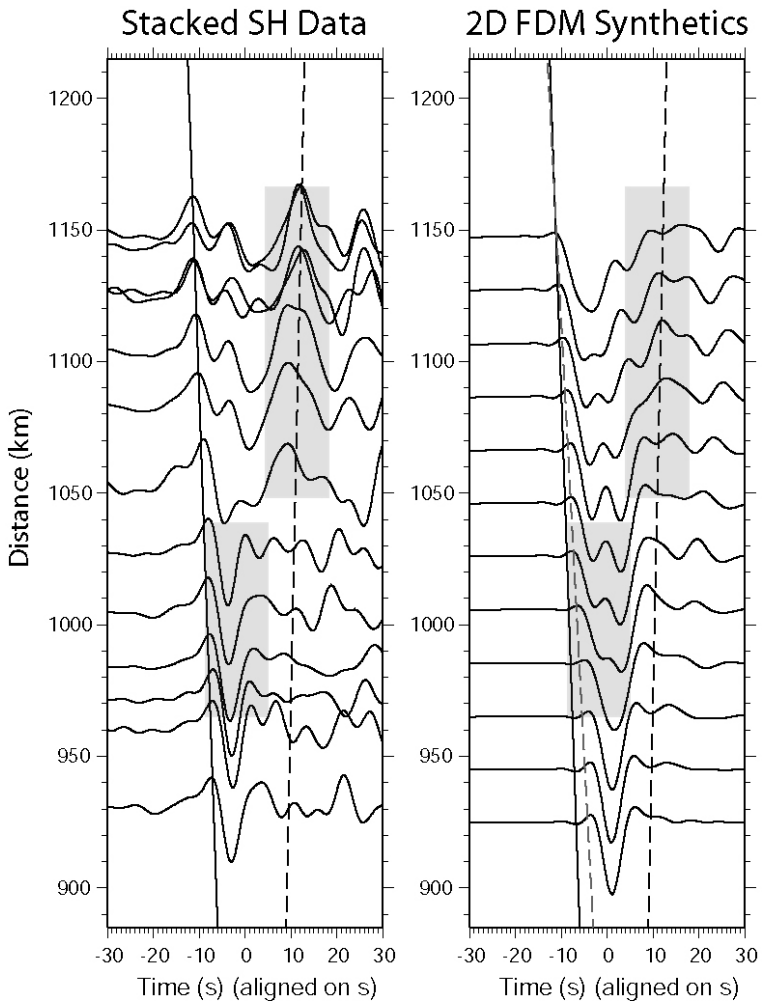

Figure 3.10: Comparison between stacked SH data and FDM synthetics. The FDM synthetics are calculated for an S model scaled to the regional P model with $f = 2$. The records before stacking come from the stations marked by red circles in Figure 3.9. Every trace in the data record section represents a stack of records from a 2° azimuthal window. The solid lines indicate the approximate first S arrival in the data. The gray dashed line in the right panel indicates the approximate first S arrivals in the FDM synthetics. The black dashed lines in both panels align with the peak of the later-arriving up-swing phases for stations with an epicentral distance greater than 1050 km. Waveform differences between data and synthetics are highlighted by the gray boxes.

the initial model for inversion. The final tomographic slab image in the regional model thus represents a better model with constraints from both seismicity and arrival times. We want to test if increasing the slab thickness affects the waveforms. Therefore, for each of the base models we calculate 2-D synthetics with different slab thicknesses above the transition zone (thicknesses of 90 km and 120 km, as shown in Figure 3.11). All the base models with a slab inside the transition zone ($\delta \ln \beta = 5\%$), a slab above the transition zone ($\delta \ln \beta = 6\%$), and a mantle wedge ($\delta \ln \beta = -4\%$) produce synthetics which fit the traveltimes of the first arrivals. But the synthetic waveforms change with distance for the different base models. The synthetic waveform is widened at small distances for the models shown in Figure 3.11a, which indicates that near-source scattering is very strong due to the close distance between the source and the eastern edge of the slab inside the transition zone, and this scattering is even stronger when the slab is thinner. The base models shown in Figure 3.11b produce synthetic waveforms more similar to the data for stations at smaller distances. But the thinner slab (thickness of 90 km) produces widened slab-phase waveforms for stations at larger distances, which are not observed in the data. The base models with a slab thickness greater than 120 km produce similar waveforms to the one with a thickness of 120 km. The up-going wavefronts with this specific source-station geometry are only sensitive to the upper slab interface and partially sensitive to the bottom interface if the slab is thin. When the slab thickness is greater than 120 km, the bottom interface does not significantly affect the slab-phase waveform. Thus, the base model is fixed with a slab thickness of 120 km, and the eastern edge of the slab inside the transition zone is located far enough away from the source so as not to produce significant near-source scattering. We specify the dip angle inside the transition zone to be 33°, which appears sufficient for the purpose of this waveform modeling study.

3.5.1 Slab Models with a Low Velocity Layer (LVL)

Although the modified base model significantly reduces the traveltime misfits, it does not produce the secondary arrivals present in the data, especially at distances larger than 1050 km. A reversal of polarity of the later arriving phases would indicate the existence of

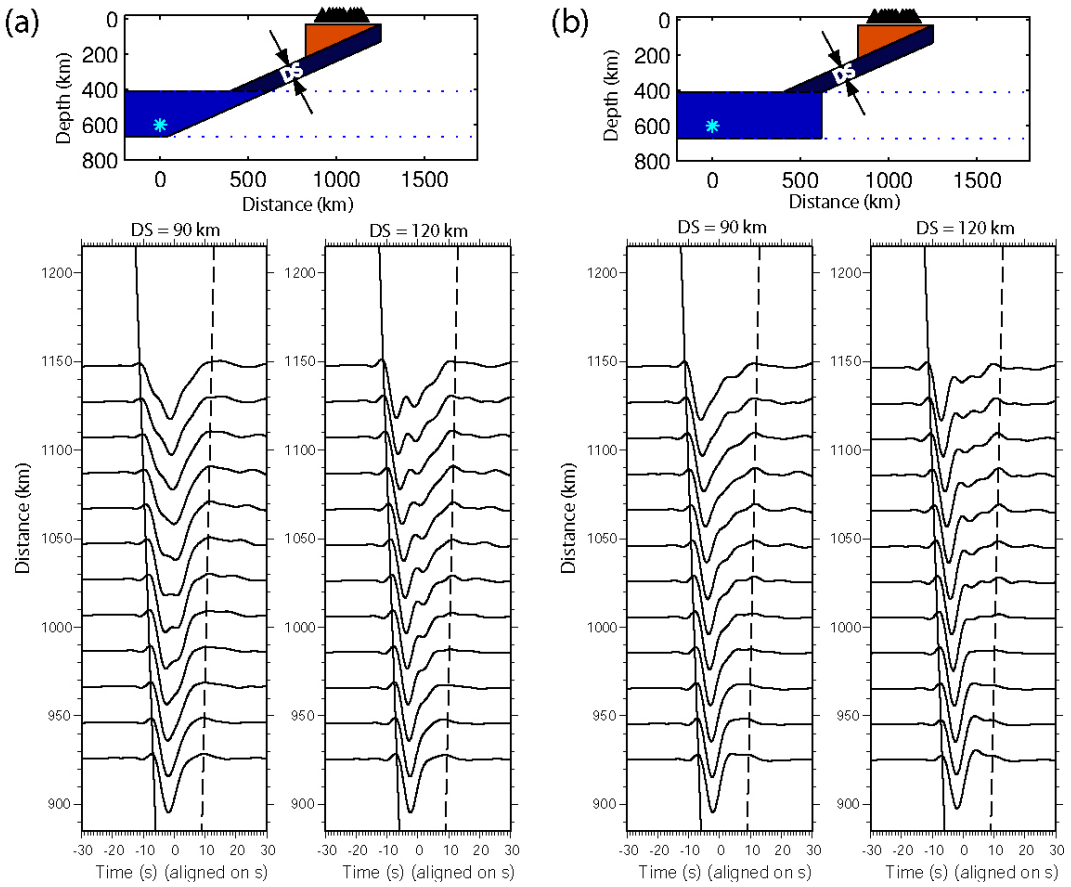

Figure 3.11: FDM waveforms for base models with a slab inside the transition zone. Mantle wedge (orange polygon): $\delta \ln \beta = -4\%$. Slab above the 410 km discontinuity (dark blue polygon): $\delta \ln \beta = 6\%$. Thickness of the slab (DS): 90 km or 120 km. Slab inside the transition zone (blue polygon): $\delta \ln \beta = 5\%$. The dark solid and dash lines are the same as those in Figure 3.10. (a) The eastern edge of the slab in the transition zone has the same dip angle as the slab above. (b) The eastern edge of the slab in the transition zone is vertical. The first two panels on the bottom denote FDM record sections for the model shown in (a) with slab thicknesses of 90 km and 120 km, respectively. The third and fourth panel on the bottom denote FDM record sections for the model shown in (b) with slab thicknesses of 90 km and 120 km, respectively.

a low-velocity waveguide along the propagation path, with high velocities on either side. There are inferences of such a low-velocity layer with a thickness of 5–10 km and relative P-wave velocity perturbations $\delta \ln \alpha$ of -6% on top of the slab beneath north-eastern Japan from differential travel time between direct P and and P to S converted phase [*Matsuzawa et al.*, 1986]. Observations of seismic signals with low-frequency onset followed by high-frequency coda have been modeled by *Furumura and Kennett* [2005]. Motivated by this study, we added a low-velocity layer (LVL) on top of the slab (Figure 3.12b), and describe the LVL with the following three parameters: its thickness (DL), its depth extent (HL), and its relative shear-wave velocity perturbation ($\delta \ln \beta$). In general, as discussed in *Martin et al.* [2003], the velocity contrast between the LVL and its surroundings influences the waveform most. However, as discussed in the previous section, the velocity perturbation inside the slab is well constrained in the base model by differential traveltimes with increasing distances, and thus $\delta \ln \beta$ inside the LVL is a controlling parameter. We tested nine types of models with different LVL geometries (DL = 10 km, 20 km, and 30 km, and HL = 200 km, 300 km, and 400 km) (Figure 3.12c,d,e). We fix DL and HL for each of the nine combinations and perform a grid search for the best $\delta \ln \beta$ which produces significant later arriving up-swings with the right timing for stations at the maximum distance of 1150 km. The differential time between the onset of the SH wave and the peak of the later arriving up-swing is about 23 s at 1150 km. The waveform change is quite sensitive to the depth (i.e., length) of the LVL, and only models with depths approaching 300 km reproduce the characteristics of the observed waveforms at all distances.

When the LVL extends deeper (HL = 400 km), the energy trapped in the LVL arrives too early and causes too much pulse widening in the synthetics at close distances compared to the data. When the LVL is too shallow (HL = 200 km), there is insufficient energy trapping for the later arriving up-swings. Even if we make the LVL extremely slow with $\delta \ln \beta = -56\%$, -42% and -28%, corresponding to DL = 10 km, 20 km, and 30 km, respectively, the synthetic waveforms at distances of $\sim$ 960 km and traveltimes at distances larger than 1050 km disagree with the data. For the best fitting models with a LVL length of $\sim$ 300 km there are still significant trade-offs between thickness DL and shear-velocity perturbation $\delta \ln \beta$, such that a smaller DL combined with a more negative $\delta \ln \beta$ can produce the same

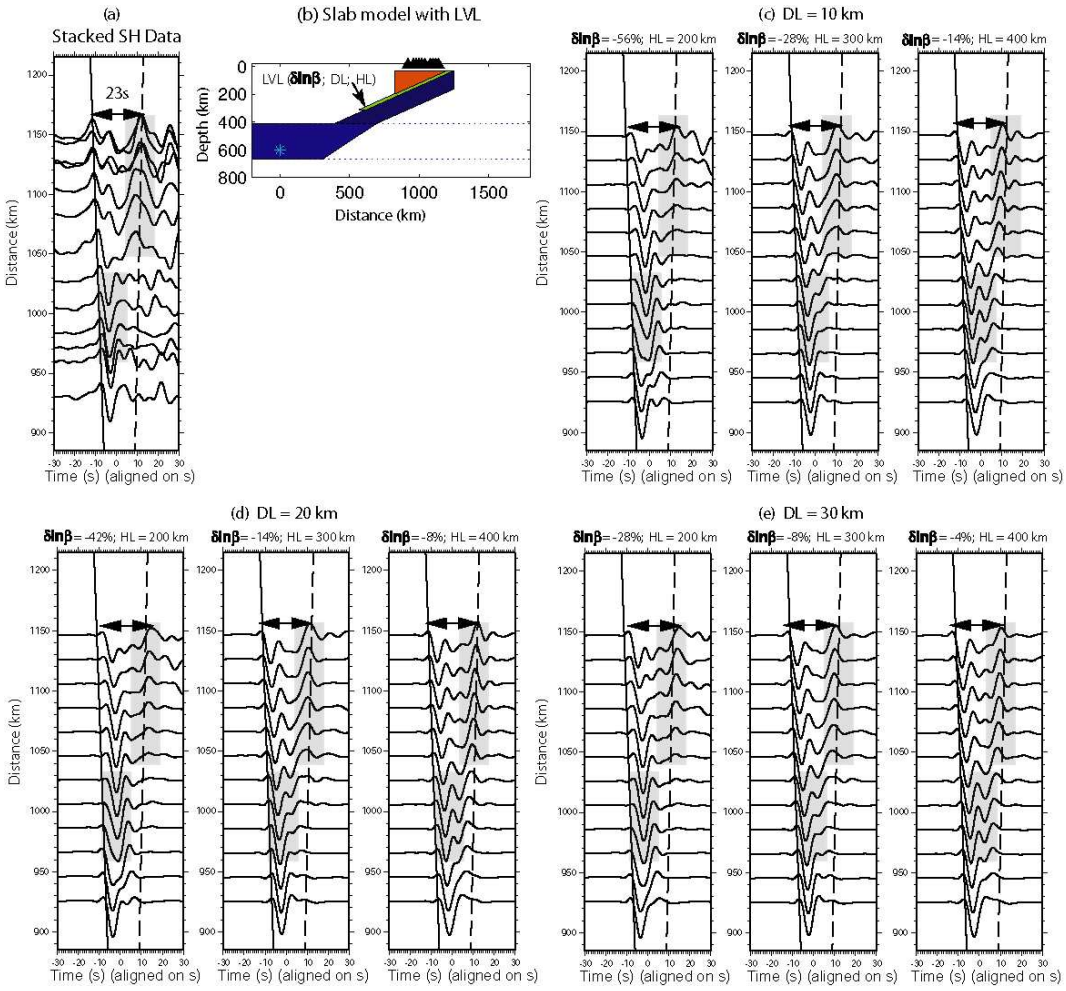

Figure 3.12: FDM simulations for slab models with a low velocity layer (LVL). (a) Stacked SH data. (b) The LVL is indicated by the green polygon. It is characterized by its thickness (DL), its maximum depth (HL), and its relative shear-wave velocity perturbation ($\delta \ln \beta$). The black triangles indicate station locations. (c,d,e) Synthetic waveforms calculated for nine models with different thicknesses DL (10, 20, or 30 km), and lengths HL (200, 300, or 400 km). The length of the bar with two-way arrowheads indicates the largest separation between the first arrival and the later arriving up-swing phase, which is 23 s at a distance of 1150 km. The dashed lines, solid lines, and gray boxes are the same as those in Figure 3.10. The comparison between data and synthetics indicates models with a LVL extending over a length of 300 km are preferable.

waveform features at all distances. The 2-D synthetics for this deep event thus cannot distinguish between a model with HL = 300 km, DL = 10 km, and $\delta \ln \beta = -28\%$; a model with HL = 300 km, DL = 20 km, and $\delta \ln \beta = -14\%$; and a model with HL = 300 km, DL = 30 km, and $\delta \ln \beta = -8\%$. Note that attenuation is currently not considered in the numerical simulations, and this may cause overestimation of either the layer thickness or the shear-wave velocity reduction. Thus, our investigation only provides upper limits for these two parameters. For the sake of simplicity, we will take the model with a 20 km-thick LVL as a starting point for further refined waveform modeling.

3.5.2 Mantle Wedge Models

Next, we investigate the heterogeneity in the mantle wedge by testing the three simple models shown in Figure 3.13. The slow part of the mantle wedge has an 8% shear-wave velocity reduction; models with an even slower mantle wedge alter the trend of traveltime with increasing distance. Overall, the heterogeneity in the mantle wedge does not change the waveforms very much. Adding the wedge-shaped low-velocity part (Model 2) helps the development of later arrivals, indicated by arrows in Figure 3.13d. Resolving detailed structure inside the mantle wedge would require data from closer and shallower events, as in the study by *Furumura and Kennett* [2005]. Our final 2-D model has the following characteristics (Model 2): in the upper mantle, the dip angle of the slab is $\sim 24^\circ$, and the slab has a uniform relative compressional-wave velocity anomaly $\delta \ln \alpha$ of 4.5% and a uniform relative shear-wave anomaly $\delta \ln \beta$ of 6.0%; inside the transition zone, the eastern edge of the slab has a dip angle of 33° or larger and the slab flattens toward the west, and inside the slab in the transition zone $\delta \ln \alpha = 3\%$ and $\delta \ln \beta = 5\%$. The Low Velocity Layer (LVL) on top of the slab is extremely slow with $\delta \ln \alpha = -7\%$ and $\delta \ln \beta = -14\%$, assuming the LVL is 20 km thick and extends down to 300 km; there is a slow region of the mantle wedge adjacent to the LVL with $\delta \ln \alpha = -4\%$ and $\delta \ln \beta = -8\%$. We convolve the raw synthetics with empirical source-time functions for both P and SH waves as discussed earlier. FDM synthetics are shown in (Figure 3.14) and these agree well with the observations at distances most affected by the slab.

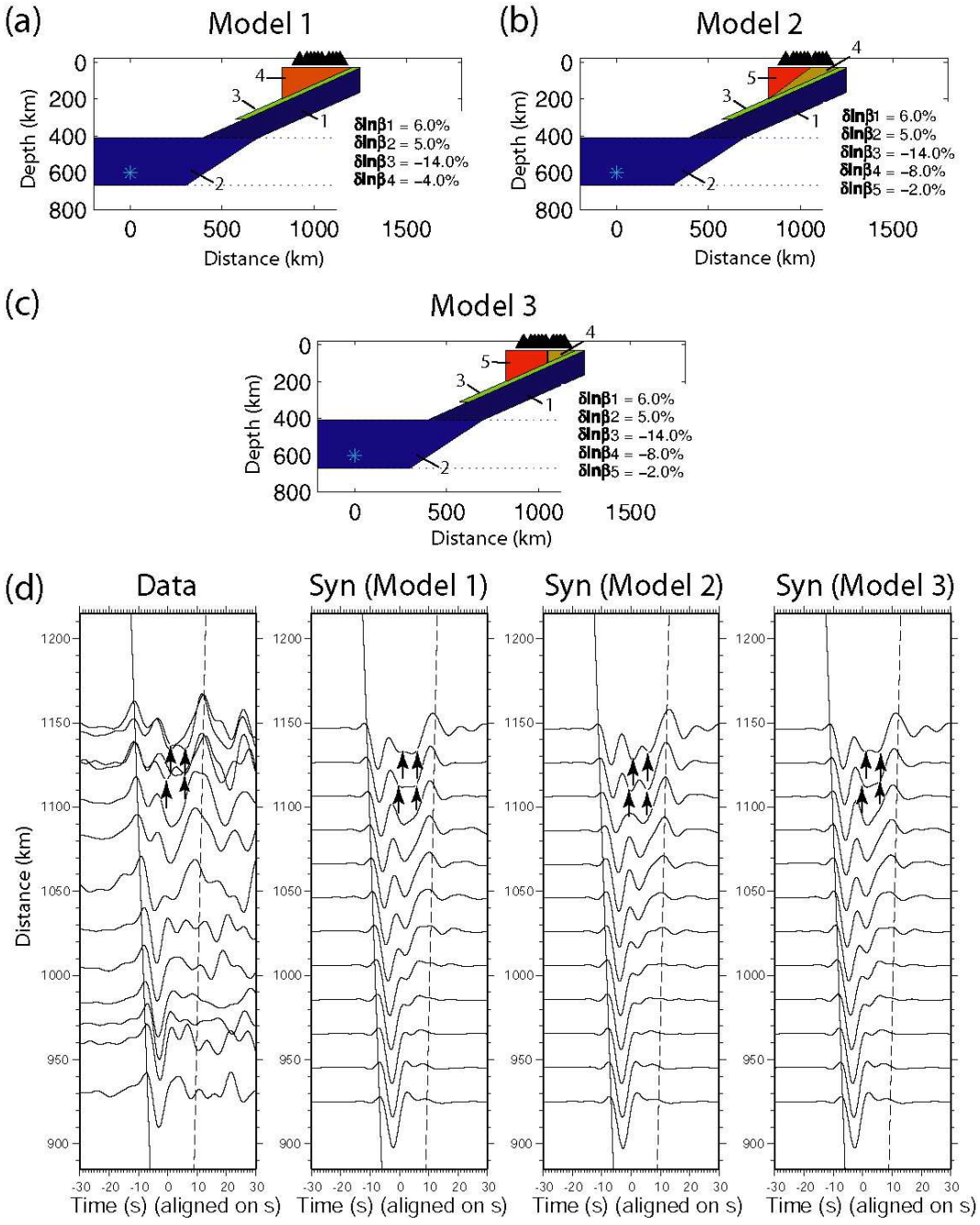

Figure 3.13: FDM simulations for three models with different types of mantle wedges. (a) Model 1: Uniform mantle wedge. (b) Model 2: Mantle wedge with a slow region (yellow) starting at 200 km. (c) Model 3: Mantle wedge with a slow part (yellow) starting at 100 km. (a,b,c) The shear-wave velocity perturbation inside each region of the model is indicated by values of $\delta \ln \beta$ shown in the lower right corner of the model. (d) Data and synthetic waveform comparison. The arrows indicate multiple later arrivals at large distances. The left column shows the SH data, and the subsequent columns show SH FDM synthetics for models 1 (a), 2 (b), and 3 (c), respectively.

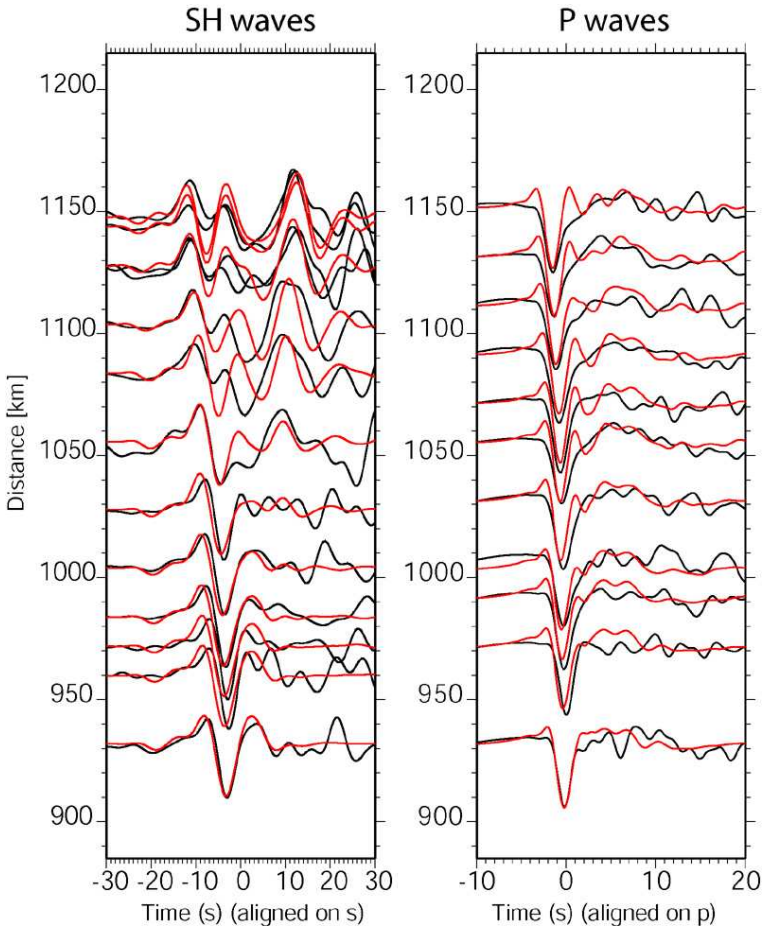

Figure 3.14: Waveform fits between the data (black lines) and FDM synthetics (red lines) for event 20020915. SH waves are bandpass filtered between 6 s and 29 s, and P waves are bandpass filtered between 1 s and 29 s. The synthetics are obtained by convolving the numerical Green's function with the empirical source-time function.

3.6 3-D SEM verification

In this section we use the SEM to validate Model 2 (Figure 3.13b), which is derived from tangential S waveforms for one event (20020915). We calculate SEM synthetics for all 3 components for the same event, as well as a complementary shallower event (20030831). We implement Model 2 in the 3-D SEM mesh by sweeping it cylindrically around a vertical axis through the epicenter, since it is reasonable to assume that the structure of the region beneath the examined stations is two-dimensional based on discussions in the previous sections.

Figure 3.15 shows 3-component comparisons between data and 3-D SEM synthetics for both events. Event 20030831 is almost 100 km shallower than event 20020915, recorded by stations within the same corridor (Figure 3.9), so the raypaths sample similar regions of the slab. The comparison between data and synthetics in Figure 3.15 indicates the quality of the fit on all three components. In general, the synthetics calculated for Model 2 capture the correct differential traveltime for the first arrivals at different distances, the dispersion characteristics of the SH waveforms at large distances, and the relative amplitude ratio between the first and later arrivals for vertical S waves. For the same source-time function, SEM simulations at twice the resolution lead to the same conclusions for S waves, thereby demonstrating that the resolution of the SEM mesh shown in Figure 3.3 is sufficient to capture Model 2. For P waves only the high-resolution results can capture the distortion around 3 s, which is illustrated in Figure 3.15; there is a 2.5 s baseline timeshift applied to all traces. Notice the arrival times for vertical P waves are well captured by Model 2.

3.7 Discussion

From our 2-D FDM waveform modeling we conclude that the later arriving up-swing SH phases can be produced by a low-velocity layer on top of the slab. The waves propagating along the dip of the slab trap a significant amount of energy inside the low velocity layer, which manifests itself as large-amplitude up swings in the seismogram. These up swings are also observed at other stations located in the azimuthal range from 110°–140°, thus the

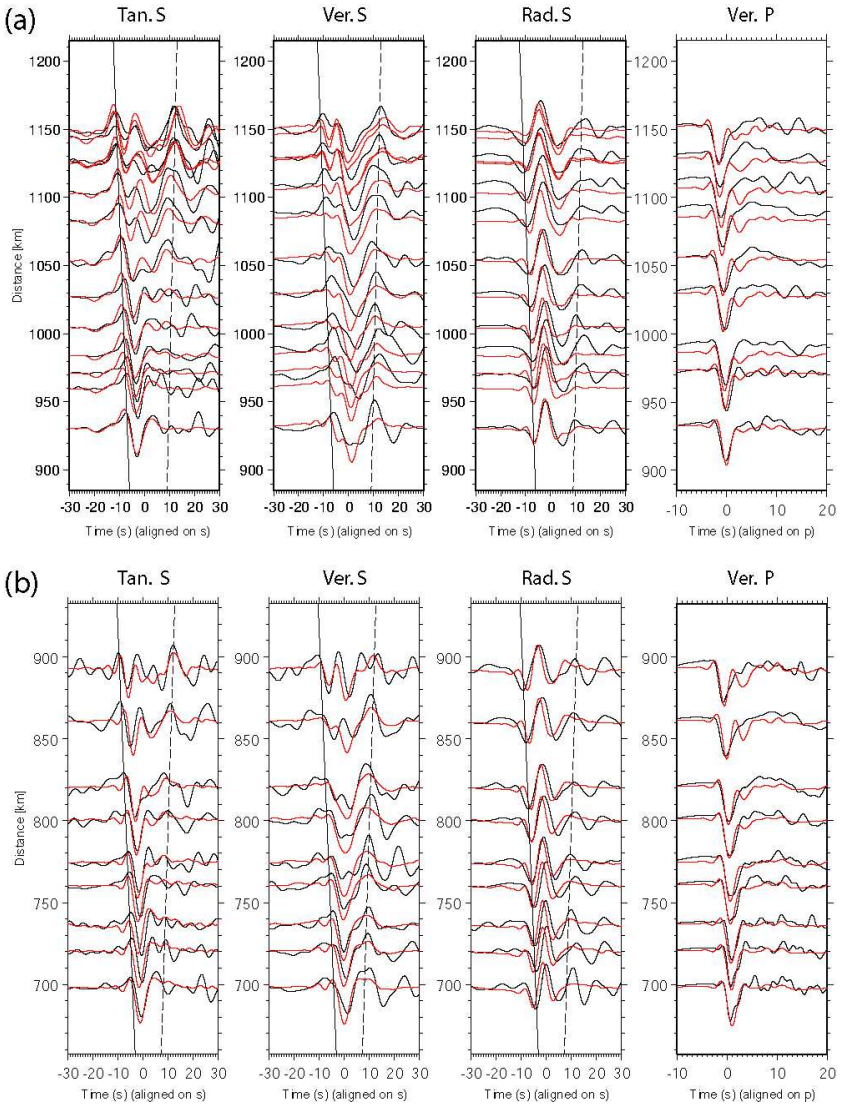

Figure 3.15: Three-component S-waveform and vertical P-waveform comparisons between data (black lines) and 3-D SEM synthetics (red lines). SEM synthetics are calculated for Model 2 in Figure 3.13b. Both data and synthetics for S waves are filtered between 6 s and 29 s, and for P waves between 3 s and 29 s. (a) Event 20020915 (depth 589 km). (b) Event 20030831 (depth 492 km). Model 2 is our preferred model and fits the data for both events on all three components adequately.

LVL can be a general feature on top of the slab beneath north-eastern region of Honshu island.

In order to better understand energy trapping in the slow waveguide, we examine two additional models based upon 3-D SEM simulations: one model has a slab with a LVL but no mantle wedge; the other has only the slab and no low-velocity anomalies (Figure 3.16). The simulation results for the first model show that on the tangential component of the stations beyond an epicentral distance of 1050 km the later arriving up-swings still appear, but their amplitude is not as large as for Model 2. This indicates that a slow mantle wedge helps energy to accumulate in the later arrivals, which is consistent with what is observed on the vertical component. The first-arriving pulses on the vertical component have relatively large amplitudes compared to those calculated for Model 2. For the second model with only the slab, the first arrivals advanced by the slab are predominant on the tangential component, but there are almost no secondary S arrivals. Radial S waves show much larger amplitude ratios of the first arrival relative to the secondary arrival. Thus the 3-D SEM simulations further verify that an elongated slow waveguide helps to trap energy in the secondary S arrivals. On the radial component, S-wave dispersion for either model is not obvious, but the S waveform at a distance of 1150 km is clearly widened compared to those at closer distances. The cross-correlation results (Figure 3.17) further verify that Model 2 fits the SH waveforms and arrival times better than the regional starting model. For vertical S waves the improvement is not as obvious as for SH waves, but the overall waveform fits improve from an average cross-correlation of 0.6 to 0.7, and traveltime misfits for distant stations are reduced from 2 s to 0.5 s. The waveform fits for Model 2 with or without a mantle wedge are not substantially different, but waveforms in Model 2 with just the slab and no LVL are distinctly different. Thus the LVL is an important element in the final model, and the waveform fits are very sensitive to this structure, but not to the mantle wedge. These waveguide phenomena are clearly illustrated in the 2-D FDM snapshots of SH wave propagation shown in Figure 3.18. Note that the presence of the fast slab advances the wavefront, whereas the LVL and the slow mantle wedge both delay and amplify the wavefield. The wavefront is advanced by the fast slab, and at the same time, in the confined LVL waveguide with a thickness comparable to the wavelength of the S waves,

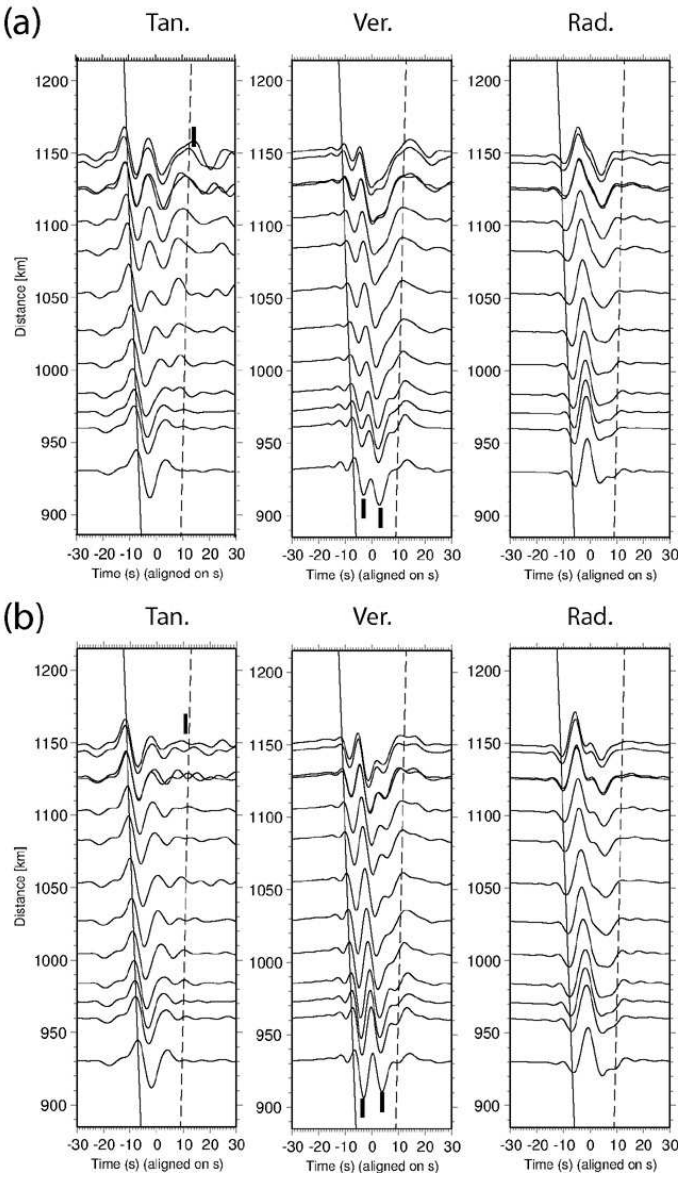

Figure 3.16: Three-component SEM synthetic waveforms for two different models. (a) Model 2 without a slow mantle wedge but with a LVL. (b) Model 2 with neither a slow mantle wedge nor a LVL. The black bars indicate the up-swing phases on the tangential component or the first and secondary arrivals on the vertical component. When there are no slow anomalies (neither a LVL nor a mantle wedge) the amplitude of the first arrival gets bigger compared to the secondary arrival on the vertical component, and the amplitude of the positive later arriving up-swings on the tangential component gets smaller.

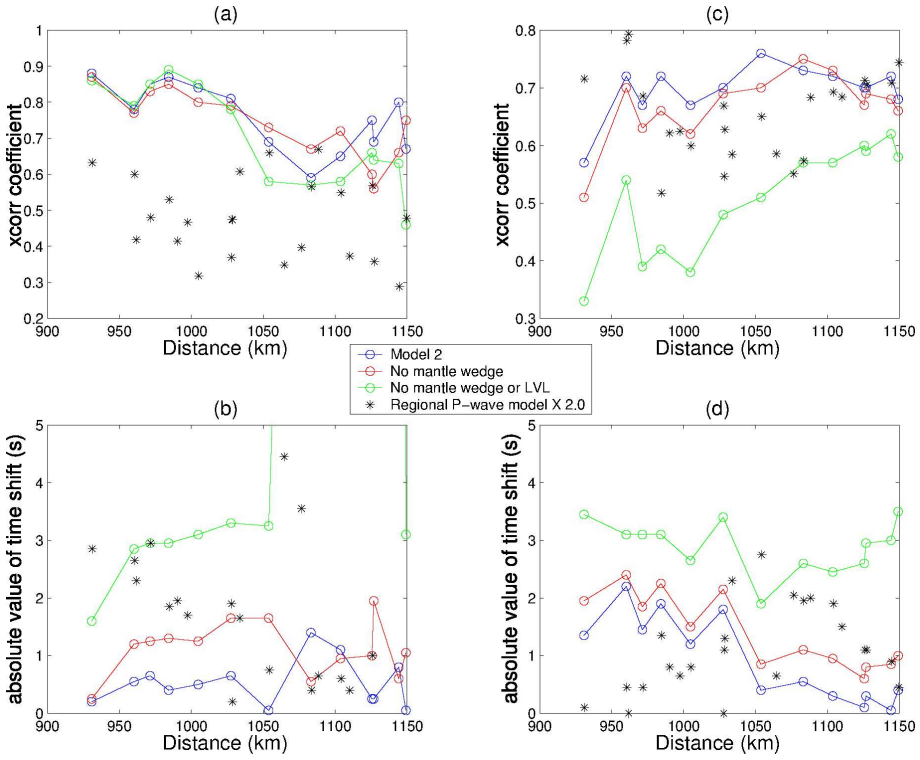

Figure 3.17: Comparison of cross-correlation coefficients (upper panel) and traveltime anomalies (bottom panel) between data and SEM synthetics calculated for the regional model (black stars), Model 2 (blue circles), Model 2 without a slow mantle wedge but with a LVL (red circles), and Model 2 with neither a slow mantle wedge nor a LVL (green circles). Stars indicate individual trace cross-correlation results and circles indicate stacked trace cross-correlation results. (a,b) SH waves. (c,d) Vertical S waves.

a slow wavefront with significant energy is formed from the original wavefield behind the fast wavefront (Figure 3.18a). Inside the slow mantle wedge the two wavefronts start to split again (Figure 3.18b), and these wavefronts reach the surface at different times. The undistorted part of the wavefront unaffected by the slab sweeps the surface, is recorded by stations closer to the epicenter, and displays only one SH pulse with a large amplitude in the seismogram (Figure 3.18c). For stations at intermediate distances, one slow and one fast wavefront are recorded, exhibiting the distinct two-pulse waveforms (Figure 3.18d). For stations further away, the seismograms record three or more wavefronts arriving sequentially, which results in more dispersed S waveforms with smaller amplitudes (Figure 3.18e). Note that the amplitude of these low-frequency waveforms decreases toward the eastern seaboard of Japan. This is different from the large abnormal intensity observed by *Furumura and Kennett* [2005], which is dominated by high-frequency (> 1 Hz) signals. The decoupling mechanism surely has some influence on the waveforms, and the degree of influence depends not only on the slab geometry, but also on the source and receiver locations. As the trapped waves approach the volcanic front, the slow mantle wedge gradually separates the slow wavefronts from the direct SH wavefronts. The bending slab decoupling mechanism of guided waves discussed by *Martin et al.* [2003] does not explain our observations, as the previously imaged slab in the 2-D cross-section has relatively constant dip even above 200 km, thus there is no obvious bending. The guided-wave decoupling is more likely being enhanced by the low-velocity mantle wedge, similar to a mechanism proposed by *Fukao et al.* [1983] and *Hori* [1990], the leaking of trapped energy. Moreover, even without the low-velocity mantle-wedge, a certain amount of trapped energy still can be transmitted to the stations near the LVL, as shown in Figure 3.16a, which could be due to the long travel paths, the near source velocity structure, and the relative position of the source with respect to the LVL.

As discussed previously, there are trade-offs between the width of the waveguide and the shear-wave velocity reduction inside the waveguide. The LVL must have a certain minimum width compared to the dominant wavelength of the shear waves. The characteristic period of the Hi-net data is about 6 s, and the average shear-wave velocity of the 1-D reference model in the upper mantle is 5 km/s. Thus the characteristic wavelength of the shear

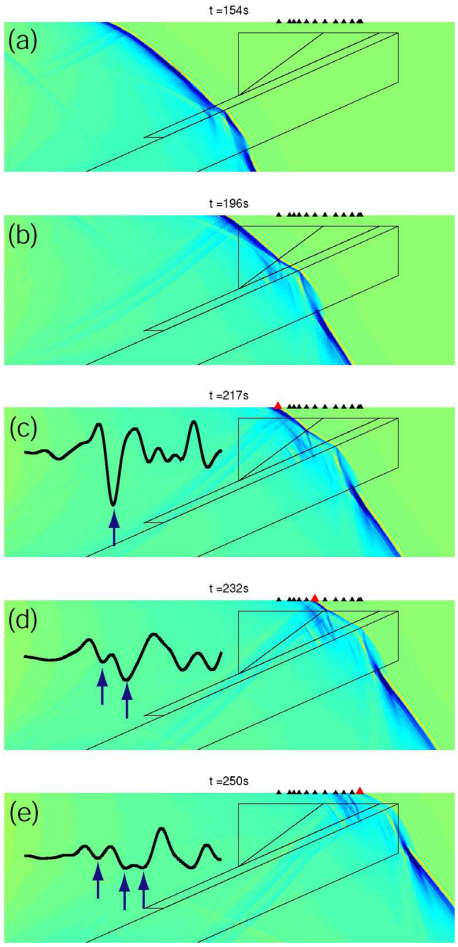

Figure 3.18: FDM snapshots of SH-wave propagation in Model 2. The black triangles indicate the station locations (shown as red circles in Figure 3.9). The color indicates the amplitude of the displacement field for an SH source located at a depth of 600 km. Negative displacement is shown in blue, and positive displacement is shown in red. The polygons with a black outline indicate the different regions in Model 2. (a) Snapshot at 154 s. Part of the wavefront energy starts to be trapped in the LVL, and the wavefront inside the slab is obviously advanced compared to the wavefront outside the slab. (b) Snapshot at 196 s. The energy in the wavefront is further redistributed to different branches when the wave enters the heterogeneous mantle wedge. (c) Snapshot at 217 s. The waveform recorded by the closest stations shows a single pulse. (d) Snapshot at 232 s. The waveform recorded by intermediate-distance stations starts to have a secondary arrival. (e) Snapshot at 250 s. The waveform recorded by the furthest stations shows multiple arrivals. Three distinct data waveforms are shown in the left half of panels (c), (d), and (e), recorded by stations marked by red triangles. The arrows indicate initial and late (multiple) arrivals. Note that the absolute amplitude decreases for multiple-arrival waveforms compared to single-pulse waveforms, which indicates an energy redistribution between multiple branches of the wavefront.

waves propagating inside the LVL is $\sim 30(1 + \delta \ln \beta)$ km. We experimented with different values of the width of the LVL for fixed values of $\delta \ln \beta$, and found that if the thickness of the LVL is less than half of this wavelength the waveguide becomes too narrow to trap sufficient energy. For example, with $\delta \ln \beta = -14\%$ the wavelength is approximately 26 km and only when its width is larger than 13 km does the waveguide trap sufficient energy.

Based on the SH-waveform modeling (Figure 3.12), the LVL exists in a depth range starting from the Moho to at least $\sim$ 300 km. The scaling factor f is found to be 1.5–2.0 based upon 3-D SEM simulations (illustrated in Figures 3.6 and 3.7), and therefore $\delta \ln \alpha$ is $-16 \pm 3\%$, $-8 \pm 2\%$, and $-5 \pm 1\%$ for a 10 km, 20 km, and 30 km thick LVL, respectively. Although there is a tradeoff between the thickness and $\delta \ln \alpha$, the depth extent of the LVL is well determined, and is twice as large as previously observed.

If we assume a 10-km-thick LVL comparable to the low-velocity waveguide observed in previous studies (e.g., *Matsuzawa et al.* 1986; *Abers* 2003), then the $\delta \ln \alpha$ we obtain here is double the 5–8% seen in other Northern Pacific arcs (Kurile, Alaska, Aleutian, N. Japan, and the Marianas). And if we assume a LVL with common $\delta \ln \alpha = -7\%$ in our preferred model, then it is 20 km thick and is thicker than that obtained by other investigators. For example, *Matsuzawa et al.* [1986] proposed a 5 to 10 km thick crust from differential travel time between direct P and and P-to-S converted phase. *Furumura and Kennett* [2005] suggests an 8-km-thick LVL with an 80-km-thick slab from the waveform similarity of simulated wave train to the observation at one single station, KMU. Their study is on the effect of elongated scatterers inside the plate, and is quite a unique approach. In contrast, we used broadband waveform data recorded by a dense array, and find that the later arriving SH up-swing is sensitive to both the thickness and $\delta \ln \beta$ inside the LVL. In particular, we found that, with $\delta \ln \alpha = -7\%$, a LVL less than 10 km thick cannot explain the up-swing phase; this is a very strong constraint.

The LVL atop the slab is often interpreted as descending hydrous mafic oceanic crust (less than 10 km thick), and these hydrous mafic rocks (e.g., gabbro, greenschist, epidote-blueschist/amphibolite) have lower seismic velocities than normal mantle until they dehydrate completely and convert to anhydrous eclogite. Given the age, convergence rate, and boundary condition of the subducting Pacific plate beneath NE Japan, the depth of com-

plete eclogitization is expected to be $\sim$ 150 km [*Peacock and Wang*, 1999; *Hacker et al.*, 2003a,b].

The LVL we observe here extends to greater depths than the maximum depth of stability for hydrous mafic lithologies. Thus, the NE Japan LVL probably is not the subducted oceanic crust (at least, not in the depth range of 150–300 km), and instead is more likely serpentinized peridotite, which retains its water to much greater depths [*Schmidt and Poli*, 1998]. There are two possible locations and origins of serpentine consistent with our observations: (1) a layer of serpentinized peridotite formed in the corner of the mantle wedge, in response to dehydration of oceanic crust at shallow depths [*Schmidt and Poli*, 1998], and gets dragged down along the top of the descending slab; or, (2) a layer of serpentinized peridotite formed in the lithospheric mantle of the down-going plate before its subduction, in response to hydrothermal circulation, perhaps related to faulting at the outer rise of the trench [*Ranero and Sallarès*, 2004; *Ranero et al.*, 2005]. These two scenarios are not mutually exclusive. Whether the layer of serpentinized peridotite lies above or below the oceanic crust is not resolved in this study due to tens of kilometers uncertainties in the locations of deep earthquakes and the interface between the slab and mantle wedge.

Nevertheless, our results require that serpentinization of peridotite is the dominant cause of the NE Japan LVL. Serpentinized peridotites, whether serpentine or chlorite dominated, are characterized by very large negative seismic velocity anomalies compared to the normal mantle (i.e., IASPEI91) to depths at least as great as the reactions that transform serpentine and/or chlorite into phase A and H_2O; this reaction should be accompanied by a circa 50% reduction in the amplitude of the velocity anomaly [*Hacker et al.*, 2003a]. The pressures at which these reactions occur along slab geotherms are poorly known but generally believed to fall between 6 GPa and 8 GPa ($\sim$ 180–260 km). This depth could be significantly greater for relatively cold slab geotherms. Based on the extrapolated trend of previously calculated slab geotherms (P-T paths with $P < 5$ GPa) [*Peacock and Wang*, 1999] for the NE Japan subduction zone, it is plausible that the geotherm associated with the bottom of the oceanic crust is sufficiently cold to intersect the conversion to phase A at pressures similar to the bottom of the LVL we observed. Conversely, the warmer temperatures in the mantle wedge above the slab should promote conversion of serpentinite to

phase-A-rich peridotite at lower pressures. Thus, these factors lead us to favor the hypothesis that the LVL beneath NE Japan reflects a layer of serpentinite in the oceanic lithosphere, beneath the oceanic crust.

Because fully serpentinized ultra-mafic mantle is 30% slower in compressional-wave velocity (α) than the normal mantle [*Hacker et al.*, 2003a], a 10-km-thick serpentine layer beneath NE Japan having a $-16 \pm 3\%$ of $\delta \ln \alpha$ should be 50% serpentinized ($\sim$ 7 wt% H_2O). Such a serpentine content requires that serpentinization took place in an environment with vigorous water supply. We suggest that such large amounts of seawater could have circulated into the interior of the slab beneath the outer rise of the Japan trench by way of extensional faults reaching tens of kilometers below the seafloor [*Kobayashi et al.*, 1998; *Kanamori*, 1971]. Note, however, that our results are also consistent with a thicker LVL having a lower average percentage of serpentine. Two potential sources of systematic error in the interpretation we present above are the relatively poor constraints on the phase diagram for hydrous peridotite at pressures above 5 GPa, and the relatively poor understanding of P-T paths followed by deeply subducted slabs.

3.8 Conclusion

We have generated 2-D and 3-D synthetic seismograms for an existing tomographic model of the subduction zone beneath Japan developed by *Zhao et al.* [1994]. The synthetics were compared with observations from the Hi-net array involving over 500 stations. The tomographic model reduces the cross-correlation traveltime residuals relative to a 1-D model by $\sim$ 50%. However, the waveforms are not well matched. A detailed slab model along a restricted 2-D corridor is constructed by a combination of forward modeling and a grid search. The model confirms that the average compressional-wave velocity inside the slab is about 4.5% higher than the ambient mantle, and that the 120-km-thick slab subducts with a dip angle near 24°. The slab sinks into the transition zone and flattens towards the west, with the compressional-wave velocity increasing by 3%. The 2-D model indicates there is an elongated low-velocity layer above the slab extending down to a depth about 300 km, with an S-wave velocity reduction of 14% compared to the normal mantle if the thickness

of the LVL is 20 km. However, the thickness of the LVL trades off to some extent with a low S-wave velocity in the LVL. A model with an LVL on top of the slab and a slow mantle wedge produces the observed strong secondary SH arrivals, which cannot be easily imaged with tomographic techniques.

We also note that the tomographic result depends on the initial slab structure. No tomographic study with an initial slab structure having an embedded LVL has been attempted. It is possible that adding a 20-km-thick LVL in the initial model of inversion can yield a strucuture equally consistent with the traveltime data used in the previous inversion studies. We did not include attenuation in the waveform modeling, which could have caused over-estimation of the thickness of $\delta \ln \alpha$; what we present here is the upper limit of these two parameters. In summary we believe that the question of how extensive the low-velocity layer is has not been resolved yet, and it would be an interesting future project to examine the broad-band waveform data for many more events in the way we did in this paper.

We interpret the LVL beneath NE Japan to be composed of hydrated mafic and/or ultramafic rocks: above a depth of 150 km, the LVL could be composed of hydrous mafic crust and serpentinized peridotite above and/or below the descending crust; below a depth of 150 km this hydrous layer could be more likely composed of serpentinized peridotite (or, at the greatest depths, phase A) above and/or below the fully eclogitized oceanic crust. Water released from the dehydration reactions in this hydrous zone could cause the abundant arc volcanism, the intermediate-depth intra-slab seismicity (70–300 km) [*Hacker et al.*, 2003b; *Ranero et al.*, 2005], and possible silent slip events, which have been observed in other subduction zones (e.g., Cascadia and the Tokai region in central Japan) [*Dragert et al.*, 2001; *Ozawa et al.*, 2002].

3.9 Addendum

The subduction zone beneath NE Japan is one of the coldest subduction regions (Figure 3.19a). The hydrous phases such as serpentinized peridotite, can be kept stable by the cold slab geotherms down to greater depths. The fully serpentinized phase A-chlorite serpentine (Figure 3.19b), can maintain $\sim$ 12 wt% H_2O down to a depth of 250 km, cor-

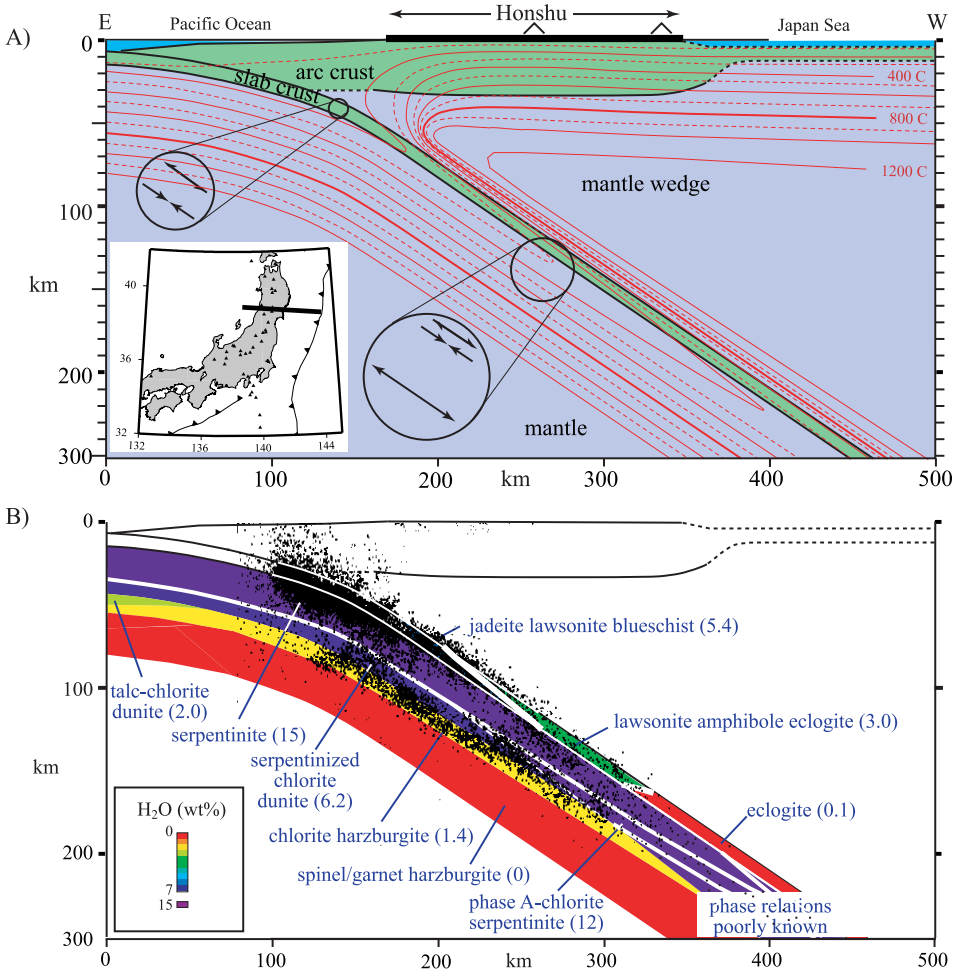

Figure 3.19: Correlation between seismicity and phase transformations in the Tohoku subduction zone (from *Hacker et al.* [2003b]).

responding to P = 5 GPa. The phase relations beyond 250 km are poorly know. Our observation of a LVL extending down to a depth of 300 km suggests the existence of stable hydrous phases at depths beyond 250 km.

The very negative seismic velocity anomalies inside the LVL indicates a high percentage of serpentinization. A significant amount of water is required for this process. There is a good correlation of the locations of the great outer rise earthquakes and the NE Japan region, where the strong LVL is observed (Figure 3.20). These earthquakes (*Peacock* [2001]) with deep rupture extent ($>$ 30 km), in addition to the faulting at the outer rise of the trench [*Ranero and Sallarès*, 2004; *Ranero et al.*, 2005], can provide a pathway for significant

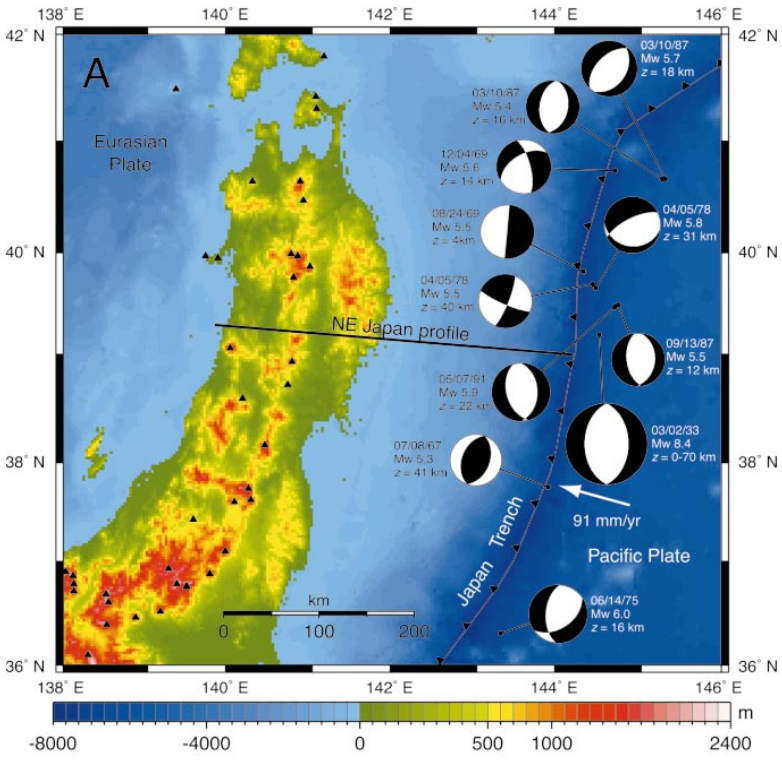

Figure 3.20: Geotectonic map of northeast Japan and focal mechanisms for selected outer rise earthquakes (from *Peacock* [2001]).

amount of 'water' infiltration periodically. For example, the 1933 Sanriku event in the outer rise region ruptured the entire lithosphere [*Kanamori*, 1971], and the 1977 Sambuwa event has a rupture depth extent of 30–50 km.

Chapter 4

3-D Adjoint Tomography of the Japan Subduction Zone

4.1 Abstract

In order to obtain better 3-D seismic velocity models of the Japan subduction zone and the neighboring region beneath Eastern China, we use adjoint tomography to iteratively minimize the misfit between the synthetics and data from Hi-net, F-net, and Global Seismographic Network (GSN) stations. We use *Zhao et al.* [1994]'s 3-D model embedded in the *Lebedev and Nolet* [2003] model as the initial model in the tomographic inversion. According to finite-frequency theory, the sensitive region along the ray path is given by a 3-D 'banana-doughnut' kernel, and the overall spatial distribution of the sum of all available event-station kernels determines the resolvable volume in the inversion. We select a total of 269 events with M_w between 4.5–8 to obtain maximum coverage of this region while avoiding redundancy. We processed the data and synthetics using two types of band-pass filters: 6–30 s for all the records and 24–120 s for F-net and GSN records. We apply an automated data-window selection algorithm in selecting measurement windows. The adjoint sources in these measurement windows are constructed based upon the frequency-dependent traveltime misfits between synthetics and data. Given the adjoint sources, we use the adjoint spectral-element method [*Tromp et al.*, 2005] to calculate banana-doughnut kernels for body waves and surface waves for the selected records. The weighted sums of the banana-doughnut kernels for all event-station pairs, with weights determined by the

traveltime measurements, can be used to construct misfit kernels, which are the gradients required in a non-linear conjugate gradient algorithm to further refine the existing 3-D model.

4.2 Introduction

Subduction zones play a very important role in plate tectonics. Many investigations of 3-D heterogeneity of the subduction zones have been carried out to understand the related dynamic and mineralogical processes: the slab dehydration process, melting in the mantle wedge and associated volcanic activities.

Amongst all the subduction zones on the Earth, the Japan subduction zone is the most extensively studied, with the aid of very dense station coverage and traveltime tomographic method [*Zhao et al.*, 1992, 1994; *Wang and Zhao*, 2005, 2006]. The low-velocity regions revealed tomographic images correlate with the locations of active volcanoes. However, the waveform modeling and receiver-function method observe there is a thin but strong low velocity layer (LVL) on top of the slab [*Chen et al.*, 2007; *Furumura and Kennett*, 2005; *Kawakatsu and Watada*, 2005], which is missing in the previous tomographic image inverted using traditional traveltime tomographic techniques. The LVL, associated with water transportation into the deep mantle [*Kawakatsu and Watada*, 2005], is essential for abundant arc volcanism, the intermediate-depth intra-slab seismicity (70–300 km) [*Hacker et al.*, 2003b; *Ranero et al.*, 2005], possible silent slip events [*Dragert et al.*, 2001; *Ozawa et al.*, 2002], and dynamically maintaining slab dip [*Manea and Gurnis*, 2007]. Mapping the 3-D distribution of the LVL may help us better understanding all the relative subduction zone processes. However, the traditional ray-based traveltime tomographic methodologies lack the robustness of recovering the amplitude of the velocity anomalies of seismic velocity structures, such as the LVL in subduction zones.

In recent years, finite-frequency tomographic techniques have been developed to better recover the sharp and small-scale seismic velocity structures inside the Earth [*Zhou et al.*, 2005; *Montelli et al.*, 2004; *Zhao et al.*, 2005; *Tromp et al.*, 2005]. In most of the studies, the 3-D sensitivity kernels are calculated based on 3-D initial model from traveltime

tomography, assuming the existing 3-D reference models are better initial models for tomographic inversion than 1-D reference models. The adjoint spectral-element method [*Tromp et al.*, 2005] especially facilitates calculating 3-D sensitivity kernels for seismograms with multiple phases.

In this study, we apply the adjoint spectral-element method to calculate the 3-D sensitivity kernels for a large number of station-event pairs. This work is on-going because of the computational overhead. The tomographic inversion will take several iteration to reach the final 3-D models. In this chapter we will present the initial 3-D models, the current dataset, the application of a window selection algorithm, the banana-doughnut kernels of the major phases, examples of event kernels, and finally the misfit kernels from a subset of events. The finite-frequency tomography using adjoint methods has been benchmarked in a synthetic inversion by *Tape et al.* [2007a]. In this study, we apply the same technique and extend it to 3-D case study of Japan subduction zone.

4.3 Model

In the previous chapter (Chapter 3), we showed that the regional 3-D P-wave model [*Zhao et al.*, 1994] typically explains about half of the traveltime anomalies and some of the waveform complexity. The goal of this chapter is to further minimize the misfit between the data and synthetics by refining the 3-D structure of the entire Japan subduction zone and the neighboring Eastern Asia area.

The lateral dimensions of the inversion domain are 44°(EW)×33°(NS) (108–152°E and 18–51°N). The initial model (Figure 4.1) is constructed using the Southeast Asia S-wave model of *Lebedev and Nolet* [2003] as the background model, with P-wave velocity anomalies added from a high-resolution Japan P-wave model [*Zhao and Hasegawa*, 1993; *Zhao et al.*, 1994] and S-wave velocity anomalies scaled to P by a factor of 1.5 [*Chen et al.*, 2007]. Two different crustal models are implemented in the spectral-element mesh: inside the region of the high-resolution model (32–45°N, 130–145°E, and down to 500 km), the crustal model is derived from the arrival times of local shallow earthquakes [*Zhao et al.*, 1992]; outside this region, the crustal model is CRUST2.0 [*Bassin et al.*, 2000] (Figure 4.2).

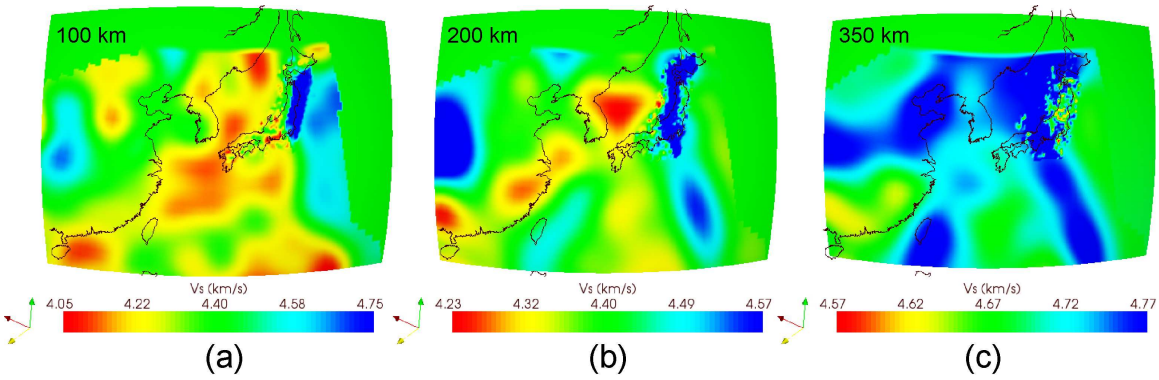

Figure 4.1: Map view of the spherical cross-sections of the initial S model plotted in Paraview, at depths of (a) 100 km, (b) 200 km, and (c) 350 km. A high-resolution Japan regional model, scaled from a P-wave model [*Zhao et al.*, 1994] with an optimal factor of 1.5 [*Chen et al.*, 2007], is embedded in a Southeast Asia S model [*Lebedev and Nolet*, 2003].

4.4 Data Selection

4.4.1 Raw Data

We collected data for more than 269 events with M_w 4.5–8 that occurred between 2000 and 2006. The source locations and focal mechanisms are the Harvard centroid-moment tensor (CMT) solutions. For each event, we use a maximum of 818 stations from three different networks (GSN, F-net, and Hi-net): 119 stations from GSN and F-net provide broadband records, whereas 699 Hi-net stations provide only high-frequency records (Figure 4.3).

4.4.2 Automated Data Selection

We use the one-chunk version of spectral-element code to calculate synthetic seismograms accurate at periods of $\sim$ 6 s and longer [*Chen et al.*, 2007], and processed the synthetics in two period ranges: 6–30 s for all the records, and 24–120 s for the broadband records only.

In this section, we apply a windowing algorithm (FLEXWIN) [*Maggi et al.*, 2008] to both data and synthetics for the 269 events in the Japan subduction zone. This algorithm first selects windows on the synthetic record containing a distinct energy arrival based on a

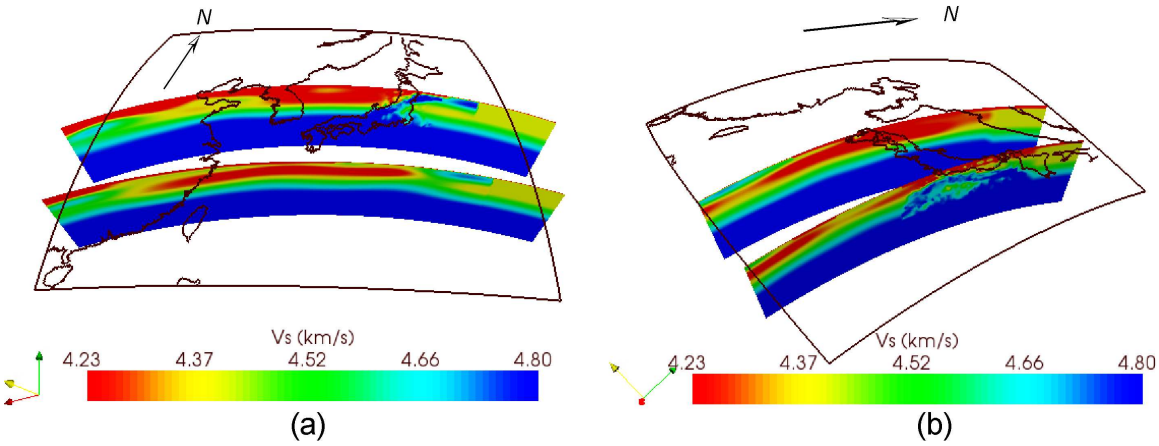

Figure 4.2: Vertical cross-sections of the initial S model at (a) latitudes of 30°N and 40°N and (b) longitudes of 130°E and 140°E. The bottom of the vertical cross-sections is at a depth of 700 km. Notice in the northern cross-section in (a), the subducting slab (blue colored high-velocity blob above the transition zone) beneath the central Japan.

short-term / long-term ratio (STA/LTA); it then rejects those windows in which the data and synthetics fail a set of quality criteria based on their cross-correlation, time-lag, amplitude ratio, and signal-to-noise ratio. The related parameters are explained in Table 4.1. For this study, the parameters are tuned and set in Table 4.2. Figures 4.4, 4.5, and 4.6 show windowing results for three events at different depths (Table 4.3): 051502B, 22.4 km deep, Taiwan; 091502B, 589.4 km deep, Northeastern China; 200511211536A, 155 km deep, Kyushu, Japan. We have tuned the windowing algorithm using different sets of parameters for the two period ranges (see Table 4.2). In the period range 24–120 s, the water level of short-term / long-term ratio is raised after the surface-wave arrivals to exclude the later arrivals that are not sensitive to upper mantle structure. In the period range 6–30 s, the water level is raised after the S-wave arrivals to exclude the surface waves, as the current crustal model is not detailed enough to predict the short-period surface waves. For the shallow event beneath Taiwan recorded at station ERM (Figure 4.4), the synthetics and data fits are poor in the short-period range (6–30 s), compared to the good fits in the long-period range (24–120s). For T = 6–30 s, the synthetics capture only the major P-wave arrival on the vertical component (Figure 4.4b), which is also the only arrival picked by the windowing algorithm. For T = 24–120 s, the observed and synthetic seismograms are similar in shape, and the algorithm picks not only the long-period P- and S-wave arrivals,

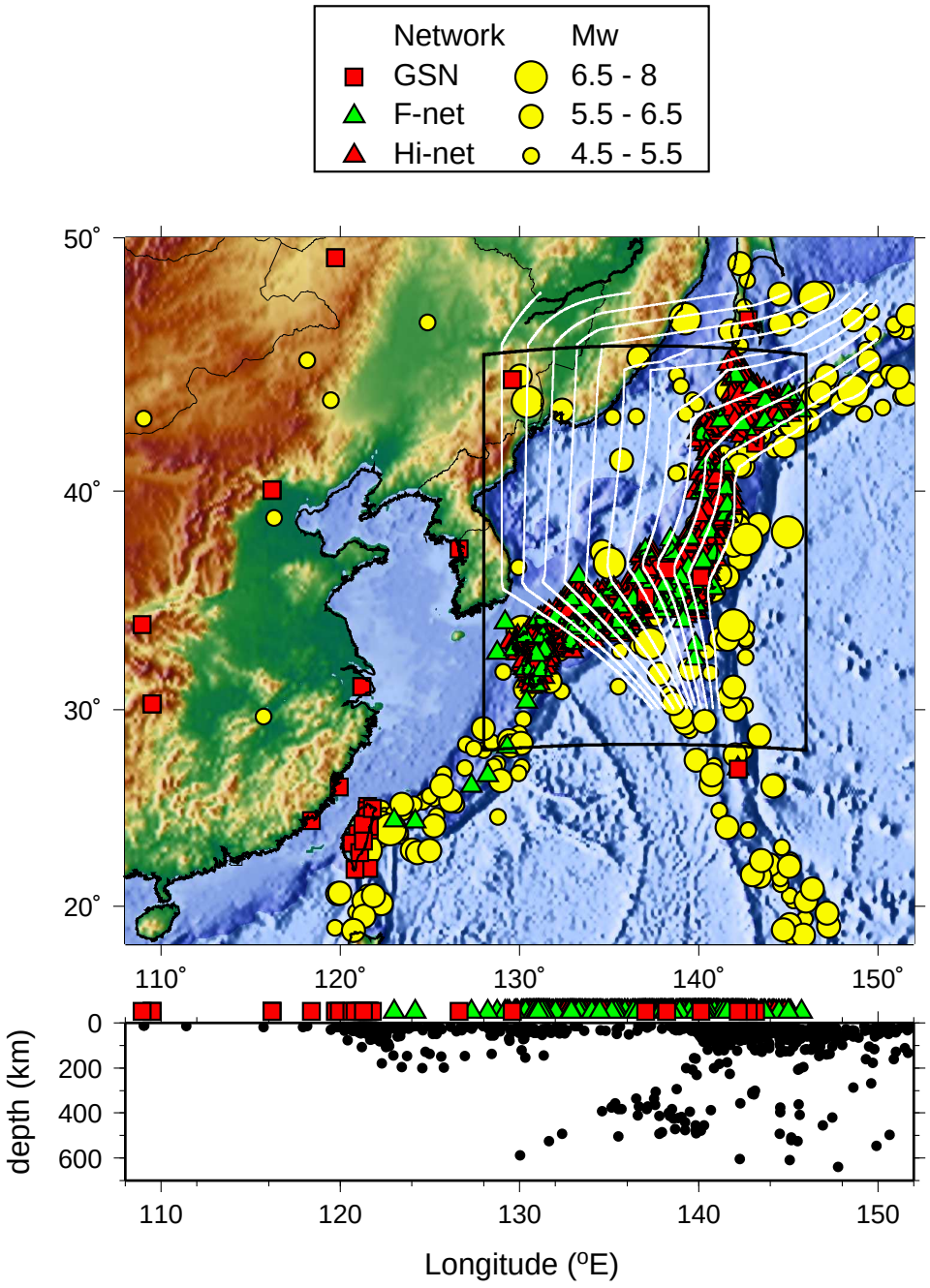

Figure 4.3: Map of the event and station distribution in the study area. More than 200 events with M_w from 4.5 to 8 that occurred between 2000 and 2006 are selected for tomographic inversion, indicated by the yellow circles. There are a total 818 stations from three different networks located in this area: GSN (red squares), F-net (green triangles), and Hi-net (red triangles), amongst which GSN and F-net provide broadband records, whereas Hi-net only provides high-frequency records. The bottom plot shows the distribution of all the events and stations projected onto a WE striking vertical plane. The region of the high-resolution Japan model is identified by the black box on the map. Inside the box, the white lines indicate the contours of the upper boundary of the Pacific plate with a 50 km contour interval.

Standard tuning parameters:			
$T_{0,1}$			bandpass filter corner periods
$r_{P,A}$			signal-to-noise ratios for whole waveform
$r_0(t)$			signal-to-noise ratios single windows
$w_E(t)$			water level on short-term:long-term ratio
$CC_0(t)$			acceptance level for normalized cross-correlation
$\Delta\tau_0(t)$			acceptance level for time lag
$\Delta \ln A_0(t)$			acceptance level for amplitude ratio
Fine tuning parameters:			
c_0			for rejection of internal minima
c_1			for rejection of short windows
c_2			for rejection of un-prominent windows
$c_{3a,b}$			for rejection of multiple distinct arrivals
$c_{4a,b}$			for curtailing of windows with emergent starts and/or codas
w_{CC}	w_{len}	w_{nwin}	for selection of best non-overlapping window combination

Table 4.1: Overview of standard tuning parameters, and of fine tuning parameters for a windowing algorithm (FLEXWIN), from *Maggi et al.* [2008]. Values are defined in a parameter file, and the time dependence of those that depend on time is described by user-defined functions.

$T_{0,1}$	24, 120	6, 30
$r_{P,A}$	3.5, 3.0	3.5, 3.0
r_0	1.5	3.0
w_E	0.12	0.12
CC_0	0.70	0.70
$\Delta\tau_0$	12.0	3.0
$\Delta \ln A_0$	1.0	1.0
c_0	0.7	0.7
c_1	3.0	3.0
c_2	0.0	1.0
$c_{3a,b}$	1.0, 2.0	1.0, 2.0
$c_{4a,b}$	3.0, 25.0	3.0, 12.0
$w_{CC}, w_{\text{len}}, w_{\text{nwin}}$	1, 1, 1	1, 1, 1

Table 4.2: Values of standard and fine-tuning parameters for Japan dataset in two period ranges: $T = 6 - 30$ s and $T = 24 - 120$ s.

Japan Events	Latitude	Longitude	Depth, km	M_w	Location
051502B	24.66	121.66	22.4	6.1	Taiwan
200511211536A	30.97	130.31	155.0	6.2	Kyuhu, Japan
091502B	44.77	130.04	589.4	6.3	Northeastern China
080202D	29.35	139.25	441.5	6.2	South of Honshu, Japan
083103C	43.38	132.37	493.0	6.1	Primor'ye, Russia
100301E	46.95	148.62	288.1	5.9	Northwest of Kuril Island
110704A	47.93	144.52	493.1	6.1	Sea of Okhotsk
200502221120A	33.15	137.16	372.2	5.6	Coast of Honshu, Japan
200510151551A	25.29	123.43	194.6	6.4	Northeast of Taiwan
200610091001A	20.66	119.85	15.0	6.3	Philippine Islands
111103C	22.39	143.48	107.1	5.8	Volcano Islands, Japan
102700B	26.31	140.69	387.6	6.0	Bonin Islands Region
011401A	22.19	143.93	112.5	5.8	Volcano Islands Region
061501B	18.94	147.25	17.0	5.9	Mariana Islands
070301F	21.66	142.99	307.7	6.4	Mariana Islands Region
021903D	44.19	141.73	226.6	5.8	Hokkaido, Japan Region
121404A	44.19	141.59	12.0	5.7	Hokkaido, Japan Region
200507230734A	35.57	140.29	61.9	5.9	Near the S. Coast of Honshu
120201B	39.49	141.09	123.7	6.4	Honshu, Japan
200602141527A	20.92	146.35	41.2	6.2	Mariana Islands Region
200609160222A	41.32	135.69	381.6	5.8	Sea of Japan

Table 4.3: Example events used in windowing measurement and event kernel calculation. For each event, the CMT catalog identifier, hypocentral location, and geographical location are given.

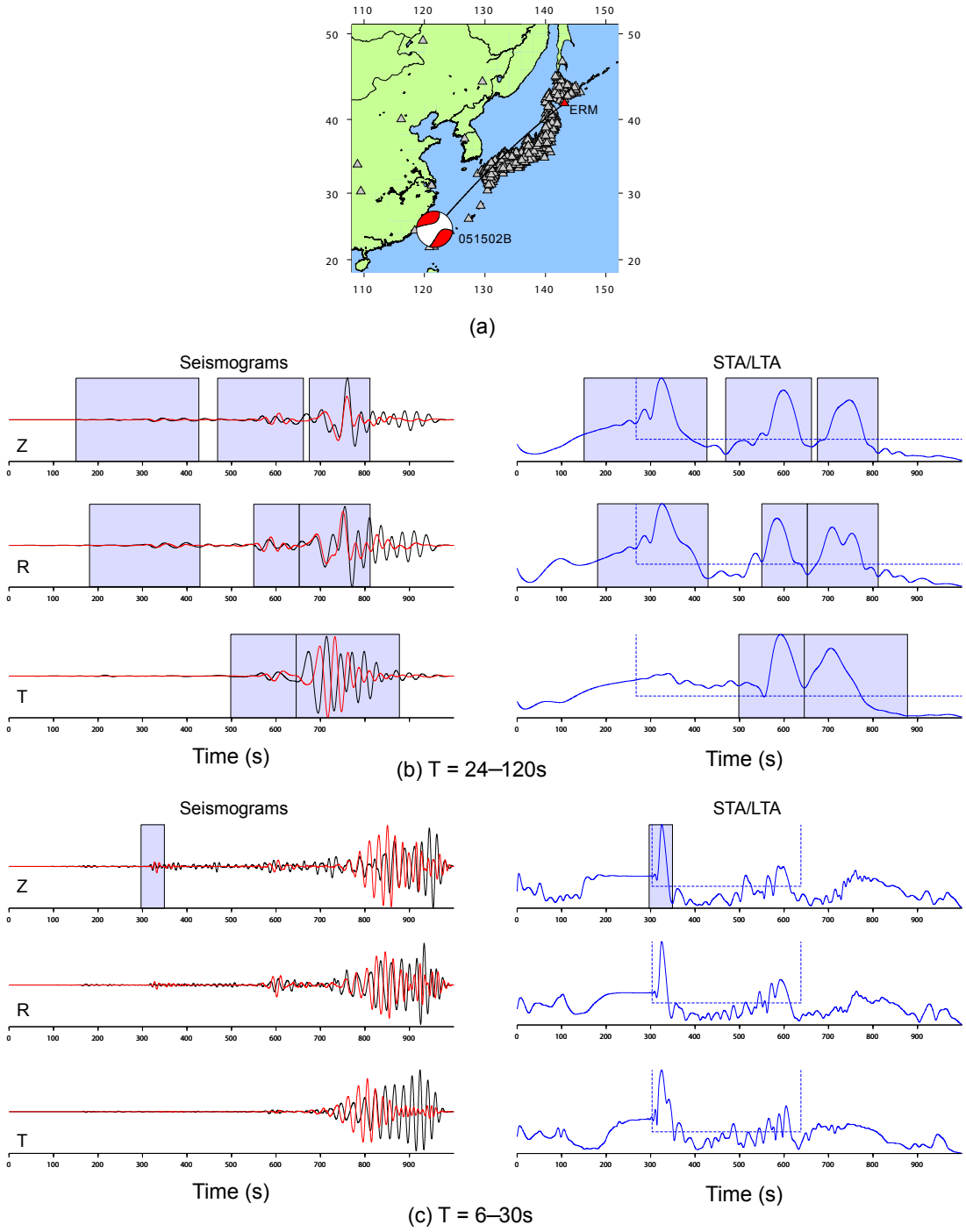

Figure 4.4: Window selection results for event 051502B from Table 4.3 recorded at station ERM (42.01°N, 143.16°E, $\Delta = 24.83°$). (a) Event and station map: event is 051502B indicated by the beach ball with the Harvard CMT focal mechanism, station ERM is marked as red triangles and all the other stations which recorded this event are marked by grey triangles. (b) Results for station ERM for the period range 6 s to 30 s. Vertical (Z), radial (R), and transverse (T) records of data (black, left column) and synthetics (red, left column), as well as the STA/LTA records (right column) used to produce the window picks. (c) Results for station ERM for the period range 24 s to 120 s.

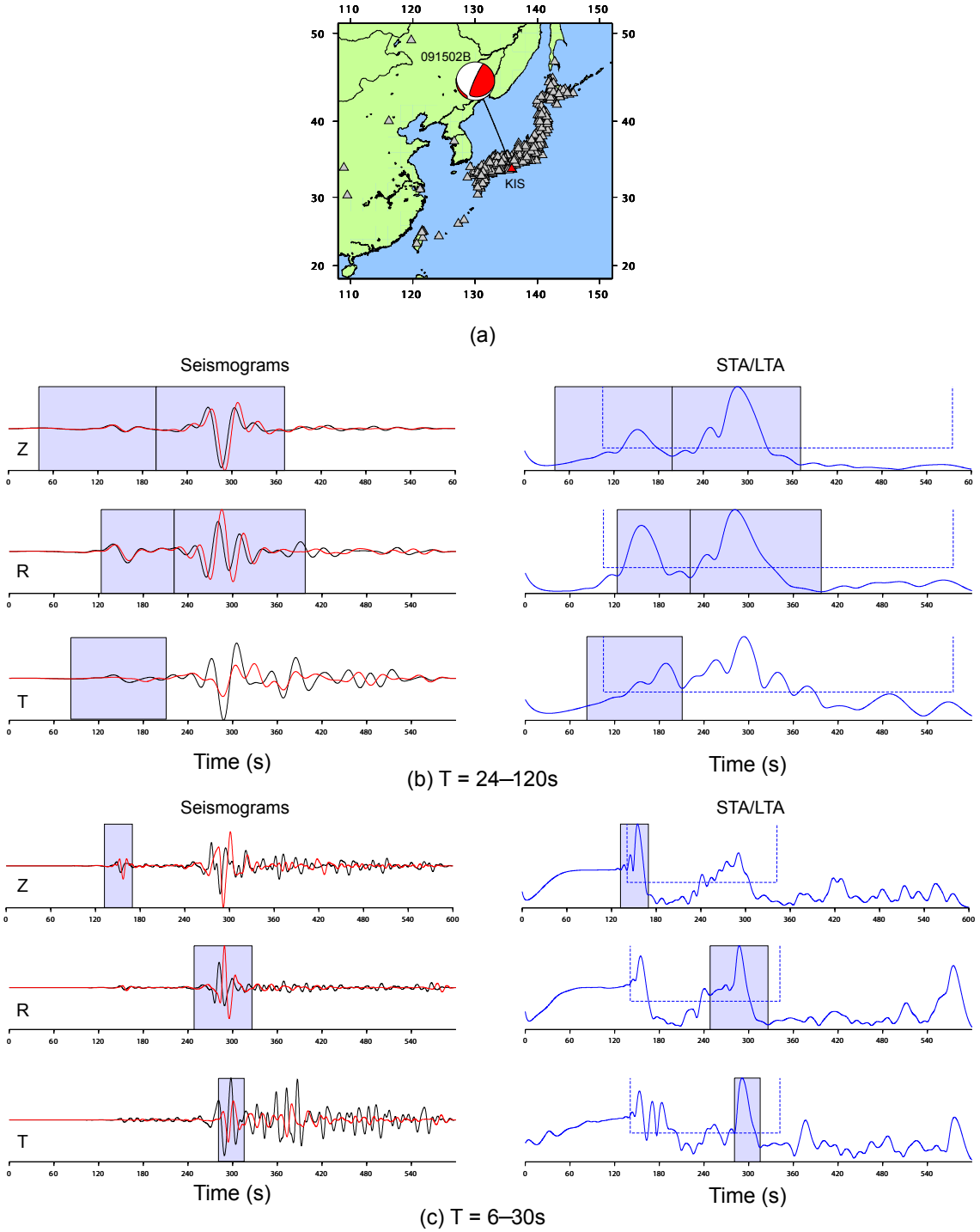

Figure 4.5: Window selection results for event 091502B from Table 4.3 recorded at station KIS (33.87°N, 135.89°E, $\Delta = 11.79°$). (a) Event and station map: event is 091502B indicated by the beach ball with the Harvard CMT focal mechanism, station KIS is marked as red triangles and all the other stations which recorded this event are marked by grey triangles. (b) Results for station KIS for the period range 6 s to 30 s. Vertical (Z), radial (R), and transverse (T) records of data (black, left column) and synthetics (red, left column), as well as the STA/LTA records (right column) used to produce the window picks. (c) Results for station KIS for the period range 24 s to 120 s.

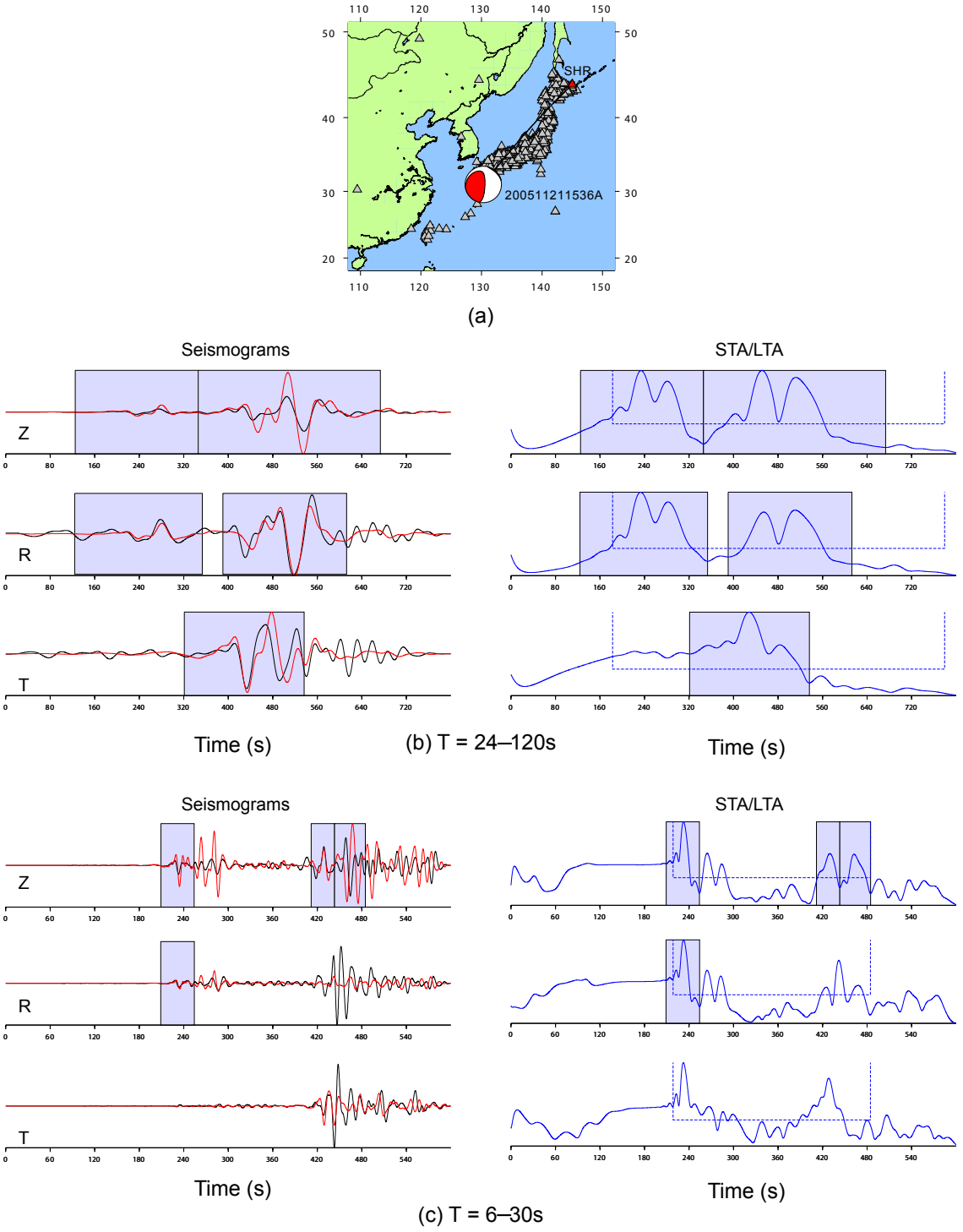

Figure 4.6: Window selection results for event 20051121536A from Table 4.3 recorded at station SHR (44.06°N, 144.99°E, $\Delta = 17.47°$). (a) Event and station map: event 20051121536A is indicated by the beach ball with the Harvard CMT focal mechanism, station SHR is marked as red triangles and all the other stations which recorded this event are marked by grey triangles. (b) Results for station SHR for the period range 6 s to 30 s. Vertical (Z), radial (R), and transverse (T) records of data (black, left column) and synthetics (red, left column), as well as the STA/LTA records (right column) used to produce the window picks. (c) Results for station SHR for the period range 24 s to 120 s. Note that corresponding high-frequency bandpass filtered version (b) has shorter record length (600 s).

but also the Rayleigh-wave on the vertical and radial components and the Love-wave on the transverse component (Figure 4.4c). As the depth sensitivity of surface waves is frequency dependent, long-period surface waves are sensitive to deeper velocity structure, the good fits at long periods (24–120 s) indicate that the starting model structure below the Moho is adequate for tomography.

Figure 4.5 shows an example of window picks for a deep event beneath Northeastern China (091502B) recorded at station KIS. Compared to the shallow event above, the seismograms from this event are very simple, and contain only two major body-wave arrivals (P and S). The windowing algorithm's similarity criterion clearly comes into play here, causing it not to pick the short-period S arrival on the vertical component (Figure 4.5b) as the distorted S-wave waveform of the data is quite different from the Gaussian shaped synthetics. The long-period S-wave arrival on the same component is selected due to higher data-synthetic waveform similarity (Figure 4.5c).

The records of the intermediate-depth event (200511211536A) recorded by station SHR (Figure 4.6) contain more seismic phases than the previous two examples. On the vertical component of the short-period seismogram (Figure 4.6b), the P-wave arrives at $\sim$ 230 s, immediately followed by pP and sPn, and the S-wave arrives at $\sim$ 420 s, followed by sS and PcP. The windowing algorithm selects separate windows for the P, S, and sS arrivals on the vertical component, and selects only the P arrival on the radial component. In the period range 24–120 s, the P and S waves merge with the arrivals that follow them, causing the windowing algorithm to select wavepackets instead of single phases: $P + pP + sPn$ and $S + sS + PcP$ on the vertical and radial components, and $S + sS$ on the transverse component. Note that the surface-wave signals of this intermediate-depth event are not as clearly defined as those of the shallow event (Figure 4.4).

Summary plots of window picks for event 200511211536A in the two period ranges T = 6–30 s and T = 24–120 s are shown in Figures Figures 4.7 and 4.8, respectively. On the short-period window record sections, the windows picked by the algorithm form two main branches that correspond to P and S arrivals. Sparse P arrivals are visible even on the transverse component (Figure 4.7g). The number and width of windows for each trace varies with epicentral distance. On the vertical and radial component window record sec-

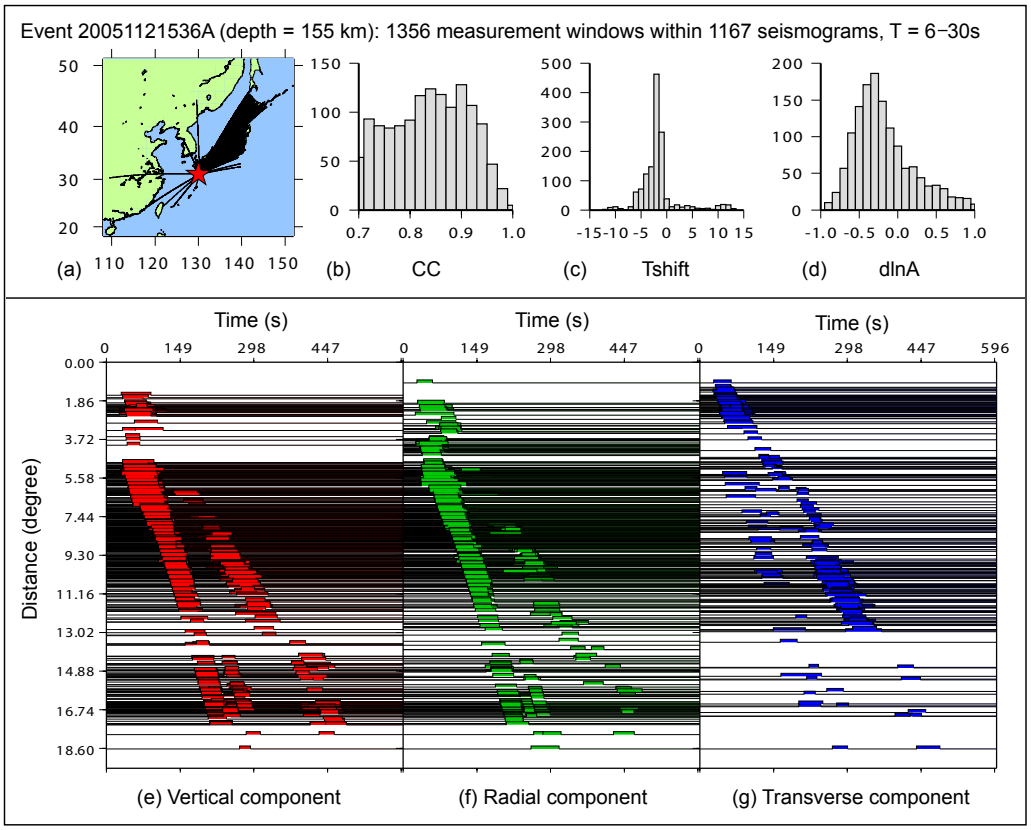

Figure 4.7: Summary plots of windowing results for event 200511211536A in Table 4.3, for the period range 6 s to 30 s. Same as Figure 4.8, only the windowing code has been run using a different set of parameters (Table 4.2), so that primarily only the body-wave arrivals are selected.

tions (Figure 4.7e,f), beyond the distance of 14° and after the P-arrival branch there are two small branches corresponding to pP and sPn, while after the S-arrival branch there is another branch corresponding to sS. The summary plot for the 24–120 s period range shows a single branch of windows on the vertical component that splits up into separate P- and S-wavepackets at distances greater than 15°. The same split is visible on the radial component, but occurs earlier (around 10°), while the transverse component windows form a single branch containing the merged $S + sS$ arrivals. Comparison of the histograms in Figures 4.7 and 4.8 shows that windows selected on the T = 24–120 s seismograms tend to have higher degrees of waveform similarity than those selected on the T = 6–30 s records. Timeshift $\Delta\tau$ values peak between -5 s to 0 s in both period ranges, indicating

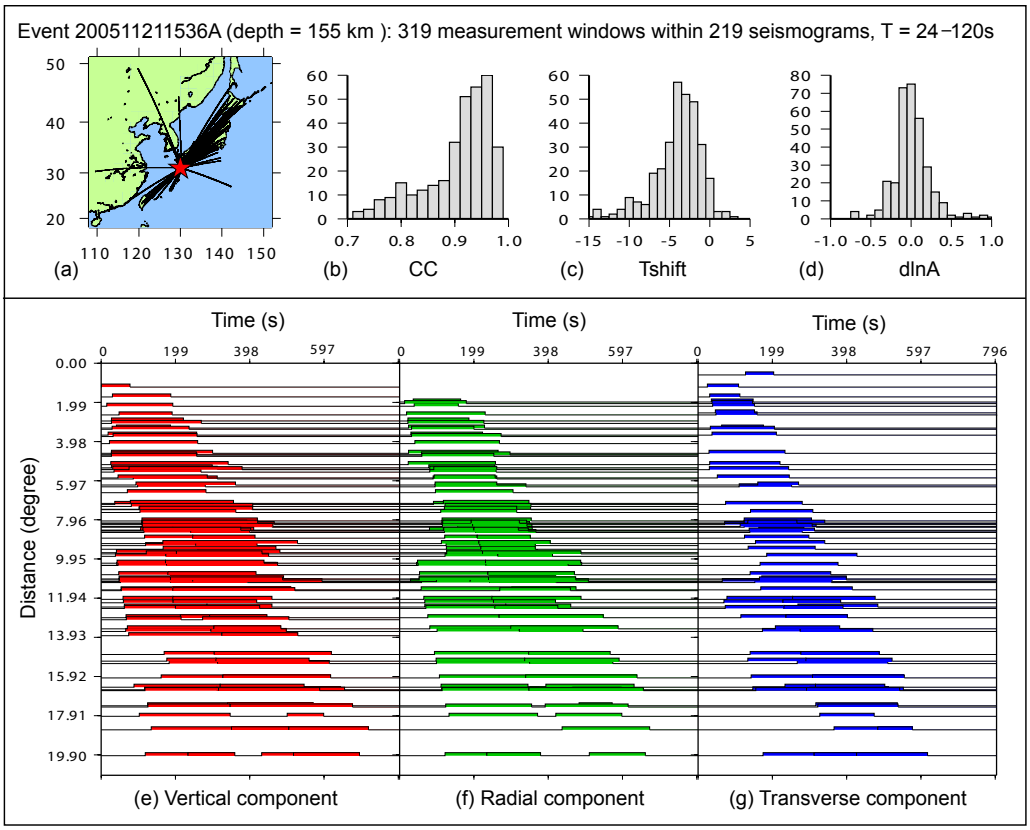

Figure 4.8: Summary plots of windowing results for event 200511211536A in Table 4.3, for the period range 24 s to 120 s. (a) Map showing paths to each station with at least one measurement window. (b)–(d) Histograms of number of windows as a function of normalized cross-correlation CC, time-lag τ, and amplitude ratio $\Delta \ln A$. (e)–(g) Record sections of selected windows for the vertical, radial, and transverse components.

that the synthetics are slower than the observed records. The particularly large peak at -2 s in the $\Delta\tau$ distribution of Figure 4.7c is probably due to the large number of Hi-net recordings that make up the short-period range records. The amplitude misfit $\Delta \ln A$ distribution peaks at $\Delta \ln A \simeq 0$ for T = 24–120 s (Figure 4.8d), indicating the amplitude of the synthetics matches the amplitude of the data at long periods. The peak at $\Delta \ln A \simeq -0.3$ in Figure 4.7d indicates that, on average, the synthetics overestimate the amplitude of the observed waveforms by 30% at short-periods. We cannot know at this stage if this anomaly is due to an overestimation short period energy in the source spectra of the events, or to an underestimation of the seismic attenuation.

Figure 4.9 show summary plots of the window picks statistics for the shallow (051502B), intermediate (200511211536A) and deep events (091502B) for the period range T = 6–30 s. Notice the very large numbers of measurement windows picked due to the over 600 Hi-net stations: 1243 windows for event 051502B, 1356 windows for event 200511211536A, and 1880 windows for event 091502B. Comparing the statistics for these three events, we see that the degree of similarity CC improves with increasing event depth, impling that the estimation of mantle structure is better than the estimation of crustal structure in the initial model. The $\Delta \ln A$ distributions of these three events have similar shapes, with peaks in the range of -0.5 to -0.3. However, the $\Delta\tau$ distributions have very different features: the shallow event (051502B) has a large peak at -10 s and another smaller peak at 8 s; the intermediate-depth event (200511211536A) has a very large peak at -2 s; the deep event (091502B) has a more distributed $\Delta\tau$ in the range -2 to -10 s. Possible explanations for these large average time lags include an origin time error, and/or an overestimation of the seismic velocity at the source location.

For our regional-scale tomographic study of the Japanese subduction zone, FLEXWIN is used to select measurement windows for a set of 269 events within the depth range 0–640 km. The histograms of the number of windows selected in both period ranges are shown in Figure 4.10. Notice that in the period range of 24–120 s, the majority of the events (233) fall into the bracket with 50–350 measurement windows selected, and in the period range of 6–30 s, most events have number of measurement windows less than 900. The set of 57 events with less than 100 measurement windows in period range of 6–30 s

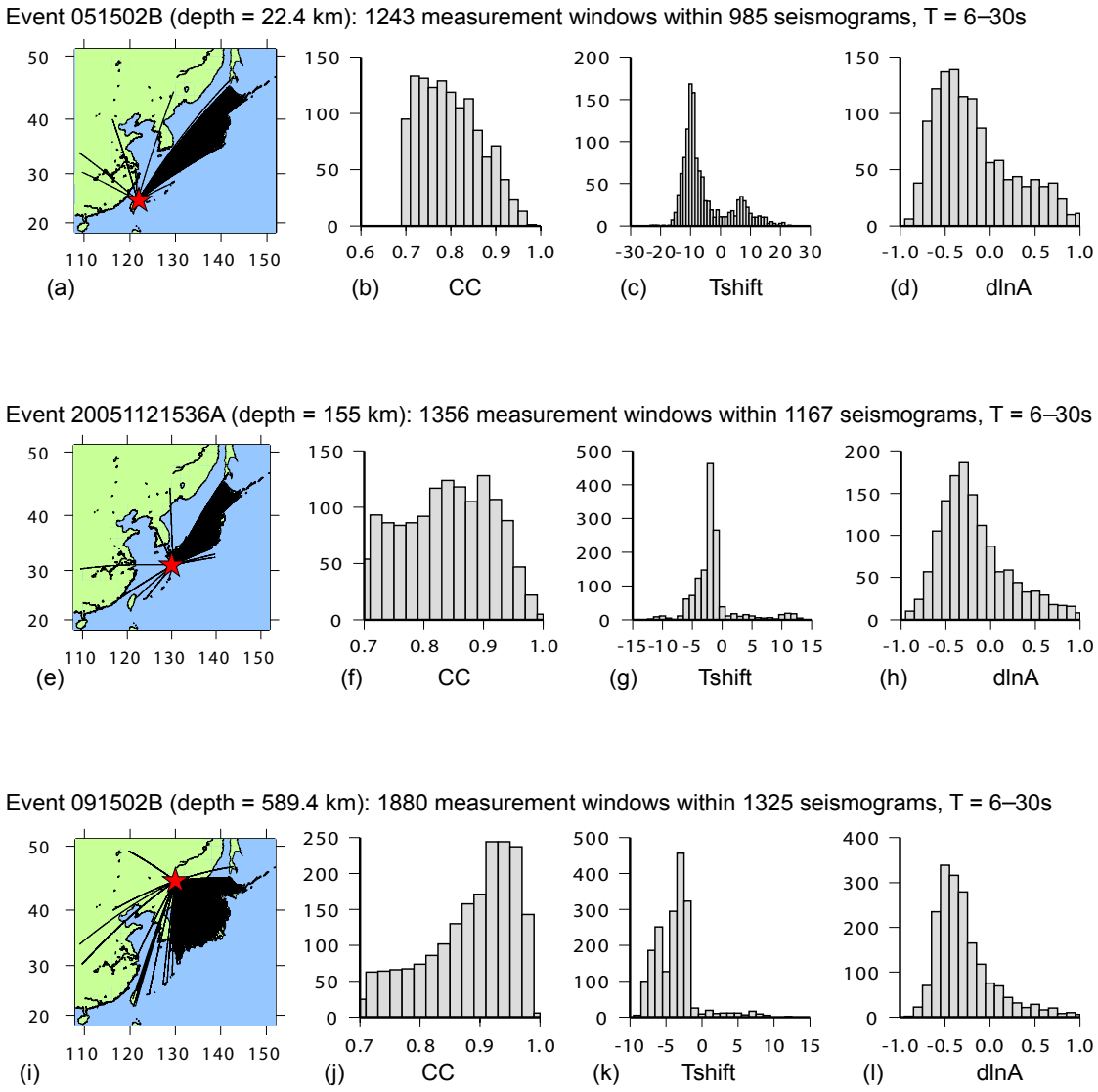

Figure 4.9: Summary statistics of windowing results for events 051502B, 200511211536A, and 091502B in Table 4.3, for the period range 6 s to 30 s.

mostly consists of shallow events (depth $<$ 100 km), the few window selections indicate that the shallow velocity structures in the initial model are not detailed enough to explain the short-period data. We select a subset of 206 events with more than 50 measurement windows in T = 24–120 s and more than 100 in T = 24–120 s in order to exclude the events with noisy data quality or bad source location, origin time, or source mechanism. For these 206 events, the FLEXWIN selected 44,709 windows in T = 24–120 s and 119,376 windows in T = 6–30 s. These windows, which capture the body-wave and surface-wave phases, can be fed into the code of measuring the frequency-dependent traveltime misfit, using either the cross-correlation or the multitaper measurement method [*Hjörleifsdóttir*, 2007].

Figure 4.11 shows the histogram of traveltime misfits (timeshifts) for 119,376 measurements of the selected 206 events in T = 6–30 s. Timeshift $\Delta\tau$ distributions have values peak at -2 seconds, slightly biased towards the negative side. This indicates the initial model is overall slower than the real model. The first few iterations of the inversion will be required to adjust these biased timeshift distributions. The timeshift distributions with epicentral distances are scattered (Figure 4.12). There is clearly a linear increasing of the upper bound of absolute timeshifts with increasing of distances, due to the constrains in window selection algorithm. However at each distance, timeshifts span the whole range of values from the most negative to the most positive, which is caused by the mixing of measurements for different body-wave phases, or the same body-wave phase sampling different 3-D structures.

4.5 3-D Sensitivity Kernels

In finite-frequency traveltime tomography, the traveltime adjoint sources are generated by time-reversing only the predicted ground velocity at each component, which means that the traveltime adjoint field does not depend on the data [*Tromp et al.*, 2005]. The sensitivity kernels generated by the interaction between the forward wavefield and the traveltime adjoint field are called ‘banana-doughnut’ kernels.

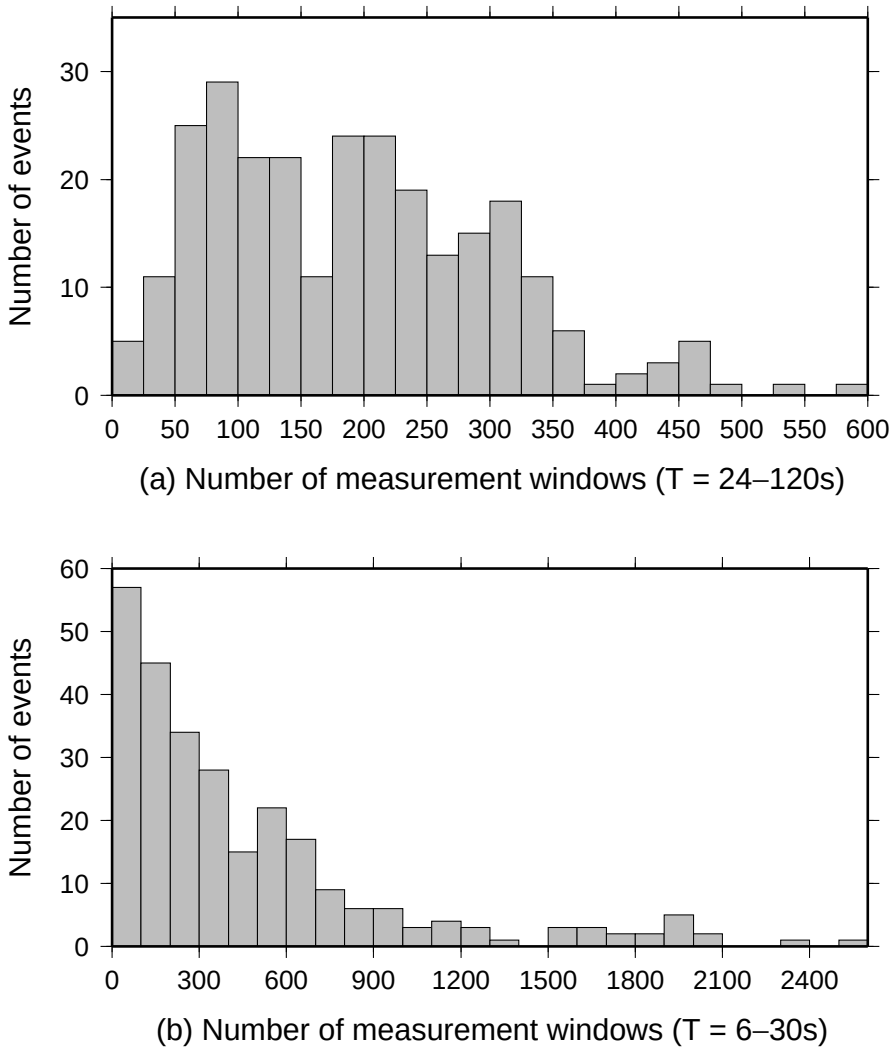

Figure 4.10: Summary statistics of number of measurement windows for all 269 events in the period range of (a) 24–120 s and (b) 6–30 s.

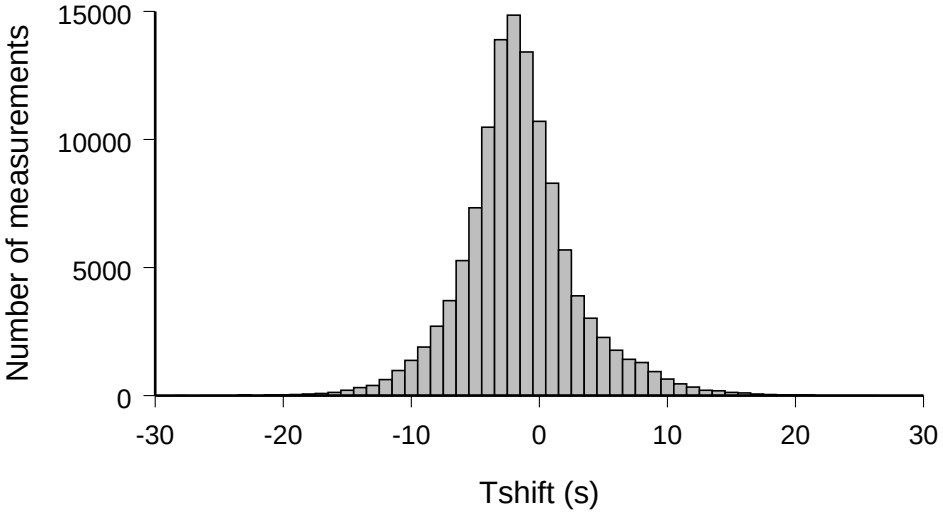

Figure 4.11: Summary statistics of timeshifts for the measurements of the selected 206 events in the period range of 6–30 s.

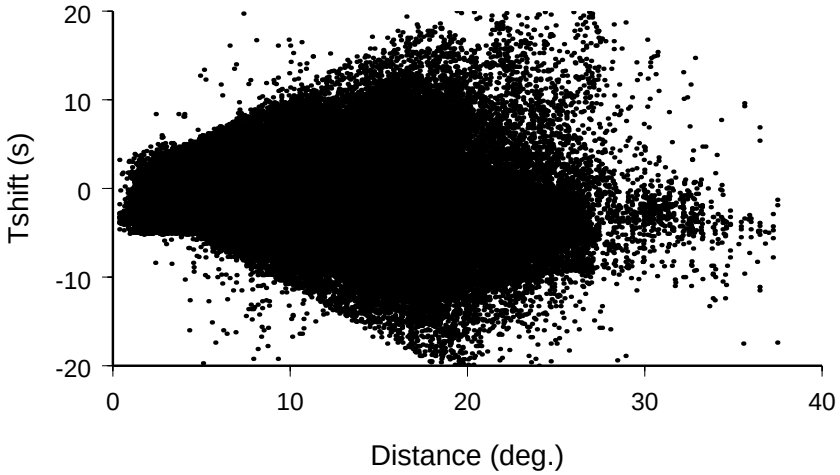

Figure 4.12: Timeshifts plotted as a function of epicentral distance for the selected 206 events in the period range of 6–30 s.

4.5.1 3-D 'Banana-Doughnut' Kernels of the Major Phases

In the region of the Japan subduction zone, due to different event-station geometries, there are many phases observed in the data and also predicted by the 3-D synthetics. In summary, the major phases consist of P, S, pP, sP, sS, Sn, Pn, Love, and Rayleigh waves.

For an intermediate depth event (200609160222A, depth = 318.6 km), Figure 4.13a shows the P and S waveforms are well predicted by the synthetic record at a close epicentral distance (station HRO, $\Delta = 5.74°$). With traveltime adjoint sources created from the highlighted windows, we calculated the banana-doughnut kernels for P (Figure 4.13b) and S waves (Figure 4.13c). The P-wave kernel for compressional-wave velocity (α) shows a typical banana-doughnut shape, hollow in the middle. The P-wave kernel for shear-wave velocity (β) is almost zero, which demonstrates again the P wave is not sensitive to shear-wave velocity perturbation. The S-wave kernels are more complicated: α kernel of the S-wavepacket has a leg with sensitivity to α, indicating S to P conversion as well; β kernel of S has two branches, one is a typical banana-doughnut shaped direct-S sensitivity branch and the other shows strong upgoing sensitivity but weaker sensitivity after being reflected at the surface, which also indicates S to P conversion. Therefore, the S-wave packet on the vertical component actually has two phases arriving together, the down-swing S phase followed by the up-swing sP phase. The banana-doughnut kernels show an alternative way to recognize seismic phases on the seismograms. For the same event (200609160222A), we also calculate the 3-D synthetics for a station with larger epicentral distance (station XAN, $\Delta = 22°$). More phases show up on the vertical component of both data and synthetics (Figure 4.14a). Figure 4.14b shows P is reflected at the bottom of transition zone (660 km), while Figure 4.14c displays pP bounced at the surface. In this event-station configuration, the sP wave arrives much earlier than the S wave. The sP banana-doughnut kernels (Figure 4.14(d,e)) have sensitivity patterns similar to the sP branch in Figure 4.13c. Two major phases, S and sS, arrive on the tangential component (Figure 4.15), and the sensitivity patterns are very similar to P and pP kernels in Figure 4.14(b,c), except with more sensitivity branches sampling different regions of the model, which explains why the S and sS waveforms are more complicated.

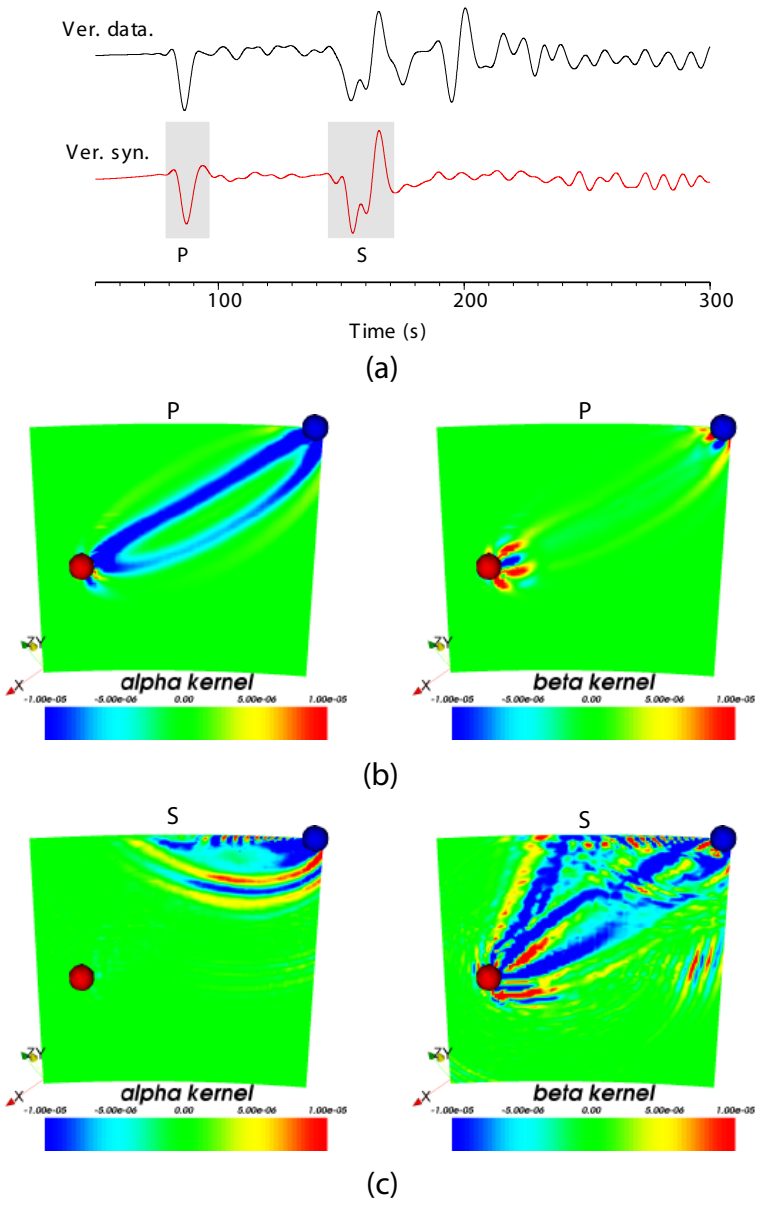

Figure 4.13: Data and 3-D synthetics comparison for the vertical component record of station HRO and the corresponding P- and S-wave banana-doughnut kernels. (a) Data (black) and synthetics (red) are bandpass filtered between 6–150 s, and vertical cross-sections of (b) P- and (c) S-wave banana-doughnut kernels for station HRO ($\Delta = 5.74°$) and event 200609160222A (depth = 318.6 km),are calculated by using the adjoint sources constructed from the highlighted grey windows in (a).

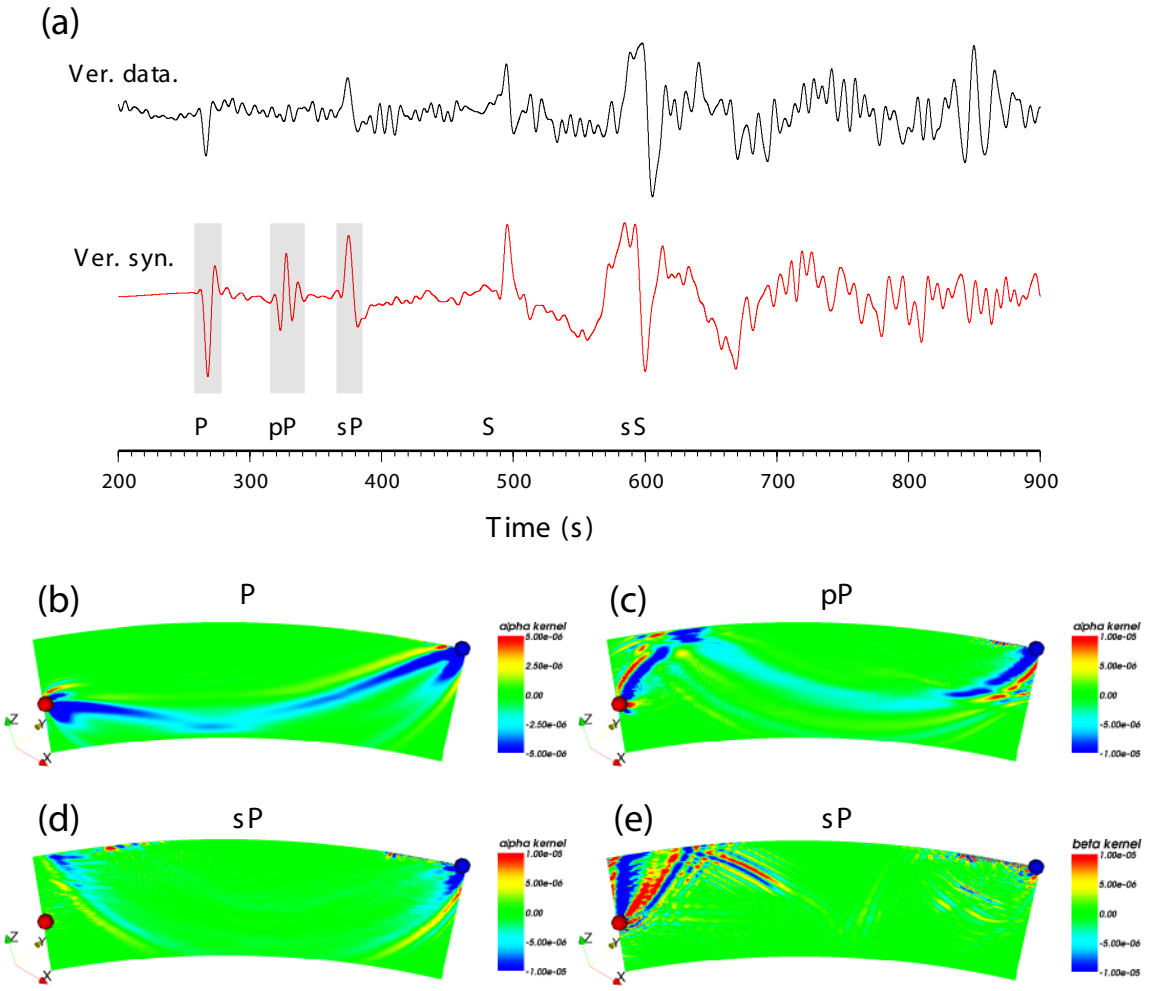

Figure 4.14: Data and 3-D synthetics comparison for the vertical component record of station XAN and the corresponding P-, pP- and sP-wave banana-doughnut kernels. (a) Data (black) and synthetics (red) are bandpass filtered between 6–150 s, and vertical cross-sections of (b) P-wave α kernel, (c) pP-wave α kernel, (d) sP-wave α kernel, and (e) sP-wave β kernel for station XAN ($\Delta = 22°$) and event 200609160222A (depth = 318.6 km), are calculated by using the adjoint sources constructed from the highlighted grey windows in (a).

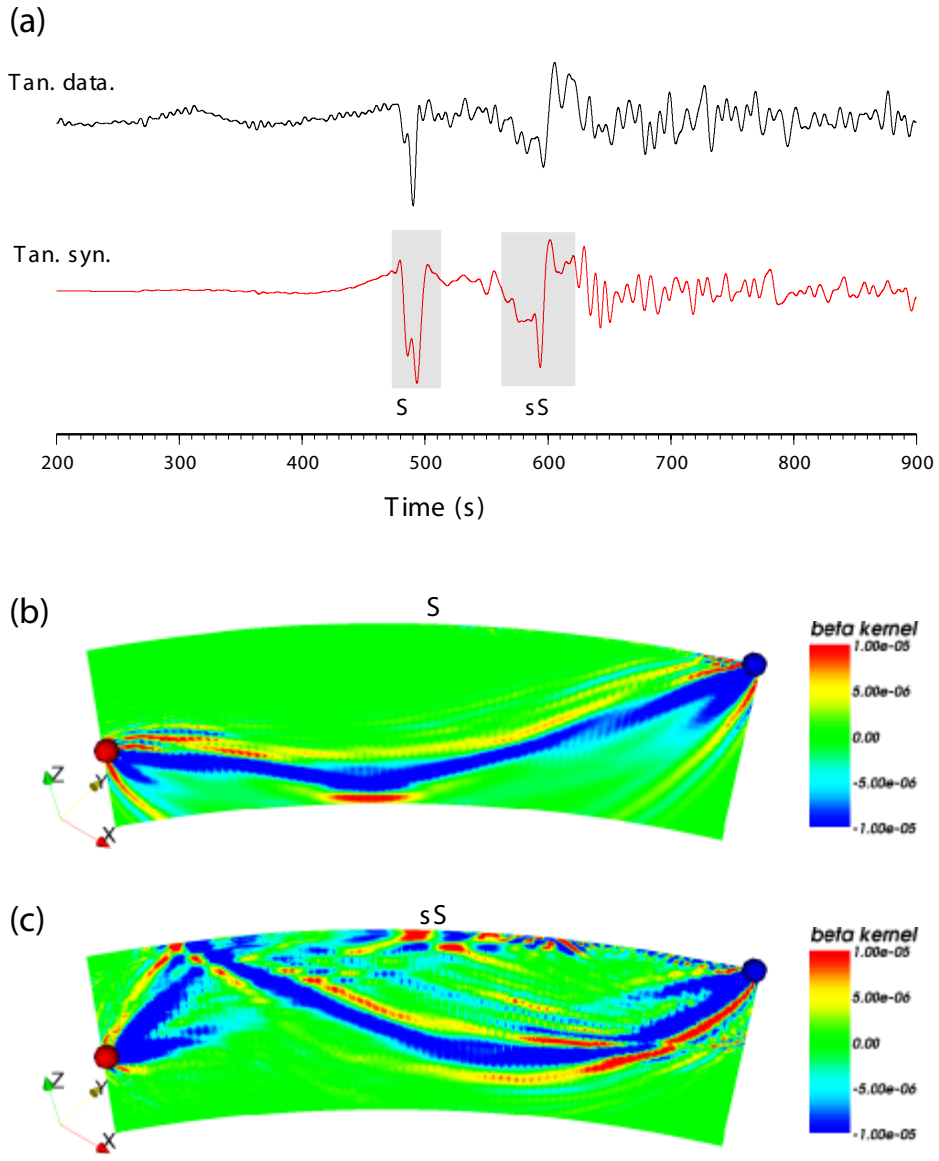

Figure 4.15: Data and 3-D synthetics comparison for the tangential component record of station XAN and the corresponding S- and sS-wave banana-doughnut kernels. (a) Data (black) and synthetics (red) are bandpass filtered between 6–150 s, and vertical cross-sections of (b) S-wave β kernel and (c) sS-wave β kernel for station XAN ($\Delta = 22°$) and event 200609160222A (depth = 318.6 km), are calculated by using the adjoint sources constructed from the highlighted grey windows in (a).

Finally, we investigate the phases and the corresponding kernels at station HIA ($\Delta = 8.6°$) for a very shallow event (event 091603D, depth = 15 km). Figure 4.16 shows nice fits between the data and the synthetics in the period range of 12–150 s. On the vertical records, there are weak Pn and Sn phases, followed by a very strong Rayleigh-wave arrival, while on the tangential records, the Love-wave arrival is dominant. Figure 4.17 exhibits that Pn wave has sensitive to α and β close to the surface, and it also has a strong sensitivity to α in the depth range of 100–300 km; Sn wave has sensitivity only to β close to the surface in the upper 200 km. The sensitivity regions of Rayleigh- and Love-wave are shown in Figure 4.18. The horizontal cross-sections are at a depth of 15 km. Surface waves have sensitivity close to the surfaces. Rayleigh wave is sensitivity to both α and β, and the sensitivity to β is relatively much stronger. Love wave is only sensitive to β, the asymmetric shape of the kernel might be caused by the radiation pattern or 3-D heterogeneity.

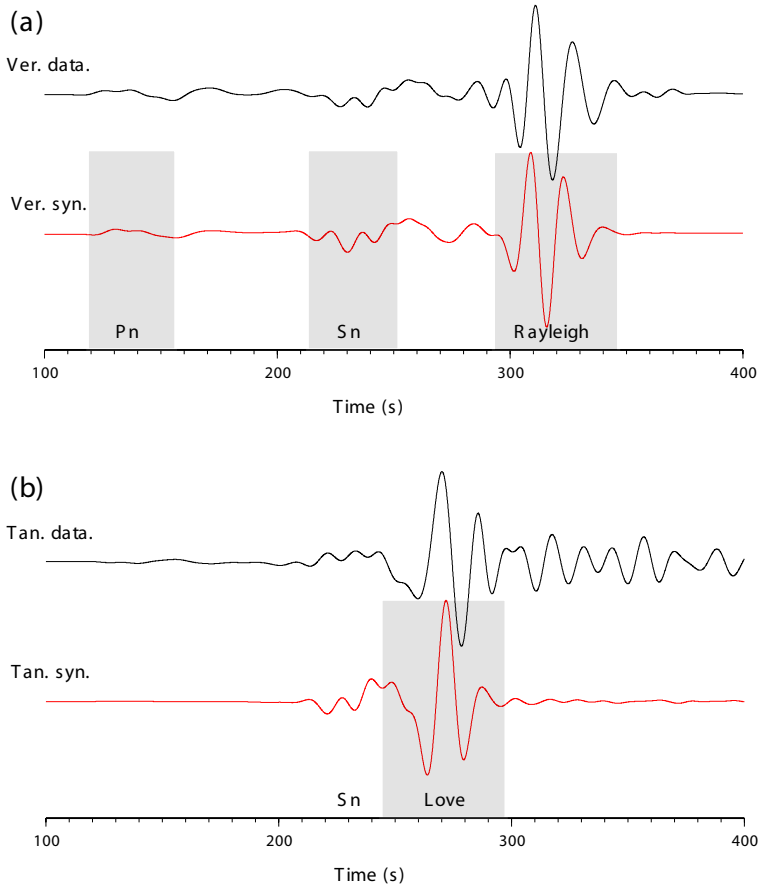

Figure 4.16: Data and 3-D synthetics comparison for the (a) vertical and (b) tangential component records of station HIA ($\Delta = 8.6°$) and event 091603D (depth = 15 km).

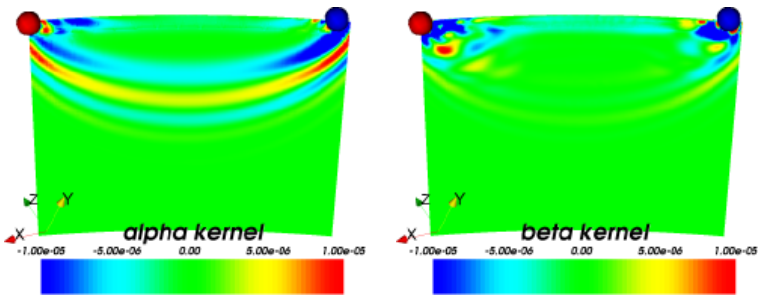

(a) Pn

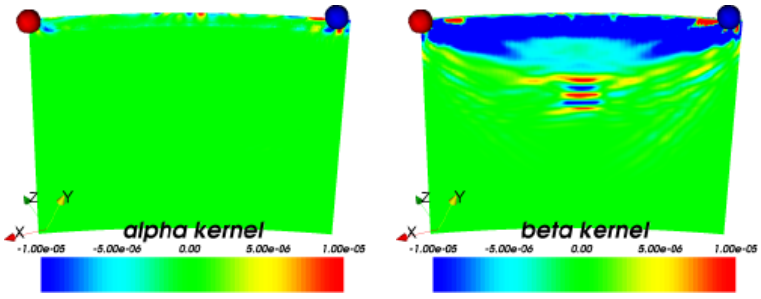

(b) Sn

Figure 4.17: Vertical cross-sections of (a) Pn-wave and (b) Sn-wave α and β kernel for station HIA and event 091603D (depth = 15 km). The kernels are calculated using the adjoint sources constructed from the highlighted grey windows in Figure 4.16.

All the major phases discussed above provide very important traveltime information and sensitivity coverage of the 3D volume of the model.

By summing up all the P-wave α kernels between a deep event (091502B) and all the stations (> 600) from the Hi-net array, Figure 4.19 shows the total volume of the sensitivity region, which is near the slab upper interface. Figure 4.20 shows the volumetric sensitivity region for a shallow event (091603D) and all the stations from the F-net and GSN stations. For this shallow event, the sensitivity region covers the transition zone.

4.5.2 Event Kernels

The 3-D 'banana-doughnut' kernels calculated using the traveltime adjoint sources do not depend on the data, but in the inversion process, we need to use the 3-D 'banana-doughnut' kernels weighted by the traveltime misfit measurements. So the adjoint sources used in the end are actually *combined traveltime adjoint sources* defined by *Tromp et al.* [2005].

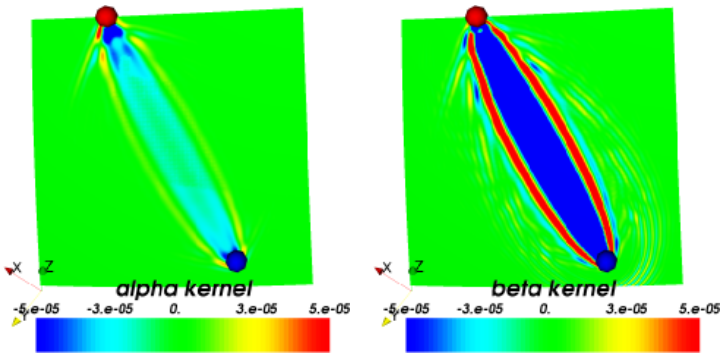

(a) Rayleigh

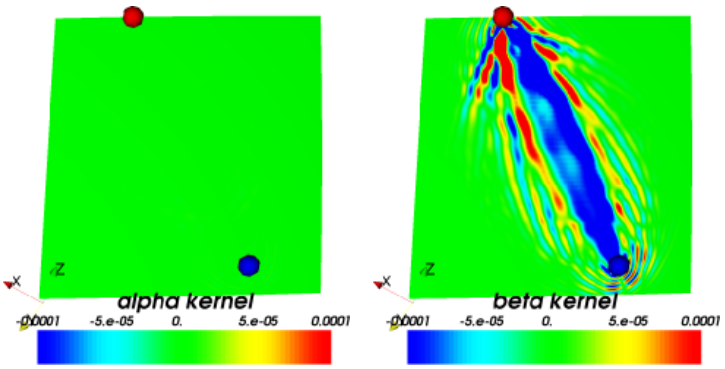

(b) Love

Figure 4.18: Horizontal cross-sections of (a) Rayleigh-wave and (b) Love-wave α and β kernel for station HIA and event 091603D (depth = 15 km). The kernels are calculated using the adjoint sources constructed from the highlighted grey windows in Figure 4.16.

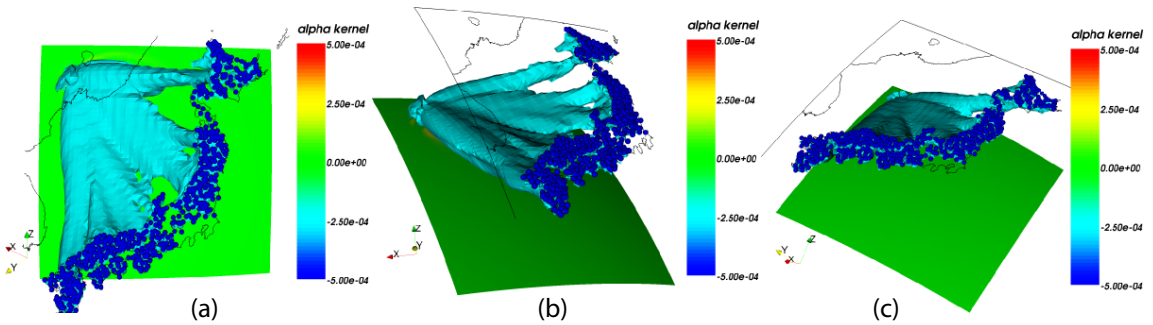

Figure 4.19: Isosurface of 3-D banana-doughnut α kernel of event 091502B (depth = 589.4 km) from vertical P waves. Blue circles indicate Hi-net stations. The green layer is the spherical surface at a depth of 660 km. (a) Map view. (b) Side view from the south-west. (c) Side view from the south-east.

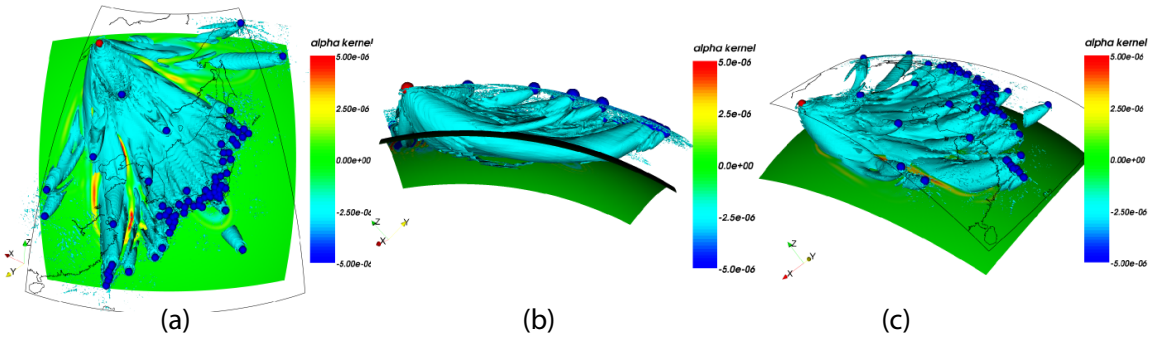

Figure 4.20: Isosurface of 3-D banana-doughnut α kernel of event 091603D (depth = 15 km) from vertical P waves. Blue circles indicate F-net and GSN stations. The event location is marked by a red circle. The green layer is the spherical surface at a depth of 660 km. (a) Map view. (b) Side view from the west. (c) Side view from the south-west.

Figure 4.21 shows examples of adjoint sources on three components at station KIS, which recorded event 091502B (Table 4.3). In the period range of 6–30 s, the adjoint sources are calculated using cross-correlation measurements of traveltime misfits in the selected body-wave windows (Section 4.4.2, Figure 4.5b). In the period range of 24–120 s, the adjoint sources are calculated using both cross-correlation and mutitaper measurements of travel-time misfits in the selected long-period body-wave windows (Section 4.4.2, Figure 4.5c). Cross-correlation and mutitaper measurements yield almost the same adjoint sources, except the multitaper adjoint sources tend to have smaller amplitude. In the following event kernel calculations, we use the adjoint sources summed from both period ranges for all the stations. And we chose the multitaper adjoint sources whenever it meets the criteria to make the multitaper measurements.

With the combined adjoint sources ready, we calculated the event kernels generated from all the non-zero combined adjoint sources, which contain the information of travel-time misfits. Figure 4.22 shows the event kernels of shear-wave velocity β for three events at different depths (Table 4.3): 051502B, 22.4 km deep; 200511211536A, 155 km deep; 091502B, 589.4 km deep. Figure 4.23 shows the event kernels of compressional-wave velocity α for these three events. The main sensitivity region of each event has a very different shape and amplitude. Event 051502B has the main sensitivity region beneath Ryukyu Islands and East China Sea (Figure 4.22a and Figure 4.23a); event 200511211536A has the sensitivity region beneath Japan Islands (Figure 4.22b and Figure 4.23b); event 091502B

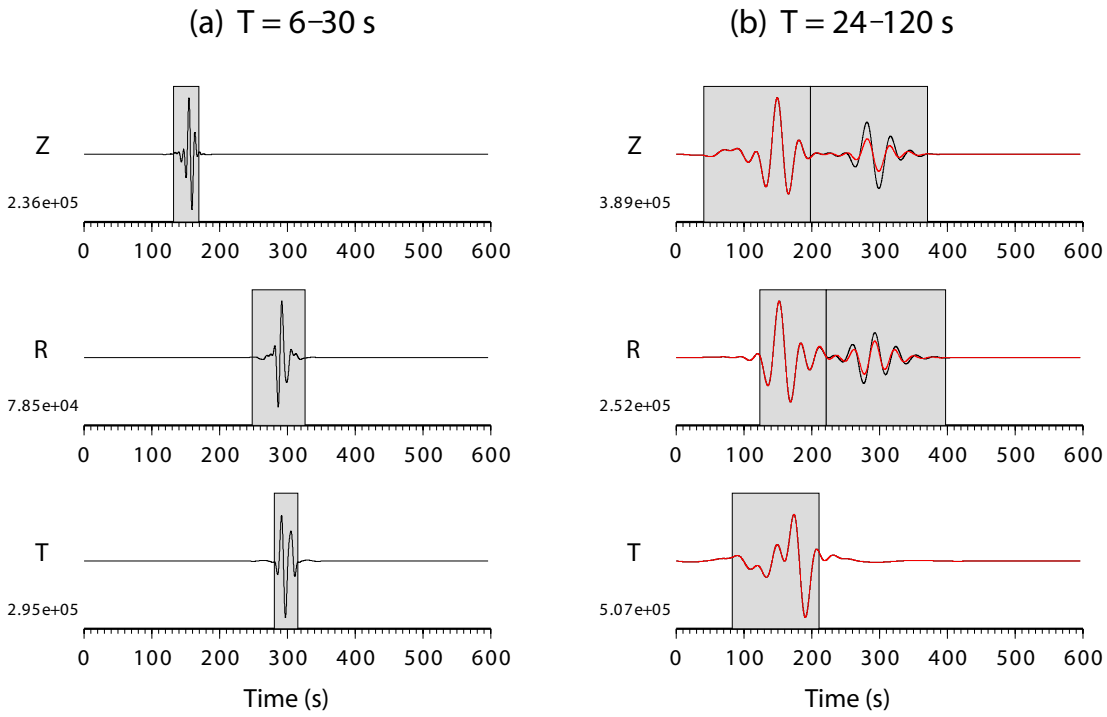

Figure 4.21: The three-component adjoint sources calculated in the period ranges of (a) 24–120 s and (b) 6–30 s for event 091502B from Table 4.3 recorded at station KIS ($33.87°$N, $135.89°$E, $\Delta = 11.79°$). The highlighted windows are the same as those in Figure 4.5 selected by the windowing algorithm (FLEXWIN). The black traces are the adjoint sources from the measurements by cross-correlation method, and the red traces indicate the adjoint sources from the measurements by multitaper method.

has the sensitivity mostly beneath Sea of Japan (Figure 4.22c and Figure 4.23c). The intermediate depth event has very weak sensitivity at the depth of 350 km (Figure 4.22b and Figure 4.23b), while both the deep and the shallow event have much stronger sensitivity (Figure 4.22a,c and Figure 4.23a,c). The sign of the gradient could also change at different depth for the same event, for example, the event kernel (Figure 4.23b) changing from negative at a depth of 100 km to positive at a depth of 200 km. Notice that, due to the large number of Hi-net stations, the shape of the sensitivity region is also controlled by the sensitivity between the event and the Hi-net stations. The event kernels show very different details due to each specific event-receiver configuration.

4.5.3 Misfit Kernels

We calculated the event kernel by simultaneously propagating back the time-reversed adjoint source signals at all the available receivers for each individual event. Figure 4.24 shows the spatial distributions of 21 sample events. The misfit kernels are then constructed by summing up these 21 event kernels. the result is not conclusive at this stage. However, if we assume these events well sample the model region and represent the whole dataset, we can have some preliminary results from the misfit kernel plots. Overall, the blue colors (negative gradients) indicate the seismic velocities in these regions need to be faster than in the initial model, while the red colors suggest the opposite. The large-scale pattern in Figure 4.25 and Figure 4.26 shows that shear-wave velocities (β) beneath the Sea of Japan, Japan Islands, and Bonin Islands should be faster than in the initial model, but β beneath Ryukyu Islands and East China Sea should be slower; the overall compressional-wave velocities (α) should be faster than the α in the initial model, except part of the region beneath Bonin Islands at a depth of 350 km. As the blue colors in Figure 4.25 and Figure 4.26 correlate well with the blue regions in Figure 4.1, where the fast slab anomalies locate, the negative gradients indicate the seismic velocities of slab need to be faster to minimize the data-synthetics misfit. There are some small-scale red patches (positive gradients) inside the blue regions (Figure 4.25 and Figure 4.26), which require slower seismic velocities. These red patches might relate to mantle wedge melts and the low velocity layer on top of

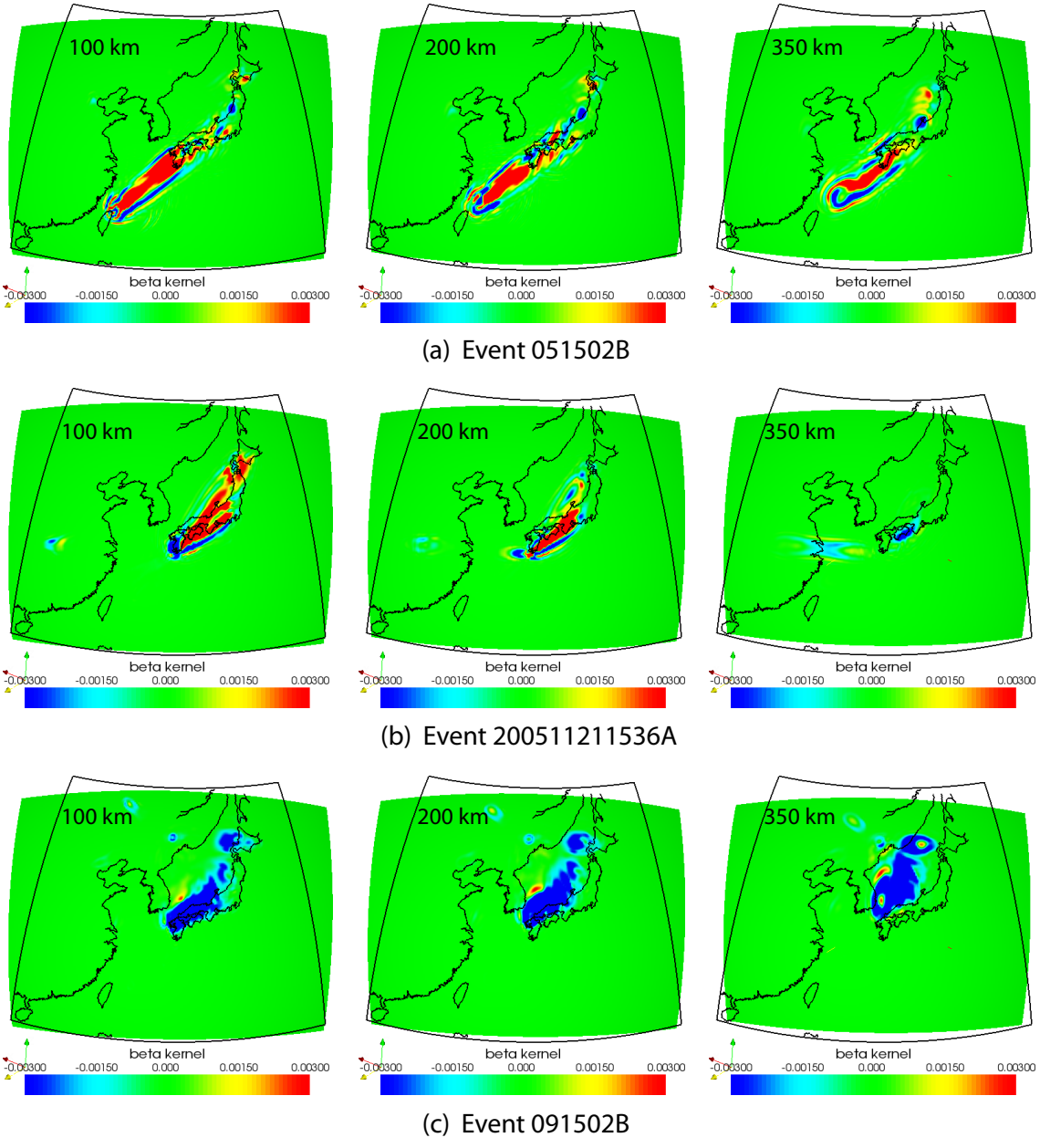

Figure 4.22: Map view of the spherical cross-sections of event kernels plotted in Paraview, for shear-wave velocity (β) at depths of 100 km, 200 km, and 350 km. The three example events are at different depths and locations (Table 4.3). (a) Event 051502B (depth = 22.4 km). (b) Event 200511211536A (depth = 155.0 km). (c) Event 091502B (depth = 589.4 km).

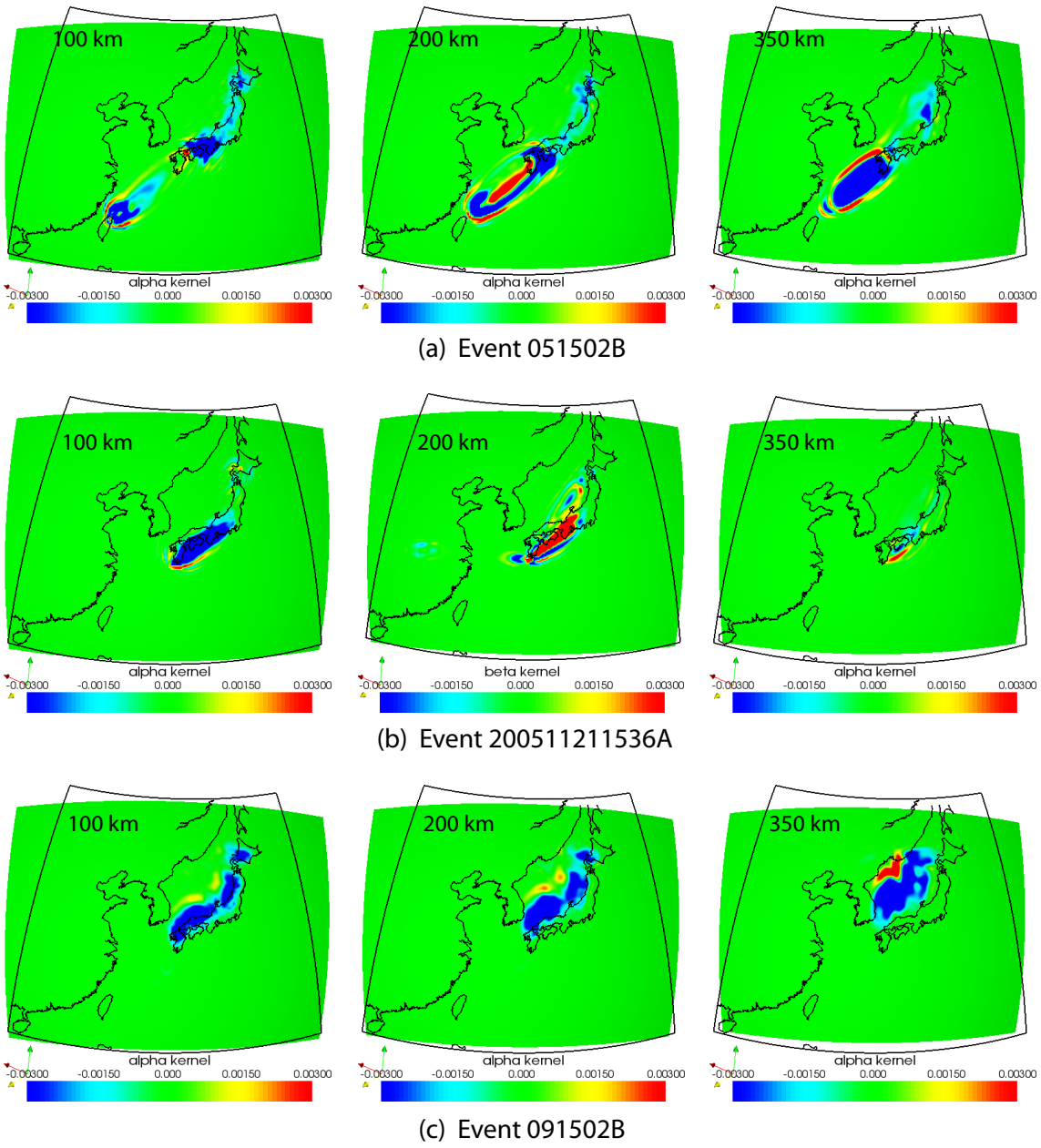

Figure 4.23: Map view of the spherical cross-sections of event kernels plotted in Paraview, for compressional-wave velocity (α) at depths of 100 km, 200 km, and 350 km. The three example events are at different depths and locations (Table 4.3). (a) Event 051502B (depth = 22.4 km). (b) Event 200511211536A (depth = 155.0 km). (c) Event 091502B (depth = 589.4 km).

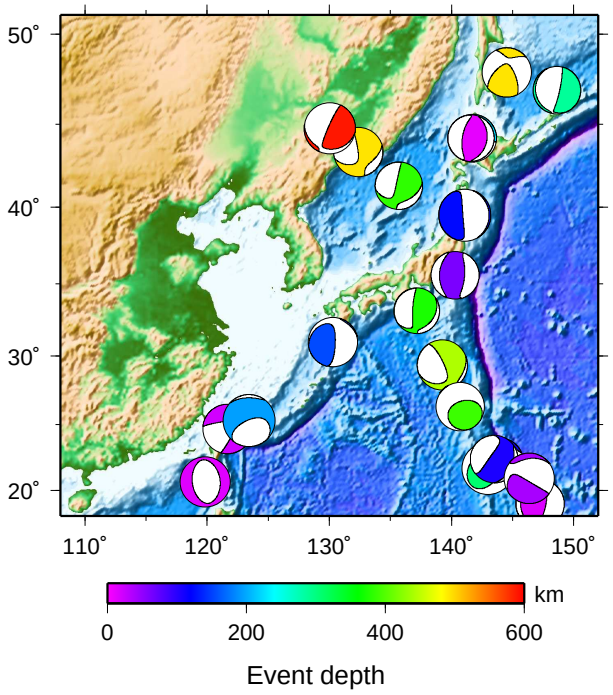

Figure 4.24: The spatial distribution of a subset of 21 events, with the source locations and focal mechanisms from the Harvard centroid-moment tensor (CMT) solutions (Table 4.3). The beach ball of each event is colored according to its depth.

the slab observed in a previous chapter (Chapter 3, *Chen et al.* [2007]). However, these small-scale features need to be further investigated by using more event kernels.

4.6 Discussion

For the adjoint tomography of the Japan subduction zone, we prepare the datasets with frequency-dependent traveltime measurements from both body waves and surface waves. Using the automated windowing code FLEXWIN, we select a subset of 206 events from the original 269 events, excluding the events with very bad data-synthetics fits. The frequency-dependent traveltime measurements are made in 44,709 windows for the period range of 24–120 s and 119,376 windows for the period range of 6–30 s. The combined adjoint sources are thus constructed based on these traveltime misfit measurements for all the receivers. Ten sample event kernels are summed up to make the preliminary misfit kernels.

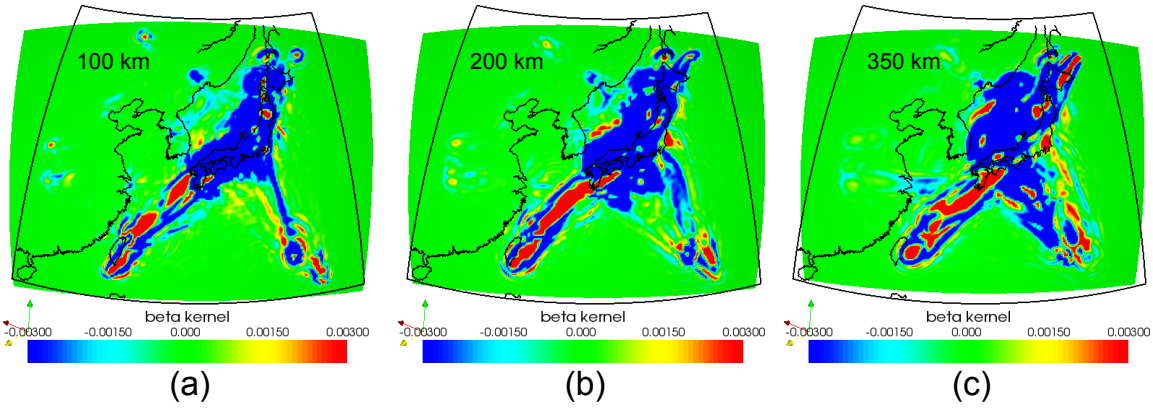

Figure 4.25: Map view of the spherical cross-sections of the misfit kernels, summation of 21 event kernels, for shear-wave velocity (β) at depths of (a) 100 km, (b) 200 km, and (c) 350 km. The spatial distribution of these 21 events are shown in Figure 4.24.

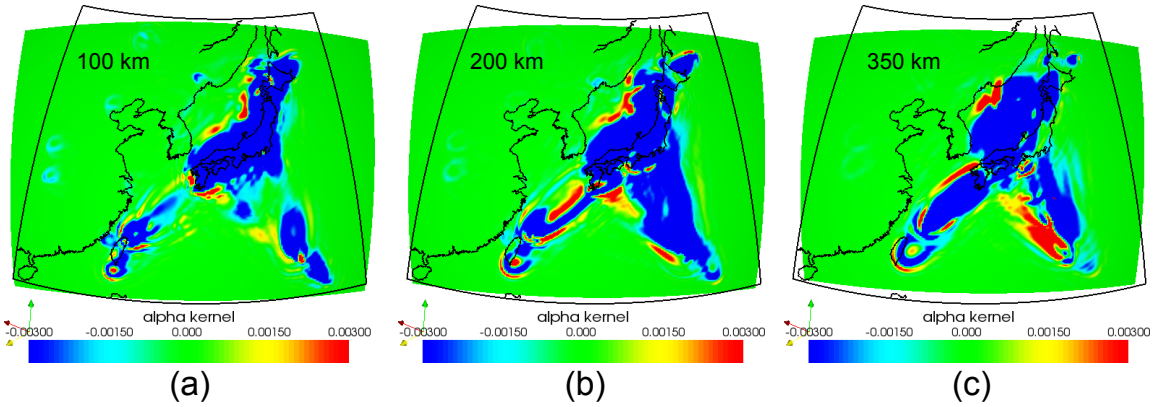

Figure 4.26: Map view of the spherical cross-sections of the misfit kernels, summation of 21 event kernels, for compressional-wave velocity (α) at depths of (a) 100 km, (b) 200 km, and (c) 350 km. The spatial distribution of these 21 events are shown in Figure 4.24.

The negative gradients for both β and α in the slab region indicate the seismic velocities of the slab need to be faster in order to minimize the data-synthetics misfit. The next step toward the adjoint tomography of the Japan subduction zone is to calculate all 206 event kernels and construct the kernels of the misfit function.

In this study, we are able to maximize the information obtained from three-component seismic records for tomographic inversion. With the kernels of the misfit function ready, we can then proceed to solve both the source and structural inversion problem using the methods discussed by *Tromp et al.* [2005] and *Tape et al.* [2007b], which have already been applied for synthetic examples. The final misfit kernel obtained from our entire dataset will be able to give us a better idea of how to refine the seismic structure in Japan subduction zone iteratively.

Appendix A

Theory of Body-Wave Anisotropy

A.1 Anisotropic Body-Wave Coefficients

Tables A.1, A.2, A.3, and A.4 tabulate the coefficients α_{nl} and β_{nl} in equations (2.30), (2.37), and (2.38) for qP, qS_1, and qS_2 waves, respectively. For brevity, let us define an auxiliary symmetric, 6×6 elastic tensor with elements C_{IJ}, $I, J = 1, \ldots, 6$, which, for

Table A.1: Coefficients α_{nl} and β_{nl} in (2.30) for B_{33}

α_{nl}	$0i$	$2i$	$4i$
0ζ	$\frac{3}{8}(\delta A + \delta C + 4\delta L + 2\delta F)$	$\frac{1}{2}(\delta C - \delta A)$	$\frac{1}{8}(\delta A + \delta C - 4\delta L - 2\delta F)$
1ζ	0	$2(2J_c - K_c)$	$-K_c$
2ζ	$\frac{1}{8}(3B_c + 2H_c + 4G_c)$	$-\frac{1}{2}B_c$	$\frac{1}{8}(B_c - 2H_c - 4G_c)$
3ζ	0	D_c	$-\frac{1}{2}D_c$
4ζ	$\frac{3}{8}E_c$	$-\frac{1}{2}E_c$	$\frac{1}{8}E_c$
β_{nl}	$0i$	$2i$	$4i$
1ζ	0	$2(2J_s - K_s)$	$-K_s$
2ζ	$-\frac{1}{8}(3B_s + 2H_s + 4G_s)$	$\frac{1}{2}B_s$	$-\frac{1}{8}(B_s - 2H_s - 4G_s)$
3ζ	0	D_s	$-\frac{1}{2}D_s$
4ζ	$-\frac{3}{8}E_s$	$\frac{1}{2}E_s$	$-\frac{1}{8}E_s$

Table A.2: Coefficients α_{nl} and β_{nl} in (2.37) for B_{11}

α_{nl}	$0i$	$2i$	$4i$
0ζ	$\frac{1}{8}(\delta A + \delta C + 4\delta L - 2\delta F)$	0	$-\frac{1}{8}(\delta A + \delta C - 4\delta L - 2\delta F)$
1ζ	0	0	K_c
2ζ	$\frac{1}{8}(B_c - 2H_c + 4G_c)$	0	$-\frac{1}{8}(B_c - 2H_c - 4G_c)$
3ζ	0	0	$\frac{1}{2}D_c$
4ζ	$\frac{1}{8}E_c$	0	$-\frac{1}{8}E_c$
β_{nl}	$0i$	$2i$	$4i$
1ζ	0	0	K_s
2ζ	$-\frac{1}{8}(B_s - 2H_s + 4G_s)$	0	$\frac{1}{8}(B_s - 2H_s - 4G_s)$
3ζ	0	0	$\frac{1}{2}D_s$
4ζ	$-\frac{1}{8}E_s$	0	$\frac{1}{8}E_s$

Table A.3: Coefficients α_{nl} and β_{nl} in (2.37) for B_{22}

α_{nl}	$0i$	$2i$	$4i$
0ζ	$\frac{1}{2}(\delta N + \delta L)$	$-\frac{1}{2}(\delta N - \delta L)$	0
1ζ	0	M_c	0
2ζ	$-\frac{1}{2}G_c$	$-\frac{1}{2}G_c$	0
3ζ	0	$-D_c$	0
4ζ	$-\frac{1}{2}E_c$	$\frac{1}{2}E_c$	0
β_{nl}	$0i$	$2i$	$4i$
1ζ	0	M_s	0
2ζ	$\frac{1}{2}G_s$	$\frac{1}{2}G_s$	0
3ζ	0	D_s	0
4ζ	$\frac{1}{2}E_s$	$-\frac{1}{2}E_c$	0

Table A.4: Coefficients α_{nl} and β_{nl} in (2.38) for B_{12}

α_{nl}	i	$3i$
0ζ	0	0
1ζ	$-(\frac{1}{2}K_s + M_s)$	$-\frac{1}{2}K_s$
2ζ	$\frac{1}{8}(B_s + 4G_s - 2H_s)$	$-\frac{1}{8}(B_s - 4G_s - 2H_s)$
3ζ	$\frac{1}{4}D_s$	$-\frac{3}{4}D_s$
4ζ	$\frac{1}{4}E_s$	$-\frac{1}{4}E_s$
β_{nl}	i	$3i$
1ζ	$\frac{1}{2}K_c + M_c$	$\frac{1}{2}K_c$
2ζ	$\frac{1}{8}(B_c + 4G_c - 2H_c)$	$-\frac{1}{8}(B_c - 4G_c - 2H_c)$
3ζ	$-\frac{1}{4}D_c$	$\frac{3}{4}D_c$
4ζ	$\frac{1}{4}E_c$	$-\frac{1}{4}E_c$

spherical problems, are related to the elements of the elastic tensor c_{ijkl} by

$$\begin{pmatrix} C_{11} & C_{12} & C_{13} & C_{14} & C_{15} & C_{16} \\ & C_{22} & C_{23} & C_{24} & C_{25} & C_{26} \\ & & C_{33} & C_{34} & C_{35} & C_{36} \\ & & & C_{44} & C_{45} & C_{46} \\ & & & & C_{55} & C_{56} \\ & & & & & C_{66} \end{pmatrix} = \begin{pmatrix} c_{\theta\theta\theta\theta} & c_{\theta\theta\phi\phi} & c_{\theta\theta rr} & c_{\theta\theta\phi r} & c_{\theta\theta\theta r} & c_{\theta\theta\theta\phi} \\ & c_{\phi\phi\phi\phi} & c_{\phi\phi rr} & c_{\phi\phi\phi r} & c_{\phi\phi\theta r} & c_{\phi\phi\theta\phi} \\ & & c_{rrrr} & c_{rr\phi r} & c_{rr\theta r} & c_{rr\theta\phi} \\ & & & c_{\phi r\phi r} & c_{\phi r\theta r} & c_{\phi r\theta\phi} \\ & & & & c_{\theta r\theta r} & c_{\theta r\theta\phi} \\ & & & & & c_{\theta\phi\theta\phi} \end{pmatrix}. \tag{A.1}$$

For Cartesian problems in which x denotes East, y North, and z up, i.e., for regional simulations, we have instead

$$\begin{pmatrix} C_{11} & C_{12} & C_{13} & C_{14} & C_{15} & C_{16} \\ & C_{22} & C_{23} & C_{24} & C_{25} & C_{26} \\ & & C_{33} & C_{34} & C_{35} & C_{36} \\ & & & C_{44} & C_{45} & C_{46} \\ & & & & C_{55} & C_{56} \\ & & & & & C_{66} \end{pmatrix} = \begin{pmatrix} c_{yyyy} & c_{yyxx} & c_{yyzz} & c_{yyxz} & -c_{yyyz} & -c_{yyyx} \\ & c_{xxxx} & c_{xxzz} & c_{xxxz} & -c_{xxyz} & -c_{xxyx} \\ & & c_{zzzz} & c_{zzxz} & -c_{zzyz} & -c_{zzyx} \\ & & & c_{xzxz} & -c_{xzyz} & -c_{xzyx} \\ & & & & c_{yzyz} & c_{yzyx} \\ & & & & & c_{yxyx} \end{pmatrix}. \tag{A.2}$$

From tables A.1, A.2, A.3, and A.4 we note that of the 21 independent elastic parameters there are five ζ-independent terms:

$$\begin{aligned} \delta A &= \tfrac{1}{8}(3C_{11} + 3C_{22} + 2C_{12} + 4C_{66}), \\ \delta C &= C_{33}, \\ \delta N &= \tfrac{1}{8}(C_{11} + C_{22} - 2C_{12} + 4C_{66}), \\ \delta L &= \tfrac{1}{2}(C_{44} + C_{55}), \\ \delta F &= \tfrac{1}{2}(C_{13} + C_{23}). \end{aligned} \tag{A.3}$$

There are six ζ-dependent terms:

$$\begin{aligned} J_c &= \tfrac{1}{8}(3C_{15} + C_{25} + 2C_{46}), \\ J_s &= \tfrac{1}{8}(C_{14} + 3C_{24} + 2C_{56}), \\ K_c &= \tfrac{1}{8}(3C_{15} + C_{25} + 2C_{46} - 4C_{35}), \\ K_s &= \tfrac{1}{8}(C_{14} + 3C_{24} + 2C_{56} - 4C_{34}), \\ M_c &= \tfrac{1}{4}(C_{15} - C_{25} + 2C_{46}), \\ M_s &= \tfrac{1}{4}(C_{14} - C_{24} - 2C_{56}). \end{aligned} \tag{A.4}$$

There are six 2ζ-dependent terms:

$$\begin{aligned} G_c &= \tfrac{1}{2}(C_{55} - C_{44}), \\ G_s &= -C_{45} \\ B_c &= \tfrac{1}{2}(C_{11} - C_{22}), \\ B_s &= -(C_{16} + C_{26}), \\ H_c &= \tfrac{1}{2}(C_{13} - C_{23}), \\ H_s &= -C_{36}. \end{aligned} \tag{A.5}$$

There are two 3ζ-dependent terms:

$$\begin{aligned} D_c &= \tfrac{1}{4}(C_{15} - C_{25} - 2C_{46}), \\ D_s &= \tfrac{1}{4}(C_{14} - C_{24} + 2C_{56}). \end{aligned} \tag{A.6}$$

And finally, there are two 4ζ-dependent terms:

$$\begin{aligned} E_c &= \tfrac{1}{8}(C_{11} + C_{22} - 2C_{12} - 4C_{66}), \\ E_s &= -\tfrac{1}{2}(C_{16} - C_{26}). \end{aligned} \tag{A.7}$$

For near-horizontally propagating body waves (radial anisotropy), i.e., when the incidence angle $i \approx 90^\circ$, the qP, qS_1, and qS_2 body-wave phase speeds are determined by (2.27) and (2.33), where

$$B_{33} = \rho^{-1}(\delta A + B_c \cos 2\zeta - B_s \sin 2\zeta + E_c \cos 4\zeta - E_s \sin 4\zeta), \tag{A.8}$$

$$B_{11} = \rho^{-1}(\delta L + G_c \cos 2\zeta - G_s \sin 2\zeta), \tag{A.9}$$

$$B_{22} = \rho^{-1}(\delta N - E_c \cos 4\zeta + E_s \sin 4\zeta), \tag{A.10}$$

$$B_{12} = \rho^{-1}(-M_c \sin \zeta - M_s \cos \zeta - D_c \sin 3\zeta + D_s \cos 3\zeta). \tag{A.11}$$

Note that the waves speeds exhibit the symmetry $\delta c/c(\pi/2, \zeta) = \delta c/c(\pi/2, \zeta + \pi)$. Finally, in a transversely isotropic Earth model $B_{12} = 0$, we see that the shear waves travel with phase speeds determined by δL and δN, and the P wave travels with a phase speed determined by δA.

For near-vertically propagating body waves (i.e., 'shear-wave splitting'), i.e., when the incidence angle $i \approx 0^\circ$ or 180°, we have

$$B_{33} = \rho^{-1}\delta C, \tag{A.12}$$

$$B_{11} = \rho^{-1}(\delta L + G_c \cos 2\zeta - G_s \sin 2\zeta), \tag{A.13}$$

$$B_{22} = \rho^{-1}(\delta L - G_c \cos 2\zeta + G_s \sin 2\zeta), \tag{A.14}$$

$$B_{12} = \rho^{-1}(G_c \sin 2\zeta + G_s \cos 2\zeta). \tag{A.15}$$

The qP, qS_1, and qS_2 body-wave phase speeds determined by (2.27) and (2.33) thus become

$$(\delta c/c)_3 = (2\rho c^2)^{-1}\delta C, \tag{A.16}$$

$$(\delta c/c)_{1,2} = (2\rho c^2)^{-1}(\delta L \pm \sqrt{G_c^2 + G_s^2}), \tag{A.17}$$

i.e., independent of the ray azimuth ζ, with a polarization angle Φ determined by (2.35):

$$\tan 2\Phi = \frac{G_s + G_c \tan 2\zeta}{G_c - G_s \tan 2\zeta}\,. \tag{A.18}$$

If we define

$$\tan 2\Phi_0 = \frac{G_s}{G_c}, \tag{A.19}$$

then we obtain the simple expression

$$\Phi = \Phi_0 + \zeta. \tag{A.20}$$

In the context of near-vertical SKS shear-wave splitting, we deduce that the split travel-time ΔT, obtained by using (A.17) in (2.41), and the polarization angle (A.20) constrain the G_c and G_s anisotropic parameters. Finally, for transversely isotropic Earth models we deduce from (A.17) that the two S waves travel with the same phase speed, i.e., there is no splitting.

Bibliography

Abers, G., Hydrated subducted crust at 100–250 km depth, *Earth and Planetary Science Letters*, *176*, 323–330, 2003.

Backus, G. E., Possible forms of seismic anisotropy of the uppermost mantle under oceans, *J. Geophys. Res.*, *70*, 3429–3439, 1965.

Bassin, C., G. Laske, and G. Masters, The current limits of resolution for surface wave tomography in North America, *EOS*, *81*, F897, 2000.

Capdeville, Y., E. Chaljub, J. P. Vilotte, and J.-P. Montagner, Coupling the spectral element method with a modal solution for elastic wave propagation in global Earth models, *Geophys. J. Int.*, *152*, 34–67, 2003.

Červený, V., Direct and inverse kinematic problems for inhomogeneous anisotropic media — Linearization approach, *Contrib. Geophys. Inst. Slov. Acad. Sci.*, *13*, 127–133, 1982.

Červený, V., *Seismic Ray Theory*, Cambridge University Press, Cambridge, UK, 2001.

Chaljub, E., Y. Capdeville, and J. P. Vilotte, Solving elastodynamics in a fluid-solid heterogeneous sphere: a parallel spectral element approximation on non-conforming grids, *J. Comput. Phys.*, *187*(2), 457–491, 2003.

Chapman, C., *Fundamentals of Seismic Wave Propagation*, Cambridge University Press, Cambridge, UK, 2004.

Chen, M., and J. Tromp, Theoretical and numerical investigations of global and regional seismic wave propagation in weakly anisotropic Earth Models, *Geophys. J. Int.*, *168*, 1130–1152, 2007.

Chen, M., J. Tromp, D. Helmberger, and H. Kanamori, Waveform modeling of the slab beneath Japan, *J. Geophys. Res.*, *112*, doi:10.1029/2006JB004394, 2007.

Cormier, V. F., Slab diffraction of S waves, *Journal of Geophysical Research—Solid Earth*, *94*, 3006–3024, 1989.

Crampin, S., A review of the effects of anisotropic layering on the propagation of seismic waves, *Geophys. J. R. Astron. Soc.*, *49*, 9–27, 1977.

Crampin, S., An introduction to wave propagation in anisotropic media, *Geophys. J. R. Astron. Soc.*, *76*, 17–28, 1984.

Dahlen, F. A., and J. Tromp, *Theoretical Global Seismology*, Princeton University Press, Princeton, NJ, 1998.

Dragert, H., K. Wang, and T. S. James, A silent slip event on the deeper Cascadia subduction interface, *Science*, *292*, 1525–1528, 2001.

Dziewonski, A. M., and D. L. Anderson, Preliminary reference Earth model, *Phys. Earth Planet. Inter.*, *25*, 297–356, 1981.

Ekström, G., J. Tromp, and W. F. Larson, Measurements and global models of surface wave propagation, *J. Geophys. Res.*, *102*, 8137–8157, 1997.

Farra, V., First-order ray tracing for qs waves in inhomogeneous weakly anisotropic media, *Geophys J. Int.*, *161*, 309–324, 2005.

Forsyth, D. W., The early structural evolution and anisotropy of the oceanic upper mantle, *Geophys. J. R. Astron. Soc.*, *43*, 103–162, 1975.

Fukao, Y., S. Hori, and M. Ukawa, A seismological constraint on the depth of basalt-eclogite transition in a subducting oceanic crust, *Nature*, *303*, 413–415, 1983.

Furumura, T., and B. L. N. Kennett, Subduction zone guided waves and heterogeneity structure of the subducted plate: Intensity anomalies in northern Japan, *J. Geophys. Res.*, *110*(B10302), doi: 10.1029/2004JB003486, 2005.

Hacker, B. R., G. Abers, and S. Peacock, Subduction factory 1. theoretical mineralogy, densities, seismic wave speeds and H2O contents, *J. Geophys. Res.*, *108*, No. B1, 2029, 2003a.

Hacker, B. R., S. M. Peacock, G. A. Abers, and S. D. Holloway, Subduction factory 2. are intermediate-depth earthquakes in subducting slabs linked to metamorphic dehydration reactions?, *J. Geophys. Res.*, *108*, No. B1, 2030, 2003b.

Hanyga, A., The kinematic inverse problem for weakly laterally inhomogeneous anisotropic media, *Tectonophysics*, *90*, 253–262, 1982.

Helmberger, D. V., and J. E. Vidale, Modeling strong motions produced by earthquakes with two-dimensional numerical codes, *Bulletin of the Seismological Society of America*, *78*, 109–121, 1988.

Hjörleifsdóttir, V., Earthquake source charaterization using 3D numerical modeling, Ph.D. thesis, California Institute of Technology, 2007.

Hori, S., Seismic wave guided by untransformed oceanic crust subducting into the mantle: The case of the Kanto district, central Japan, *Tectonophysics*, *176*, 355–376, 1990.

Igel, H., T. Nissen-Meyer, and G. Jahnke, Wave propagation in 3D spherical sections: effects of subduction zones, *Phys. Earth Planet. Inter.*, *132*, 219–234, 2002.

Jech, J., and I. Pšenčík, First-order perturbation method for anisotropic media, *Geophys J. Int.*, *99*, 369–376, 1989.

Kanamori, H., Seismological evidence for a lithospheric normal faulting—the Sanriku earthquake of 1933, *Phys. Earth. Planet. Interiors*, *4*, 289–300, 1971.

Kawakatsu, H., and S. Watada, Seismic evidence for deep-water transportation in the mantle, *Phys. Earth Planet. Inter.*, *152*, 144–162, 2005.

Kennett, B. L. N., and E. R. Engdahl, Traveltimes for global earthquake location and phase identification, *Geophys. J. Int.*, *105*, 429–465, 1991.

Kobayashi, K., M. Nakanishi, K. Tamaki, and Y. Ogawa, Outer slope faulting associated with the western Kuril and Japan trenches, *Geophysical Journal international*, *134*, 356–372, 1998.

Komatitsch, D., and J. Tromp, Introduction to the spectral-element method for 3-D seismic wave propagation, *Geophys. J. Int.*, *139*, 806–822, 1999.

Komatitsch, D., and J. Tromp, Spectral-element simulations of global seismic wave propagation—I. Validation, *Geophys. J. Int.*, *149*, 390–412, 2002a.

Komatitsch, D., and J. Tromp, Spectral-element simulations of global seismic wave propagation—II. 3-D models, oceans, rotation, and self-gravitation, *Geophys. J. Int.*, *150*, 303–318, 2002b.

Komatitsch, D., and J. P. Vilotte, The spectral-element method: an efficient tool to simulate the seismic response of 2D and 3D geological structures, *Bull. Seismol. Soc. Am.*, *88*(2), 368–392, 1998.

Komatitsch, D., C. Barnes, and J. Tromp, Simulation of anisotropic wave propagation based upon a spectral element method, *Geophysics*, *65*(4), 1251–1260, 2000.

Komatitsch, D., Q. Liu, J. Tromp, P. Süss, C. Stidham, and J. H. Shaw, Simulations of ground motion in the Los Angeles Basin based upon the spectral-element method, *Bull. Seismol. Soc. Am.*, *94*, 187–206, 2004.

Larson, E., J. Tromp, and G. Ekström, Effects of slight anisotropy on surface waves, *Geophys. J. Int.*, *132*, 654–666, 1998.

Lebedev, S., and G. Nolet, Upper mantle beneath Southeast Asia from S velocity tomography, *J. Geophys. Res.*, *108*, doi:10.1029/2000JB000073, 2003.

Love, A. E. H., *Some problems of geodynamics*, Cambridge University Press, Cambridge,UK, 1911.

Maggi, A., C. Tape, M. Chen, D. Chao, and J. Tromp, An automated time-window selection algorithm for seismic tomography, *in preparation*, 2008.

Manea, V. C., and M. Gurnis, Subduction zone evolution and low viscosity wedges and channels, *Earth Planet. Sci. Lett.*, *264*, 22–45, 2007.

Martin, S., A. Rietbrock, C. Haberland, and G. Asch, Guided waves propagating in subducted oceanic crust, *J. Geophys. Res.*, *108*(B11), 2536, doi: 10.1029/2003JB002450, 2003.

Martin, S., C. Haberland, and A. Rietbrock, Forearc decoupling of guided waves in the Chile-Peru subduction zone, *Geophys. Res. Lett.*, *32*(L23309), doi: 10.1029/2005GL024183, 2005.

Matsuzawa, T., N. Umino, A. Hasegawa, and A. Takagi, Upper mantle velocity structure estimated from PS-converted wave beneath the north-eastern Japan arc, *Geophys. J. R. Astr. Soc.*, *86*, 767–787, 1986.

Mensch, T., and P. Rasolofosaon, Elastic-wave velocities in anisotropic mediua of arbitrary symmetry—generalization of thomsen's parameters ϵ, δ and γ, *Geophys. J. Int.*, *128*, 43–64, 1997.

Montagner, J.-P., Upper mantle low anisotropy channels below the Pacific Plate, *Earth Planet. Sci. Lett.*, *202*, 263–274, 2002.

Montagner, J.-P., and D.-A. Griot-Pimmera, How to relate body wave and surface wave anisotropy?, *J. Geophys. Res.*, *105*, 19,015–19,027, 2000.

Montagner, J.-P., and H.-C. Nataf, A simple method for inverting the azimuthal anisotropy of surface waves, *J. Geophys. Res.*, *91*, 511–520, 1986.

Montagner, J.-P., and T. Tanimoto, Global anisotropy in the upper mantle inferred from the regionalization of phase velocities, *J. Geophys. Res.*, *95*, 4797–4819, 1990.

Montagner, J.-P., and T. Tanimoto, Global upper mantle tomography of seismic velocities and anisotropies, *J. Geophys. Res.*, *96*, 20,337–20,351, 1991.

Montelli, R., G. Nolet, F. Dahlen, G. Masters, E. R. Engdahl, and S.-H. Hung, Finite-frequency tomography reveals a variety of plumes in the mantle, *Science*, *303*, 338–343, 2004.

Nishimura, C. E., and D. Forsyth, The anisotropic structure of the upper mantle in the Pacific, *Geophys. J.*, *96*, 203–229, 1989.

Ozawa, S., M. Murakami, M. Kaidzu, T. Tada, T. Sagiya, Y. Hatanaka, H. Yarai, and T. Nishimura, Detection and monitoring of ongoing aseismic slip in the Tokai region, central Japan, *Science*, *298*, 1009–1012, 2002.

Peacock, S. M., Are the lower planes of double seismic zones caused by serpentine dehydration in subducting oceanic mantle?, *Geology*, *29*, 299–302, 2001.

Peacock, S. M., and K. Wang, Seismic consequences of warm versus cool subduction metamorphism: Examples from southwest and northeast Japan, *Science*, *286*, 937–939, 1999.

Ranero, C. R., and V. Sallarès, Geophysical evidence for hydration of the crust and mantle of the Nazca plate during bending at the north Chile trech, *Geology*, *32*, No. 7; 549–552, 2004.

Ranero, C. R., A. Villaseñor, J. P. Morgan, and W. Weinrebe, Relationship between bend-faulting at trenches and intermediate-depth seismicity, *Geochemistry, Geophysics and Geosystems*, *6*, Q12,002, 2005.

Rümpker, G., and P. G. Silver, Apparent shear-wave splitting parameters in the presence of vertically varying anisotropy, *Geophys J. Int.*, *135*, 790–800, 1998.

Savage, M. K., Seismic anisotropy and mantle deformation: What have we learned from shear wave splitting?, *Reviews of Geophysics*, *37*, 65–106, 1999.

Schmidt, M. W., and S. Poli, Experimentally based water budgets for dehydrating slabs and consequencies for arc magma generation, *Earth and Planetary Science Letters*, *163*, 361–379, 1998.

Smith, M. L., and F. A. Dahlen, The azimuthal dependence of Love and Rayleigh wave propagation in a slightly anisotropic medium, *J. Geophys. Res.*, *78*, 3321–3333, 1973.

Tape, C., Q. Liu, and J. Tromp, Finite-frequency tomography using adjoint methods—Methodology and examples using membrane surface waves, *Geophys. J. Int.*, *168*, 1105–1129, 2007a.

Tape, C. H., Q. Liu, and J. Tromp, Finite-frequency tomography using adjoint methods—Methodology and examples using membrane surface waves, *Geophys. J. Int.*, *168*, 1105–1129, 2007b.

Thomsen, L., Weak elastic anisotropy, *Geophysics*, *51*, 1954–1966, 1986.

Trampert, J., and H.-J. van Heijst, Global azimuthal anisotropy in the transition zone, *Science*, *296*, 1297–1299, 2002.

Trampert, J., and J. H. Woodhouse, Global anisotropic phase velocity maps for fundamental mode surface waves between 40 and 150 seconds, *Geophys. J. Int.*, *154*, 154–165, 2003.

Tromp, J., C. H. Tape, and Q. Liu, Seismic tomography, adjoint methods, time reversal, and banana-doughnut kernels, *Geophys. J. Int.*, *160*, 195–216, 2005.

Tsvankin, I., Anisotropic parameters and p-wave velocity for othorhombic media, *Geophysics*, *62*, 1292–1309, 1997.

Vidale, J. E., Waveform effects of a high-velocity, subducted slab, *Geophysical Research Letters*, *14*, 542–545, 1987.

Vidale, J. E., and D. Garcia-Gonzalez, Seismic observation of a high-velocity slab 1200–1600 km in depth, *Geophysical Research Letters*, *15*, 369–372, 1988.

Vidale, J. E., D. V. Helmberger, and R. W. Clayton, Finite-difference seismograms for sh waves, *Bulletin of the Seismological Society of America*, *75*, 1765–1782, 1985.

Wang, Z., and D. Zhao, Seismic imaging of the entire arc of Tohoku and Hokkaido in Japan using P-wave, S-wave and sP depth-phase data, *Phys. Earth Planet. Inter.*, *152*, 144–162, 2005.

Wang, Z., and D. Zhao, Vp and Vs tomography of Kyushu, Japan: New insight into arc magmatism and forearc seismotectonics, *Phys. Earth Planet. Inter.*, *157*, 269–285, 2006.

Zhao, D., Seismic structure and origin of hotspots and mantle plumes, *Earth and Planetary Science Letters*, *192*, 251–265, 2001.

Zhao, D., and A. Hasegawa, P wave tomographic imaging of the crust and upper mantle beneath the Japan islands, *Journal of Geophysical Research-Solid Earth*, *98*, 4333–4353, 1993.

Zhao, D., S. Horiuchi, and A. Hasegawa, Seismic velocity structure of the crust beneath the Japan Islands, *Tectonophysics*, *212*, 289–301, 1992.

Zhao, D., A. Hasegawa, and H. Kanamori, Deep structure of Japan subduction zone as derived from local regional, and teleseismic events, *Journal of Geophysical Research-Solid Earth*, *99*, 22,313–22,329, 1994.

Zhao, L., T. H. Jordan, K. B. Olsen, and P. Chen, Fréchet kernels for imaging regional earth structure based on three-dimensional reference models, *Geophys. J. Int.*, *95*, 2066–2080, 2005.

Zhou, H., and G. Chen, Waveform response to the morphology of 2-D subducted slabs, *Geophys. J. Int.*, *121*, 511–522, 1995.

Zhou, Y., F. A. Dahlen, G. Nolet, and G. Laske, Finite-frequency effects in global surface-wave tomography, *Geophys. J. Int.*, *163*, 1087–1111, 2005.